Ministry of Higher Education and Scientific Research
University of Babylon / College of Science
Department of Chemistry

Synthesis of carbon nanotubes for solar celles using flame fragment deposition technique

A thesis Submitted to the College of Science, University of Babylon in Partial Fulfillment of Requirement of the Degree of Doctorate of Philosophy in Chemistry Science

By

Samaa Saadi Mahmood Obead

B.Sc. Chemistry Science - University of Babylon 2012

M. Sc. Chemistry Science - University of Babylon 2015

Supervisors

Prof. Dr. Abbas Jasim Atiyah **Prof. Dr. Falah Hassan Hussein**

2022 A.D. **1444 A.H.**

وزارة التعليم العالي والبحث العلمي

جامعة بابل / كلية العلوم

قسم الكيمياء

تحضير الأنابيب النانوية الكربونية للخلايا الشمسية باستخدام تقنية ترسيب شظايا اللهب

اطروحة مقدمة إلى كلية العلوم - جامعة بابل

وهي جزء من متطلبات نيل درجة

دكتوراه فلسفة في العلوم/ الكيمياء

من قبل

سماء سعدي محمود عبيد

بكالوريوس علوم كيمياء – جامعة بابل 2012

ماجستير علوم كيمياء – جامعة بابل 2015

بإشراف

أ. د. عباس جاسم عطية

أ. د. فلاح حسن حسين

1444 هـ

2022 م

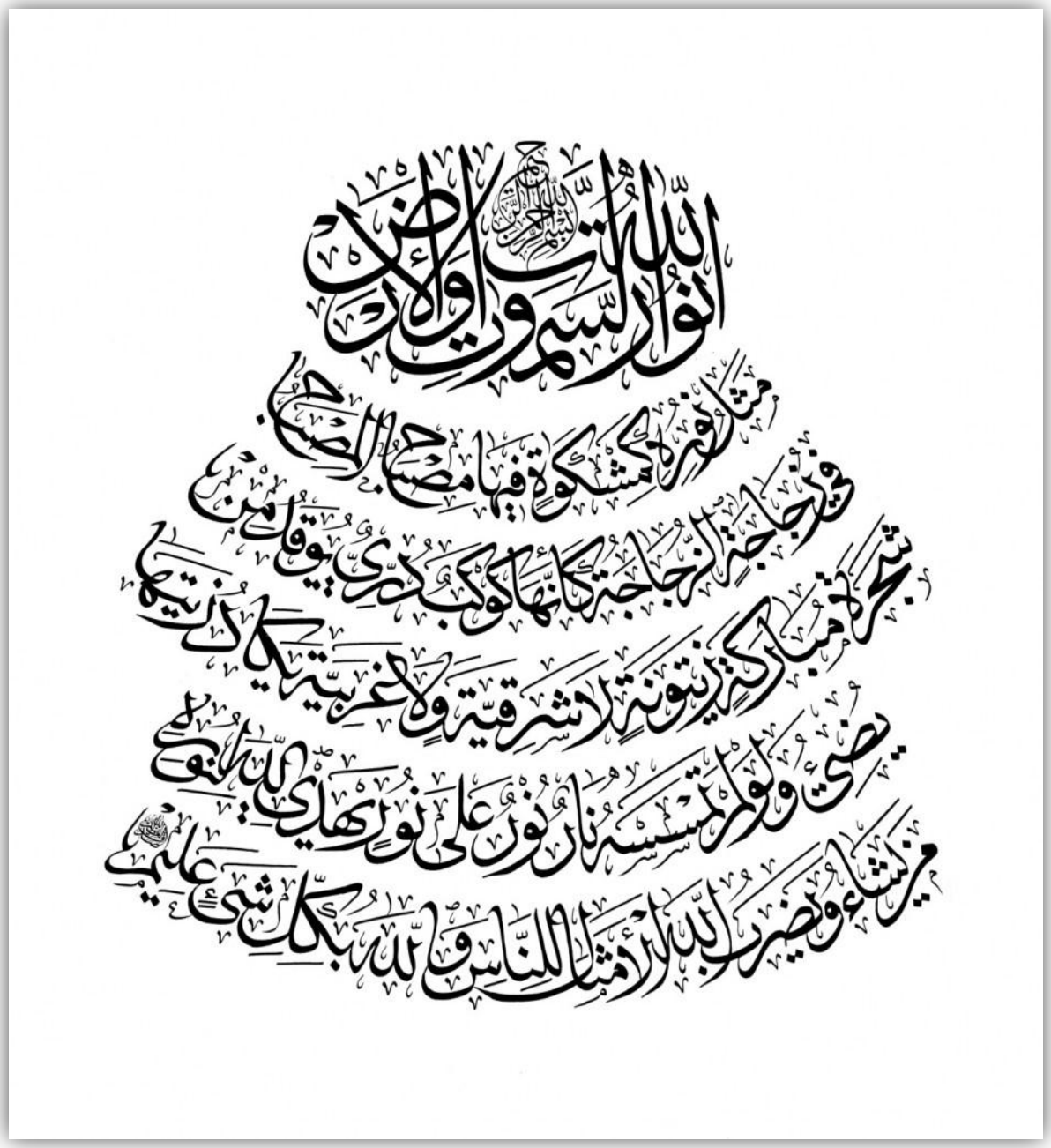

من سورة النور

الآية (٣٥)

الاهداء

الى ...

من أحمل اسمه بكل فخر... الى من أفتقده منذ الصغر ... الى من يرتعش قلبي لذكره ...

والدي (رحمه الله)

الى ...

ملاكي في الحياة ... الى من كان دعاؤها سر نجاحي وحنانها بلسم جراحي ... الى اغلى الناس ...

والدتي الحبيبة (حفظها الله)

الى ...

من تحلى بالإخاء وتميزه بالوفاء والعطاء ... الى سندي و رفيق دربي ...

نبيل (ادامه الله)

الى ...

أزهار النرجس التي تفيض حباً ونقاءاً وعطراً ... الى رياحين حياتي ...

أخواتي (أعزهن الله)

الى ...

القلوب الطاهرة الرقيقة والنفوس البريئة ... الى سندي وعضدي في الحياة ...

أخوتي (أدامهم الله)

أهديكم ثمرة جهدي معطرة بوافر حبي ...

سماح

Acknowledgements

Praise and thanks to God Who blessed me in completing this work.

Firstly, I would like to express my special appreciation and thanks to my thesis advisors **Emeritus. Prof. Falah Hassan Hussein** and. **Prof. Abbas Jasim Atiyah** for their continuous support throughout my PhD study and related researches, as they were always ready to help whenever I ran into a troubled spot or had a question about my research or its writing. Their support, motivation and guidance during the research and writing phases have been of great benefit to me.

I am grateful to the head of the chemistry department, Dr. Saadon Abdulla , and to all the members of the teaching staff in the chemistry department. Heartfelt thanks go to Dr. Firas Habeeb Abdul Razzaq (Diyala University), Dr. Abdul Kareem Al Sammeraie (University of Baghdad), Dr. Adel Alkhayatt and Dr. Adnan Ahmed (Physics Department, Science of College ,University of Kufa).

Finally, I wish to express my deepest gratitude to my family for providing me with unfailing support and continuous encouragement throughout my years of study and through the process of researching and writing this thesis. This accomplishment would not have been possible without them. Thank you.

Samaa

Summary

In this work, carbon nanotubes (CNTs) were prepared using the flame fragment deposition (FFD) method by using a homemade manufactured reactor with the use of liquefied petroleum gas (LPG) as a carbon source. The nanocomposites TiO_2/CNTs were prepared from two types of TiO_2, namely, anatase and P25 Degussa, in different proportions of both types. These were 1:0.010, 1:0.025, and 1:0.050, and these were prepared using a simple evaporation and drying process.

All the prepared nanomaterials were investigated using different techniques such as X-rays diffraction (XRD), Fourier transform infrared (FTIR) spectrometer, thermo gravimetric analysis (TGA), scanning electron microscopy (SEM), energy-dispersive X-ray spectroscopy (EDX), transmission electron microscopy (TEM), and Raman spectroscopy. The diameter of the synthesized CNTs was in the range of 29-50 nm.

The optical properties of the prepared nanocomposites TiO_2/CNTs were investigated using UV-Vis. Spectroscopy that revealed that the energy band gaps were equal to (3.13, 3.1, 3, 2.9 eV) for TiO_2 anatase and its composites (TiO_2/0.01CNTs, TiO_2/0.025CNTs, TiO_2/0.05CNTs) respectively. For TiO_2 Degussa and its composites (TiO_2/0.01CNTs,TiO_2/0.025CNTs, TiO_2/0.05CNTs) were equal to (3.22, 3.1, 3, 2.95 eV) respectively. The activity of these materials was investigated by probing their activity as active electrodes in fabricated dye synthesized solar cells (DSSCs).

These DSSCs were designed using TiO_2 of both types (anatase and Degussa) and their composites with synthesized CNTs as the anode (front

electrode) and (Pt, graphite, CNTs) as the cathode (back electrode) deposited on the surface of fluorinated tin oxide glass (FTO) in the presence of natural pomegranate dye and iodine electrolyte solution. The photovoltaic cells prepared with TiO_2(Degussa)/CNTs as the anode electrode performed better than the others, especially when used with platinum as the cathode electrode, where their efficiency reached 3.679% at the TiO_2(Degussa), 0.025 CNTs/Pt ratio.

الخلاصة :

في هذا العمل ، تم تحضير الأنابيب النانوية الكربونية (CNTs) باستخدام طريقة ترسيب شظايا اللهب (FFD) باستخدام جهاز محلي الصنع مع استخدام غاز البترول المسال (LPG) كمصدر كربوني. تم تحضير المركب النانوي TiO_2/CNT من نوعين منTiO_2 ، وهما anatase و Degussa P25 ، بنسب مختلفة من كلا النوعين ، وهي 1:0.050 ,1:0.025 ,1:0.010 وتم تحضيره باستخدام طريقة التبخير والتجفيف.

تم تشخيص جميع المواد النانوية المحضرة باستخدام تقنيات مختلفة ، مثل حيود الأشعة السينية (XRD) ،مطياف الأشعة تحت الحمراء (FTIR) ،التحليل الكمي الحراري (TGA)، المجهر الماسح الإلكتروني (SEM) ، طيف الأشعة السينية المشتتة للطاقة (EDX)، المجهر الالكتروني النافذ (TEM) وطيف رامان. كان قطر الأنابيب النانوية الكربونية المحضرة في حدود (29-50) نانومتر.

تمت دراسة الخصائص البصرية للمركبات النانوية المحضرةTiO_2/CNTs باستخدام التحليل الطيفي للأشعة فوق البنفسجية من خلال تقدير فجوة حزمة الطاقة لتكون تساوي (3.13، 3.3، 2.9) لـ TiO_2 anatase ومركباته (TiO_2/0.01CNTs, TiO_2/0.025CNTs, TiO_2/0.05CNTs) على التوالي ، و تساوي (3.22 ، 3.1 ، 3 ، 2.9) لـ TiO_2 degusa ومركباته (TiO_2/0.01CNTs, TiO_2/0.025CNTs, TiO_2/0.05CNTs) ، على التوالي. تم التحقيق في نشاط هذه المواد من خلال التحقق من نشاطها كأقطاب كهربائية نشطة في الخلايا الشمسية الاصطناعية الصبغية (DSSCs).

صُممت الخلايا الشمسية الصبغية (DSSCs) باستخدام TiO_2 من كلا النوعين (anatase & degusa) ومركباتها مع الأنابيب النانوية الكربونية المحضرة كقطب موجب (القطب الأمامي) و (البلاتين ، الجرافيت ، الانابيب النانوية المحضرة)ككاثود

(القطب الخلفي) ترسب على سطح زجاجFTO بوجود صبغة الرمان الطبيعية والمحلول الالكتروليتي هو اليودات .

أظهرت الخلايا الكهروضوئية المحضرة باستخدام TiO_2 (degusa) / CNTs كقطب أنود أنها أكثر كفاءة من الباقي ، خاصة عند استخدامها مع البلاتين كقطب كاثود ، حيث تصل كفاءتها إلى 3.679% عند النسبة TiO_2 (degusa),0.025CNT/Pt.

Certification

We certify that this thesis was prepared by **Samaa Saadi Mahmood Obead** under supervision in the Department of Chemistry, the College of Science , University of Babylon as a partial requirement for the degree of Doctor of Philosophy in Science of Chemistry.

Signature:

Name: **Dr.Abbas Jasim Atiyah**

Title: Professor

Address: College of Science ,

University of Babylon

Date: / / 2022

(Supervisor)

Signature:

Name: **Dr. Falah Hassan Hussein**

Title: Professor

Address: College of Pharmacy,

University of Babylon

Date: / / 2022

(Supervisor)

In the view of the available recommendation, I forward this thesis for debate by the examining committee.

Signature:

Name: **Dr. Saadon Abdulla Aowda**

Title: Professor

Address: Head of the Chemistry Department,

College of Science, University of Babylon.

Date: / / 2022

Table of contents

List of Tables

List of Figures

	TiO_2(anatase)/graphite , (B) TiO_2(anatase), 0.01CNTs/graphite, (C) TiO_2(anatase), 0.025CNTs /graphit (D) TiO_2(anatase), 0.05CNTs /graphite	
3.66	P-V characteristics of the fabricated DSSCs, (A) TiO_2(anatase) /graphite , (B) TiO_2(anatase), 0.01CNTs/graphite, (C) TiO_2(anatase), 0.025CNTs/graphite, (D) TiO_2(anatase), 0.05CNTs /graphite	**127**

Directory of Abbreviations

Symbol	Description
˚C	Centigrade
CB	Conduction band
CE	Conversion efficiency
CNFs	Carbon nanofibers
CNPs	Carbon nanoparticles
CNTs	Carbon nanotubes
CVD	chemical vapour deposition
DSSC	Dye sensitized solar cell
DWCNTs	Double-walled carbon nanotubes
Eg	Energy Gap
ESR	electron spin resonance
eV	Electron volt
FF	Fill factor
FFD	Flame Fragmentations Deposition
FTIR	Fourier Transform Infra-Red
FTO	fluorinated tin oxide
FWCNTs	Few-walled carbon nanotubes
g	Gram
Isc	short circuit current
ITO	indium tin oxide
LPG	liquefied petroleum gas
MWCNTs	Multi-walled carbon nanotubes

nm	**Nanometer**
O-CNTs	**Oxidized Carbon Nanotubes**
Pmax	**Maximum power**
SEM	**Scanning Electron Microscopy**
SWCNTs	**Single walled carbon nanotubes**
TCO	**transparent conductive oxide**
TEM	**Transmission Electron Microscopy**
TGA	**Thermo gravimetric analysis**
UV	**Ultraviolet**
VB	**Valance Band**
Voc	**open circuit voltage**
W	**Watt**
XRD	**X-rays diffraction**
λ	**Wavelength**

Chapter One

Introduction

Chapter two

Experimental Part

Chapter three

Results and Discussion

References

1.1. General Introduction

Nanoscience is the study of phenomena and manipulation of materials at the atomic, molecular, and macromolecular scales in order to understand and exploit properties that differ from those at larger scales. The science of nanotechnology is concerned with the design, synthesis, and application of materials and devices whose size and shape have been engineered at the nanoscale (usually cited 1-100 nanometers) [1, 2]. Nano is derived from the Greek word "nanos," which means "dwarf" [3]. Because of their size and structure, nanomaterials have different physical and chemical properties than bulk materials of the same composition [4]. Nanomaterials are materials in nanostructures and must have at least one dimension on the nanoscale . Clusters, quantum dots, nanoparticles, nanowires, and nanotubes are examples of nanostructures [5]. Nanomaterials can be both natural and synthetic (engineered nanomaterials). Natural nanomaterials are found in nature, such as volcanic ash and soot from forest fires. While carbon nanotubes (CNTs), carbon nanofibers (CNFs), graphene, fullerenes, silica, clay, metal, and metal oxide nanomaterials are examples of engineered nanomaterials that can be produced with specific shape, size, and surface properties, nanomaterials are classified into 0-D (quantam dots, nanoparticles), 1-D (carbon nanotubes, nanorods, and nanowires), 2-D (nanofilms, Nanosheets, Nanodisks, Nanoprisms, Nanoplates), and 3-D nanomaterials based on their size and shape, with 0-D, 1-D, and 2-D nanomaterials forming interfaces (powders, fibrous, multilayer, and polycrystalline materials). Typically, the performance of nanomaterials is determined more by surface area than by material composition . Nanomaterials are distinguished by their optical, magnetic, electrical, chemical, and other properties. These properties have a large impact on

electronics, sensors, energy devices, medicine, cosmetics, catalysis, and many other fields. High performance portable batteries, fuel cells, and solar cells are examples of the effects of nanomaterials on energy [6-8].

1.2. Types of Nanomaterials

Classification based on Chemical Composition.

1.2.1.Carbon-Based Nanomaterials

Fullerenes, carbon nanotubes, graphene and its derivatives, graphene oxide, nano diamonds, and carbon quantum dots are all carbon-based nanomaterials can be explain in Figure (1.1). Carbon nanoparticles have piqued attention in a variety of sectors, including biomedical uses, outstanding mechanical, optical, and chemical capabilities, and extraordinary structural dimensions [9]. Because a single carbon atom may form several valence bonds, each with its own orbital hybridization, carbon has a variety of structural forms. Carbon nanomaterial is one of the materials that has been investigated the most [10]. Carbon nanoparticles (CNPs) have shown great promise in a wide range of electrochemical applications, from energy storage and conversion (fuel cells, batteries, and super capacitors) to electrochemical sensing, due to their inherent electrochemical properties, large specific surface area, electro catalytic properties, supported electron transfer, and excellent electrical conduciveness [11].

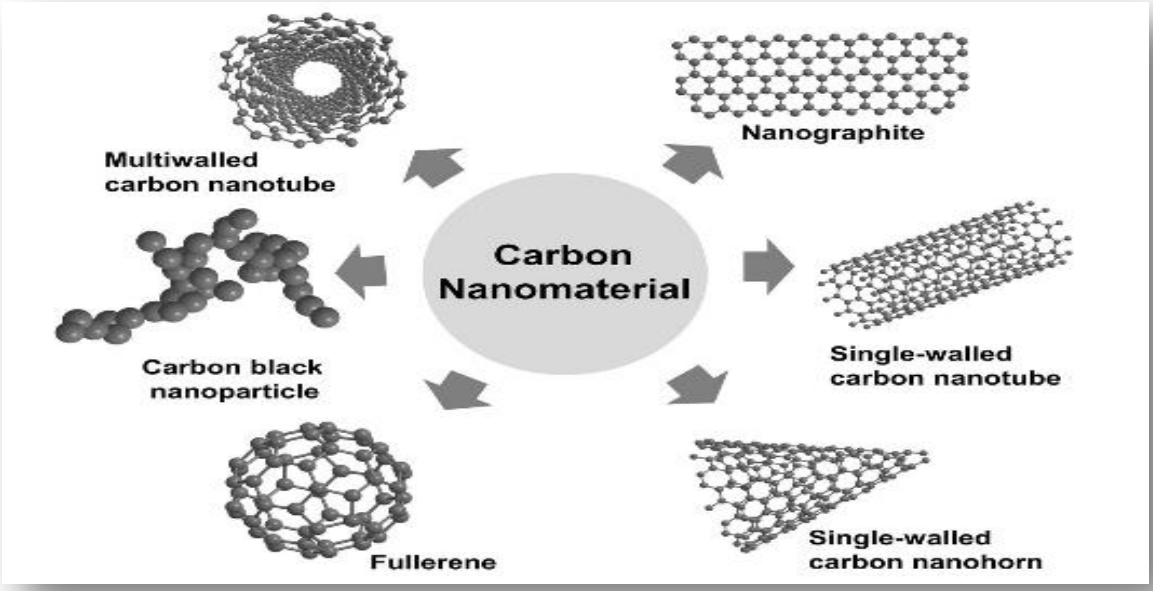

Figure (1.1): Various types of carbon-based nanomaterials [12].

1.2.2. Inorganic-Based Nanomaterials

Inorganic nanomaterials (e.g., non-metals, metal, metal oxide, and ceramic-based NMs), such as gold nanoparticles, mesoporous silica nanoparticles, graphene, magnetic nanoparticles, quantum dots, and coated double hydroxides, have been one of the most active research areas in biochemistry, biotechnology, and biomedicine can be explained in Figure (1.2) .Because of their ease of synthesis/alteration, inherent physicochemical properties, and high biocompatibility, inorganic nanomaterials have shown enormous potential in bio imaging, selective drug administration, and cancer therapy [13]. Inorganic materials with several dimensions on a nanoscale have characteristics that differ from their bulk counterparts [14]. Inorganic nanomaterials are a large class of nanomaterials that includes a wide range of elementary chemicals and compounds with a wide range of properties in optics, electronics, magnetics, and catalysis [15].

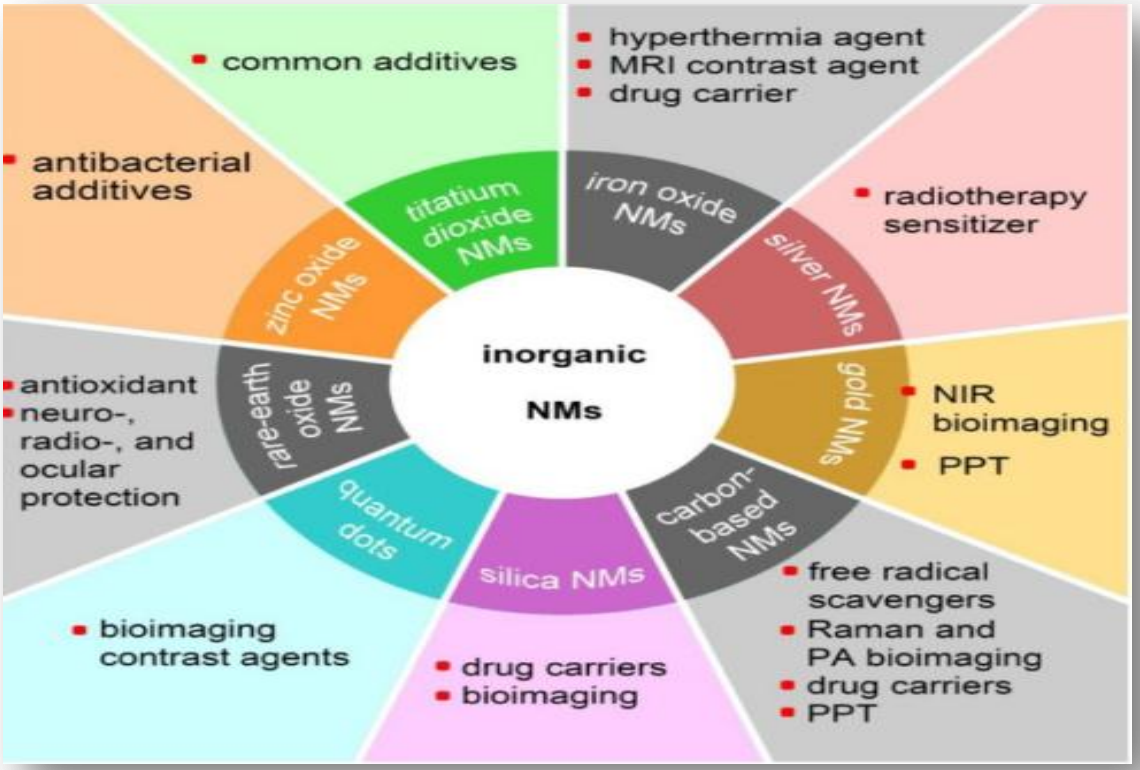

Figure (1.2): Various types Inorganic nanomaterials [16].

1.2.3. Organic-Based Nanomaterials

Organic nanoparticles are stable particles made up of organic substances (often lipids or polymers) with diameters ranging from 1nm to 10 nm. This sort of nanoparticle has seen a lot of growth and active research due to its excellent ability in a wide range of industrial domains spanning from electrical to photonic, conductive materials to sensors, medicine to biotechnology [17]. This type can be explained in Figure (1.3) [18].

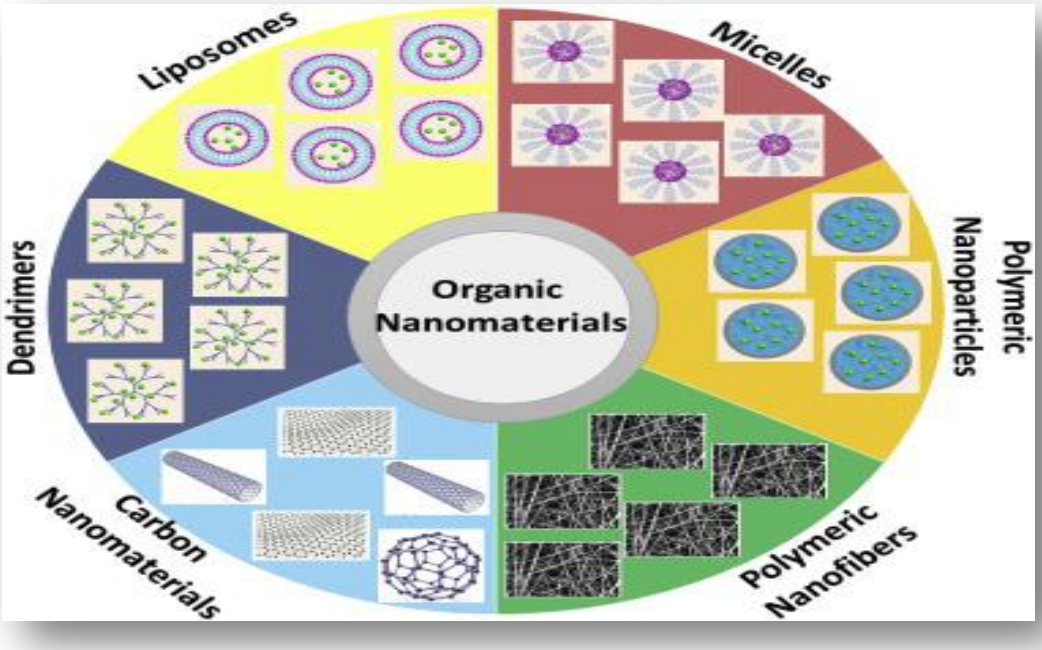

Figure (1.3) : Various types organic nanomaterials.

1.2.4. Composite-Based Nanomaterials

A composite material is created by combining two or more materials, often with very different properties, and these materials work together to give the composite its unique properties. However, because the different materials do not dissolve or blend into each other, it may be possible to tell them apart inside the composite [19]. Chemical inertness (non-reactivity) is one of the requirements for the selection and fabrication of composite materials [20]. Nanocomposites are composites in which at least one of the phases has dimensions in the nanometre range (1-100nm) [21]. Nanocomposites have unique properties that go beyond their small size, large surface area, and phase relationships at their interfaces. It is ready to improve the performance of drugs, catalysts, biomaterials, and other high-value materials [22] as shown in Figure (1.4). Ion poisoning, electrical composition, physical mixing, film casting, dipping coating, layer-by-layer aggregation, on-site preparation, coprecipitation, colloidal

aggregation, or covalent coupling are some of the ways used to make such nanocomposites [23].

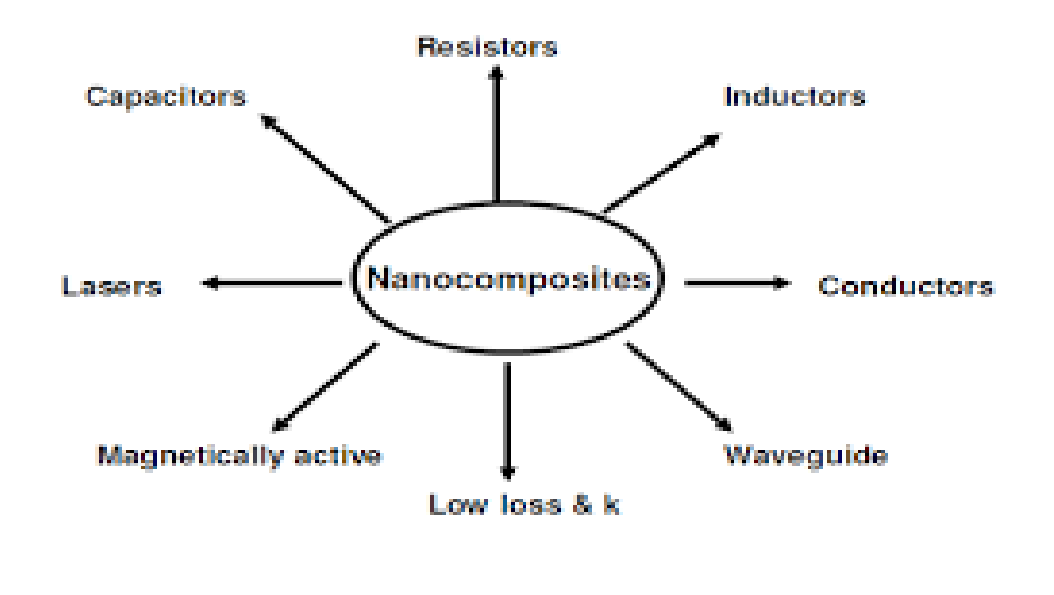

Figure (1.4): Overview of some of the potential applications of nanocomposites in microelectronics [24].

1.3. Carbon Nanotubes (CNTs)

The carbon atom is the most important chemical element found on Earth, with atomic number 6, and the 6 electrons will occupy the atomic orbitals $1s^2$, $2s^2$, and $2p^2$, which can be hybridized into three forms: sp, sp^2, and sp^3. There are many different images for carbon atoms, such as amorphous carbon, graphite, graphine, diamond, activated carbon, fullerene, and carbon nanotube [25]. Carbon nanotubes, also known as buckytubes, are cylindrical carbon molecules with unique properties that make them useful in a variety of applications, including nano-electronics, optics, large amounts of pure materials, and materials applications [26]. CNTs, also known as tubular fullerenes, are made up of cylindrical graphene sheets with sp^2 bonded carbon atoms that, when rolled upon

themselves, yield different allotropes of carbon, such as graphite, fullerenes, and CNTs [27]. CNTs have been discovered in single-walled carbon nanotubes (SWNTs) and multi-walled carbon nanotubes (MWNTs) structures [28]. Graphene is wrapped in a way that can be represented by a pair of indices (n,m) known as the chiral vector, which is dependent on indices (n,m) CNTs are classified as armchair (n=m), zigzag (m=0), or chiral (all others) as shown in Figure (1.5). Single-walled CNTs have all of these structures (armchair, zigzag or chiral), but multi-walled CNTs have only two structures (armchair or zigzag) [29]. The armchair structure is always metallic, but the other structures may make the nanotube a semiconductor [30].

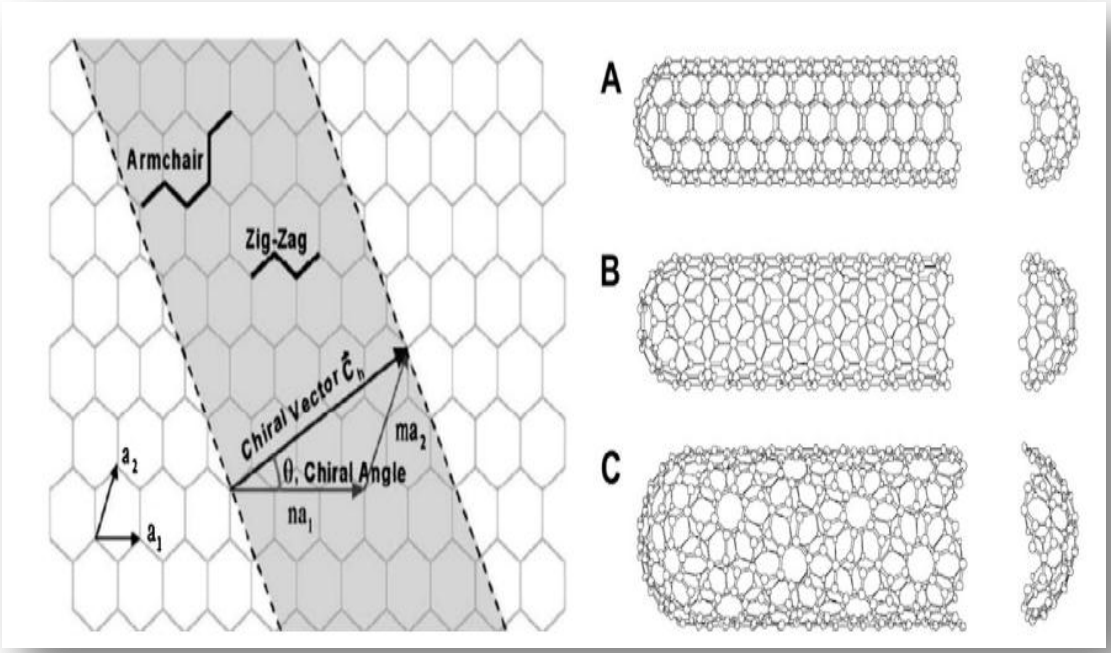

Figure (1.5): Schematic diagram showing how a hexagonal sheet of graphene is rolled to form a CNT with different chiralities (A: armchair; B: zigzag; C: chiral)[31].

1.4. Types of CNTs

CNTs are classified into four major groups according to the number of graphene layers, such as single walled carbon nanotubes (SWCNTs), double-walled carbon nanotubes (DWCNTs), few-walled carbon nanotubes (FWCNTs) and multi-walled carbon nanotubes (MWCNTs). These types are shown in Figure (1.6).

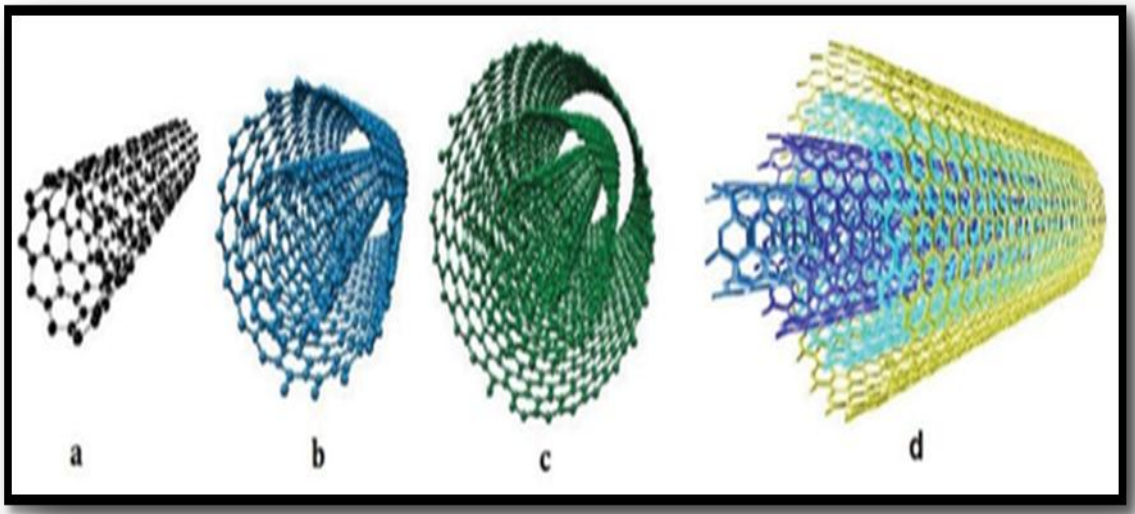

Figure (1.6): Types of carbon nanotubes (a) SWNT, (b) DWNT, (c) FWNT, (d) MWNT [32] .

1.4.1. Single-wall carbon nanotubes (SWCNTs)

Iijima [33] published the first report on single-walled carbon nanotubes (SWCNTs) in 1993. which is made up of a single cylindrical carbon layer with a diameter of 0.4-2 nm [34], and a length of 20-1000 nm [35] SWCNTs have three different structures: armchair, zigzag, and chiral, which are determined by how the cylinder is wrapped, resulting in a mixture of metallic and semiconducting materials [36,37]. SWCNTs have good electrical properties, thermal conductivity, and a surface area as large as 1300 m^2/g, but they are less pure than MWCNTs [35,38].

1.4.2. Double-walled carbon nanotubes (DWCNTs)

Two layers of graphene are used to create these nanotubes [39]. Depending on the electronic properties of the inner and outer tubes, DWCNTs show promise as nanoscale devices such as molecular cables and capacitors. However, such research is hampered by the difficulties of synthesizing significant numbers of DWCNTs in a controlled manner [40,41].

1.4.3. Few-walled carbon nanotubes (FWCNTs)

It is a subset of MWCNTs with structures similar to SWCNTs, consisting of 2-6 layers of graphene sheets [42]. Unique small diameter MWNTs with near flawless graphitization structure with diameters ranging from 3 to 8 nm and lengths in the tens of micrometers [43].

1.4.4. Multi-walled carbon nanotubes (MWCNTs)

Iijima discovered MWCNTs for the first time in 1991 [44]. This type of CNT is made up of multiple layers of graphene that have been rolled upon themselves, with a diameter ranging from 2 to 50 nm depending on the number of graphene sheets [45]. The MWCNTs may be formed in two structural models based on their arrangements of graphite layers. When the CNTs contain inside it other CNTs but the outer nanotube has a diameter that is greater than the inner nanotube, that is known as the Russian Doll model, whereas the second model is the Parchment model, which is formed when a single sheet of graphene is wrapped around itself many times, making it the same as a rolled up scroll of paper [46]. MWCNTs can be formed without using catalyst particles between two

graphite electrodes, while SWCNTs require the catalyst during preparation [47].

1.5. Synthesis of Carbon Nanotubes

Carbon nanotubes can be synthesized from a variety of carbon sources such as methane, ethylene, acetylene, natural gas, and others. These sources can produce carbon nanotubes of varying morphology, size, and purity [48]. Using pure carbon sources is very expensive and has a limited supply when compared to cheaper fuels such as natural gas, LPG and water gas [49]. The most prominent alternative carbon source is liquefied petroleum gas. It is composed of a light hydrocarbon mixture, primarily propane and butane, with a trace of sulfur. One of the advantages of this gas is that it is used as a carbon source, so it is readily available on the market and has a much lower price than other pure carbon sources [48]. There are several methods that have been developed and used for the synthesis of CNTs, most of which involve a gas phase process. The first techniques that were used to produce CNTs at high temperatures were arc discharge and laser ablation methods, but these methods have since been replaced by low temperature techniques called chemical vapour deposition (CVD) techniques [50], and This method has also been replaced here by a simpler, less expensive and more efficient method of production, which is the Flame Fragment Deposition Methods (FFD).

1.5.1. Arc-discharge method

This method uses a high temperature above 1700 ˚C to synthesize CNTs, When compared to other methods. This process typically results in the growth of CNTs with fewer structural defects. The arc-discharge method was originally used to produce C_{60} fullerenes. This process takes

place in a vacuum of gas and passes through an inert gas such as (Ar, He). In this method, graphite is used as a cathode and anode, and the chamber will also contain metal catalyst particles (such as cobalt, nickel, and/or iron), which will evaporate the anode and then condense on the surface of the cathode as carbon nanotubes when direct current is passed through the chamber as shown in Figure (1.7) [51,52].The main advantage of this method is that it produces a large number of nanotubes with high purity, while the disadvantages include being expensive, requiring a large amount of energy, and having less control over the alignment of the created nanotubes, which is critical for use and characterization [53,54].

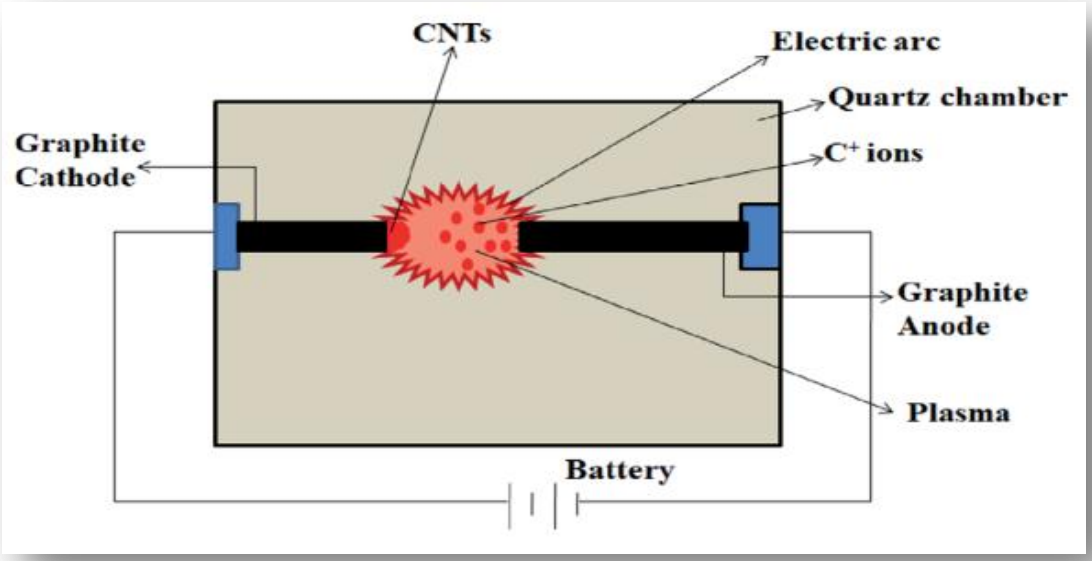

Figure (1.7): The arc discharge system for CNTs synthesis [55].

1.5.2. Laser ablation method

This method involves using a pulsed and continuous laser (YAG type) to vaporize a graphite target inside an oven filled with helium or argon gas to maintain pressure as shown in Figure (1.8). The principles and mechanisms for these methods and the arc-discharge method are similar,

but in these methods, a laser is used to provide the required energy, which is then directed at the pure graphite pellet containing catalyst materials (iron, cobalt, or nickel) [56,57]. The main advantages of this method are high yield and low metallic impurities, while the disadvantages include expensive equipment and the production of CNTs that are not always straight but contain some branching.

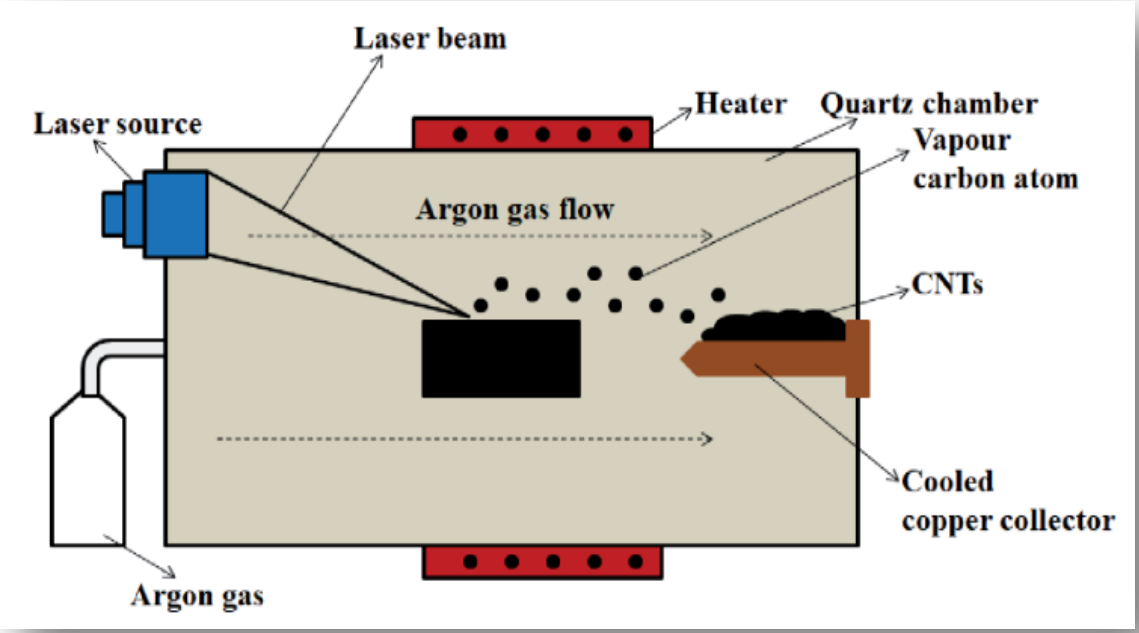

Figure (1.8): Laser ablation method for CNTs synthesis [55].

1.5.3. Chemical vapor deposition (CVD) method

In 1996, this method was used for the production and synthesis of carbon nanotubes [58]. There are many different types of these methods, such as catalytic chemical vapor deposition (CCVD), thermal or plasma enhanced (PE) oxygen assisted CVD, microwave plasma (MPECVD), radio frequency CVD (RF-CVD), or hot filament CVD (HFCVD), but the (CCVD) method is considered the standard method for CNT synthesis [59-61]. In this method, a mixture of hydrocarbon gases such as acetylene, methane, or ethylene, and nitrogen is introduced into the

reaction chamber as shown in Figure (1.9) , and the formation of nanotubes on the substrate occurs as a result of the hydrocarbon decomposition at 700-900 ˚C and atmospheric pressure [62,63]. The main advantages of these methods are that they are simple, inexpensive, require low temperatures, and are easy to control [64].

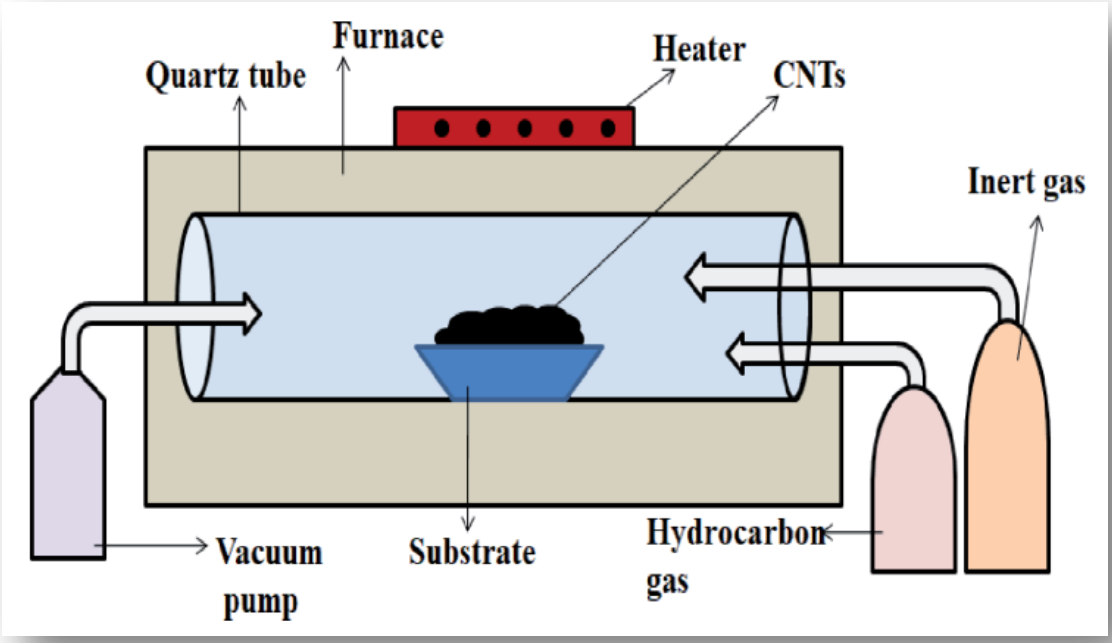

Figure (1.9): Chemical vapor deposition method for CNTs synthesis [55].

1.5.4. Flame fragment deposition methods (FFD)

Carbon nanotubes (CNTs) were synthesized using flame fragments deposition (FFD) from liquefied petroleum gas (LPG) as the carbon source, in a homemade chamber. This homemade consists of an internal burner that burns LPG in the presence of oxygen gas, the advantage of using oxygen gas is that it maintains the continuity of the burner's flame and cools the synthesized sample, whereas nitrogen gas is used to keep the flame at a suitable form. Specific gauges can be used to control the flow rates of these gases. The synthesis was carried out without the use

of any catalysts, which are known to increase the impurities of synthesized CNTs, and without the use of sophisticated tools, as is common in the classical (CVD) technique. and occurred at a lower temperature than that used in CVD technique [65,66]. Figure (1.10): depicts the schematic diagram of the homemade flame fragments deposition instrument .

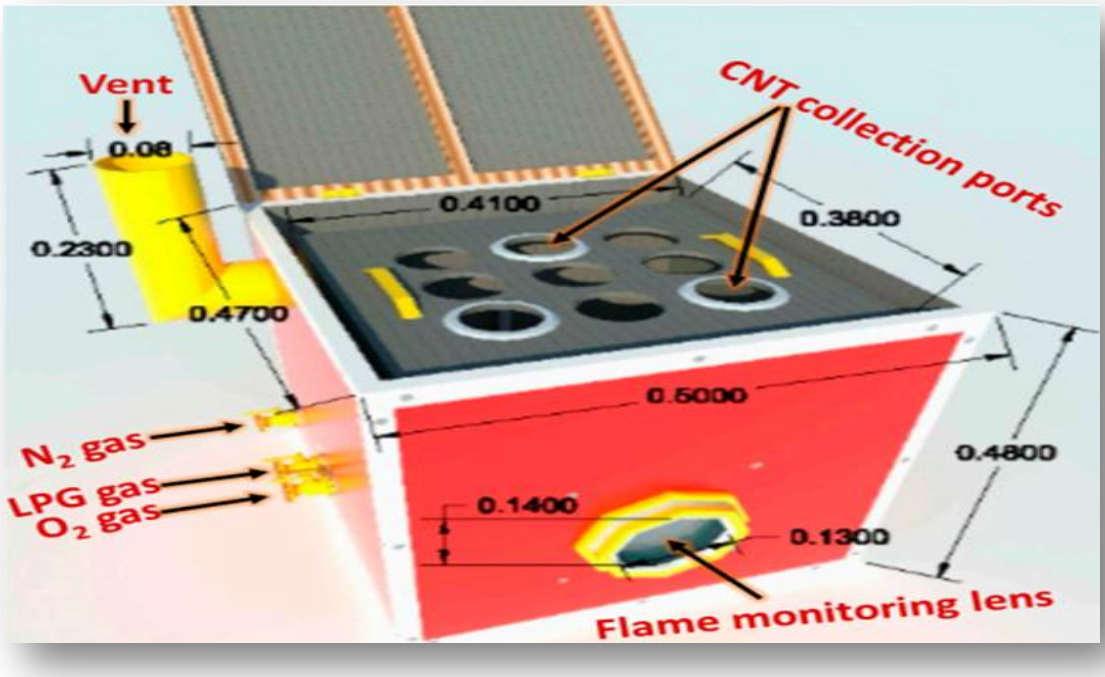

Figure (1-10): Home-made flame fragments deposition (FFD) instrument [65].

1.6. Properties of Carbon Nanotubes CNTs

CNTs have extremely large surface areas and a remarkable mechanical strength. CNTs have tensile strength 100 times that of steel, as well as electrical and thermal conductivities comparable to copper [67,68]. Because of these distinct properties, carbon nanotubes (CNTs) are promising candidates for use in a variety of applications, including solar cells [69,70]. However, in order to use carbon nanotubes in solar cells,

their mechanical, electrical, and thermal properties must be determined .

1.6.1. Mechanical properties

The mechanical properties may be understood by the nature of the bonds that form these materials , when the σ -bond is a strong chemical bond and plays an important role in the impressive mechanical properties of CNTs, the out-of-plane bond can be represented by a relatively weak π-bond that enhances the interaction between the layers in MWNTs, and between SWNTs in SWNT bundles. The bonding in nanotubes is not purely sp^2 , as bending the graphene sheet inside the tube leads to re-hybridizes the σ and π orbitals and yielding a mixture of hybridization [71]. Because CNTs have a high Young's modulus within a range of 1000-5000 GPa, they are highly resistant to physical forces. Nanotubes are also very flexible due to their length. As a result, it is well suited for applications in composite materials that require anisotropic properties [72,73].

1.6.2. Electrical properties

CNTs' electrical properties are visible in chiral forms, and the researchers have demonstrated that CNTs have distinct conductive properties. These findings suggest that geometric differences such as defects, chirality, different diameters, and the degree of crystallinity of the tubular structure have a significant impact on the electronic properties of CNTs [74,75]. The electrical properties of carbon nanotubes can be easily understood using the band structure of graphene [76]. When the carbon atoms in CNTs are arranged in a hexagonal lattice, each carbon atom is covalently bonded to three neighbor carbons via sp^2 molecular orbitals. As a result, the fourth valence electron in each unit remains free, and these free electrons are delocalized across all atoms and contribute to

the electrical nature of CNTs. CNTs can thus be conducting or semi-conducting depending on their chirality [77-79]. The electrical properties of both SWNTs and MWNTs have been relatively well discovered, and interest in this field has increased over the last decade [80,81]. Because of the ballistic nature of electron transport in SWNTs, they can be described as quantum wires, whereas transport in MWNTs is found to be fairly diffusive or quasi-ballistic [82]. CNTs can be used in transistors and other switching applications in advanced electronics due to their electronic nature [83]. The most recent use of nanotubes was as emitters. The important aspect of CNT emitters is that they can emit at lower threshold voltages [84], and they can also be used in sensors, vacuum microelectronics, and X-ray generation [85,87].

1.6.3. Thermal properties

CNTs are significant not only for their electronic and mechanical properties, but also for their thermal properties, which are related to their graphitic nature as well as their unique structure and size [88]. At room temperature, the thermal conductivity of individual MWNTs was measured and found to be 3,000 W/m K (higher than that of graphite). A similar study was conducted for SWNTs, and the result was greater than 200 W/m K for SWNTs [89]. The incorporation of pristine and functionalized nanotubes into various materials may result in a twofold increase in thermal conductivity for a loading of only 1%, demonstrating that nanotube composite materials can be useful for thermal management applications in industries [90]. The thermal conductance of carbon nanotubes (CNTs) is affected by their quality, the number of structural defects and morphology, the presence of impurities in the CNTs, and their diameter distribution [91].

1.7. Purification of Carbon Nanotubes

Purification of carbon nanotubes is a process that separates nanotubes from non-nanotube impurities in raw materials or from nanotubes with an unfavorable number of walls. Impurities such as amorphous carbon, catalysts, catalyst supports, carbon nanoparticles, and unwanted nanotubes such as a small amount of MWNTs in a raw SWNTs sample or SWNTs in DWNTs samples are examples of these impurities [92,93].

There are numerous methods and procedures for purification depending on the technique of carbon nanotube synthesis. The following steps are common to all purification procedures: filtration to remove large graphite particles and aggregations, dissolution in appropriate solvents to eliminate catalyst particles (concentrated acids as solvent) and fullerenes (use of organic solvents), and microfiltrations and chromatography to size separation and removal of amorphous carbon clusters [94]. Purification techniques are divided into three categories: physical, chemical, and a combination of chemical and physical methods [95]. Chemical methods separate the synthesis products based on their reactivity, which normally introduces unavoidable defects along the tubes and at the tube ends, causing significant damage to the structure and morphology of the CNTs, or causing the removal of metal catalyst particles through purification of CNTs , on the other hand, with proper control of the reaction conditions, may result in higher purity as well as tip opening. Chemical purification methods include heating oxidation, acids and oxidizing agents, alkali treatment, and annealing in inert gases. Physical methods, on the other hand, such as ultrasonication, filtration, centrifugation, and size-exclusive chromatography, separate impurities based on their size. These processes are typically more complex and less effective, despite the fact that they are relatively mild and do not cause severe damage to the tubes [96].

The oxidation of as-synthesized CNTs in both wet and dry conditions is the most commonly used chemical purification method. The wet condition generally refers to oxidation using a solution of concentrated acids or strong oxidants, whereas the dry condition primarily refers to controlled temperature oxidation using air, oxygen, or other gases. The central concept of this approach is a selective oxidative etching process, which is based on the fact that amorphous carbon and carbon particles can be eliminated more easily than CNTs due to their faster oxidation reaction rate. The high oxidative activity of amorphous carbon is due to the presence of high-energy hanging bonds that can be easily oxidized. Meanwhile, the higher reactivity of carbon nanoparticles can be attributed to their large curvature and pentagonal carbon ring [97,98].

Simultaneously, the structures of different CNTs have an undeniable effect on their oxidation rate. Singlewalled carbon, such as C60, is more easily oxidized, and its reactivity increases with decreasing diameter. [99]. The tips of the nanotubes may open due to oxidation. The pentagonal carbon ring nanotube tips are less chemically stable than the hexagonal carbon ring tube cylinder. While the CNTs are oxidized during the purification process, the presence of five-membered rings in the hexagonal array at the CNTs tips makes this region susceptible to oxidative reactions, presumably on the double bonds connecting two pentagons [101]. Potassium permanganate ($KMnO_4$), hydrogen peroxide (H_2O_2), and other oxidants are commonly used in the treatment [101-103] . Carbon surfaces have also been oxidized with metal cations with a high oxidation potential. The degree of oxidation is determined by the system's redox potential as well as the structural features of the nanotubes, which include curvature, pentagon, heptagon ring position, helicity, and many other factors. [104]. H_2O_2 hydrogen peroxide was

discovered to be a promising oxidant capable of attacking the carbon surface without destroying the pristine structure of the CNTs, requiring less washing time, and producing water as a by-product [105].

$$C + 2H_2O_2 \rightarrow CO_2 + 2H_2O \qquad \text{-------(1.1)}$$

1.8. Functionalization of Carbon Nanotubes

CNTs have an inert surface, but they are generally insoluble in solvents due to the strong Vander Wall interaction that tightly holds them together in bundles. Many other applications will benefit from increased solubility due to a process known as functionalization. The functionalization method will be divided into two major groups:

1.8.1. Non-covalent functionalization

CNTs functionalization methods based on non-covalent interaction can be carried out without destroying the intrinsic sp^2 hybridized structure of the nanotube sidewall, preserving the original electronic structure and properties of CNTs. Various non-covalent functionalizations have been investigated. CNTs could be non-covalently functionalized through π-π stacking interactions between conjugated molecules and the graphitic sidewall of CNTs [106,107]. CNTs are functionalized non-covalently by aromatic compounds, surfactants, and polymers, with the majority of interactions involving stacking or hydrophobic interactions. Non-covalent modifications of CNTs can do a lot to preserve their desired properties while improving their solubilities dramatically in these approaches. Aromatic molecules such as pyrene, porphyrin, and their derivatives, can and do interact with the sidewalls of carbon nanotubes via stacking interactions, paving the way for non-covalent functionalization of carbon nanotubes .Dai and colleagues described a general and appealing

approach to non-covalent functionalization of CNTs sidewalls and subsequent immobilization of biological molecules onto CNTs with a high degree of control and specificity [108].

1.8.2. Covalent functionalization

Carbon nanomaterials are relatively unreactive to chemical treatment due to characteristics such as low curvature, low solubility, and bundling. So far, several methods for covalent functionalization of CNTs have been proposed. The strategies for covalently functionalizing CNTs can be divided into two categories based on the location of the functional groups: defect and sidewall functionalizations. When compared to non-covalent methods of nanotube functionalization, covalent methods are more robust and controllable. CNTs synthesized using any available method are not defect-free. Intrinsic defects include five- or seven-membered rings known as Stone–Wales defects, sp^3 hybridized defects, and vacancies in the sidewall's sp^2 hybridized six-membered ring carbon structure [109,110]. CNTs can tolerate a limited number of defects without losing their macroscopic electronic and mechanical properties [111,112]. Furthermore, because of their higher curvature, the tips of the tubes that form a hemispherical fullerene have greater reactivity than the sidewalls [113,114]. CNTs could be opened and cut into short tubes when exposed to strong oxidizing agents such as nitric acid, $KMnO_4/H_2SO_4$, O_2, $K_2Cr_2O_7/H_2SO_4$, or OsO_4. Defects were introduced around the CNTs surface in the meantime [115,116]. Furthermore, the oxidization process generated oxygenated functional groups such as carboxylic acid, ketone, alcohol, and ester groups at the ends and defect sites of the nanotubes [117]. These functional groups were critical in further functionalizing CNTs. Sonication could also result in defects on the sidewalls of CNTs that were eager for additional chemical reactions [118,119]. Direct

covalent sidewall functionalization is associated with a shift in hybridization from sp^2 to sp^3 and a simultaneous loss of the p-conjugation system on the graphene layer. This process can be created by reacting with molecules with high chemical reactivity. Fluorination, radical addition, nucleophilic addition, electrophilic addition, and cycloaddition are examples off sidewall reactions [120].

1.9. Semiconductors

Certain substances are neither good conductors (metals) nor good insulators (glass). Semiconductors are materials with crystalline structures and very few free electrons at room temperature. It acts as an insulator at room temperature. Its resistivity is intermediate between that of a conductor and that of an insulator. Controlled conductivity can be achieved by adding appropriate impurities to semiconductors. Silicon, germanium, carbon, and other semiconductors are examples.

Semiconductors, which include transistors, solar cells, light-emitting diodes (LEDs), and digital and analog integrated circuits, are the fundamental building blocks of modern electronics[121]. A semiconductor material's electrical conductivity increases with increasing temperature, which is the opposite of a metal's behavior. Semiconductor devices can have a variety of useful properties, including the ability to pass current more easily in one direction than the other, variable resistance, and sensitivity to light or heat. Devices made from semiconductors can be used for amplification, switching, and energy conversion because the electrical properties of a semiconductor material can be modified by the controlled addition of impurities or by the application of electrical fields or light. Current flow in a semiconductor is caused by the movement of free electrons and "holes," which are referred

to collectively as charge carriers. Doping a semiconducting material with impurity atoms greatly increases the number of charge carriers within it. When a doped semiconductor contains mostly free holes, it is referred to as "p-type," while when it contains mostly free electrons, it is referred to as "n-type." To control the location and concentration of p-and n-type dopants, semiconductor materials used in electronic devices are doped under precise conditions. A single semiconductor crystal can have numerous p- and n-type regions; the useful electronic behavior is caused by the p–n junctions that connect these regions [121,122].

Titanium oxide is a common n-type semiconductor. It exists in three crystalline forms in nature: brookite (orthorhombic), anatase (tetragonal), and rutile(tetragonal) as shown in Figure(1.11). The first is extremely rare, Rutile is stable at high temperatures, whereas anatase does not. The temperatures at which the different phases transition are as follows: rutile –brookite; 500-600 °C, anatase – rutile; 850 °C. The crystal structure of titanium oxide is determined by the arrangement of octahedrons and the manner in which individual TiO_6 units are connected. For rutile, neighboring octahedral share one corner and are arranged along the long axis with mutual twisting of 90^o. In the case of anatase, the next octahedra share a common edge, and in brookite, the point of attachment is both a corner and an edge [123-125]. The majority of the research focuses on anatase and rutile. Rutile is made up of parallel chains of slightly deformed octahedrons, each of which is connected to ten neighboring units. Octahedrons in the anatase have prism warpage, and each octahedron is connected to eight other octahedrons. Ti-Ti distance is longer in anatase and Ti-O distance is shorter than in rutile. Rutile has greater thermal stability than anatase, but anatase has more stable morphology for nanostructures of 10–20 nm [126,127]. Anatase phase

has a higher band gap (3.2 eV) than rutile (3.0 eV), providing equal open circuit voltage for the same redox couple electrolyte, but rutile has a 30% lower short-circuit current [128]. Furthermore, anatase is more photoactive, has a higher refractive index, and has a higher electron diffusion coefficient than rutile. In a mixed phase of anatase and rutile, the inactive rutile enhances the photocatalytic activity of anatase [129-131]. It has been reported that a mixture of anatase and rutile phases is more active than either pure phase alone [132,133]. In addition, the highly efficient commercial photocatalyst Degussa (Evonik) P25 is primarily composed of the anatase phase (80%) with a reasonable amount of rutile (15%). Because a synergetic effect between anatase and rutile phases is frequently not observed when separately synthesized powders are simply mixed together, close contact of the phases is expected to be required [134,135]. The separation of photoexcited charge carriers between the two phases has been attributed to the high activity of the phase mixture [136,137].

Anatase is considered an active component in mixed phase TiO_2 due to its higher activity than rutile [138], whereas rutile is traditionally thought to act as an electron sink due to its lower conduction band energy than anatase. In contrast, an electron spin resonance (ESR) study in mixed phase P25 revealed that photoexcited electron transfer occurred from the rutile conduction band to the anatase conduction band [139]. This is due to the fact that the anatase trapping sites are located below the energy level of the rutile phase's conduction band [132]. However, in an attempt to explain electron transfer from the rutile conduction band to that of anatase, recent calculations and X-ray photoelectron (XP) spectroscopy studies revealed that the rutile conduction band is 0.4 eV higher than that of anatase [140,141]. Although there is some disagreement about the

alignment of the conduction band minima of the rutile and anatase phases [140,142,143]. TiO_2 is the most commonly used material for DSSC photoanodes because it is inexpensive, non-toxic, has good electrical properties, and has long-term chemical stability [144]. The benefits of titanium dioxide thin films include a high refractive index (over 2.3) and excellent transparency (over 90%) over a wide spectral range (from about 320 to about 6000 nm). TiO_2 has many desirable properties in addition to its good optical properties, such as high mechanical resistance and long-term stability. As a result, titanium oxide thin films are widely used in optics and photovoltaics as anti-reflective coatings [145-147].

Anatase titanium dioxide is the most commonly used form in dye-sensitized solar cells (DSSC). A semiconductive oxide layer with a nanocrystalline structure is used to increase the active surface of light absorption. If the surface is smooth and covered with a monolayer of dye, the amount of incident monochromatic light absorbed is less than 1%. Titanium dioxide must have an n-type conductivity in order to conduct electrons transferred from the sensitizer in a DSSC [148]. This oxide is regarded as the best material for covering the DSSC electrode due to its wide energy bandgap and sufficiently low position of the conduction band edge in relation to the redox potential of organic substances in aqueous solution. As a result, dyes that absorb light in the visible range can be used. The surface development of the layer and the size of the pores present in the layer are two parameters that must be chosen so that the guaranteed performance is maximized light absorption and freely filling the pores by the electrolyte [149].

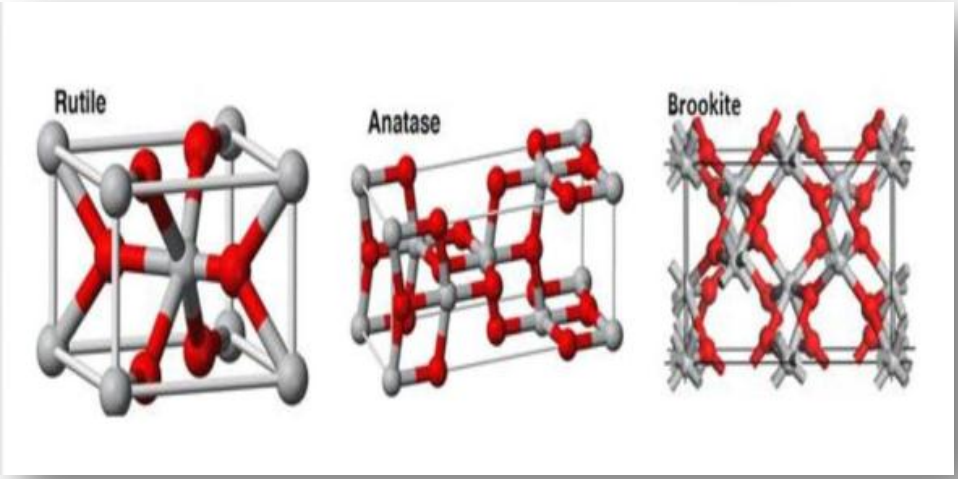

Figure (1.11): The crystal structures of rutile, anatase, and brookite [150].

1.10. TiO_2/CNTs Nanocomposites

Carbon nanotubes (CNTs) and their composites have received a lot of attention in recent years due to their unique physical and chemical properties [151-153], which make them not only widely used in catalysts [154], nanoelectronic devices [155,156], solar cells [157], hydrogen storage materials [158], and supercapacitors, but also have potential applications in sensors [159]. The use of carbon nanotubes in composite applications is heavily reliant on their ability to be homogeneously dispersed throughout the matrix without compromising their safety, and good interfacial bonding is required to achieve load transfer across the CNTs–matrix interface, which is a necessary condition for improving the composite's mechanical properties [160]. Load transfer from matrix to CNTs plays an important role in the mechanical properties of composites when the adhesion between the matrix and the CNTs is insufficient to sustain high loads, resulting in the loss of the benefits of CNTs' high tensile strength [161]. The combination of the unique properties of CNTs and semiconductor nanostructures results in the formation of a new class

of nanocomposite materials, which opens up a new range of applications in various fields of science [162,163]. Many studies have been conducted to investigate the growth of metal oxide nanoparticles using CNTs as a 1D template. ZnO, TiO_2, SnO_2, CdS, CdSe, and CdTe nanoparticles decorated on the wall surface of CNTs are appealing semiconductors due to their unique properties, which make them candidates in a variety of applications such as photoelectrochemical solar cells, gas sensors, and photo-detectors [164].

1.11. Applications of CNTs

CNTs are the most rapidly growing nanomaterials in the field of nanotechnology because they have a wide range of applications, including materials science, medicine, electronics, and energy storage [165,166]. Many appealing applications of CNTs can be achieved by using CNTs for applications requiring conductivity and high absorption capacity, as well as for the creation of high-strength composites, fuel cells, energy conversion devices, field-emission devices, hydrogen storage devices, semiconductor devices, and solar cells [167].

1.12. Solar Cells

A solar cell, also known as a photovoltaic cell, is an electrical device that converts light energy directly to electricity via the photovoltaic effect [168]. Solar cells are the basic components of photovoltaic modules, also known as solar panels. In today's world, fossil fuels produce the majority of the energy, but these fuels also emit extremely dangerous and hazardous gases, such as carbon monoxide, which pollute the environment every second. As a result, solar cells are used to generate clean energy that is both environmentally friendly and does not disrupt the economic balance. Solar cells, which convert solar energy into

electrical energy and can be stored in batteries through charging, can be manufactured to use more solar energy. The operation of a solar cell is dependent on several factors, including: [169,170].
-light absorption to create electron–hole pairs.
-The separation of charge carriers of diametrically opposed types.
-Separation of electrons and holes, as well as charge carrier collection.

Named Solar cells are named after the semiconducting material from which they are made, materials must have specific properties in order to absorb sunlight. Some of these cells are intended for use on the Earth's surface, while others are intended for use in space [171] .

1.12.1. Mechanism of solar cell

Solar cells work by transitioning free electrons gained by gaining extra energy when photons from the sun strike the film surface. After examining the band structure of a solar cell, it was discovered that when the cell gains energy from photons and generates free electrons, which recombine to generate some photovoltaic current, the binding energy of the film decreases, indicating that the maximum number of electrons are generated. As a result, the thin film-based method must be used to increase the efficiency of solar cells. which absorbs a large amount of light and thus covers a larger portion of the solar spectrum [172].

The solar cell theory works in the following steps:

(1) Photons from the sun strike the solar panel and are absorbed by semiconducting materials such as silicon and germanium.

(2) Electrons that have been excited (charged negatively) from their current molecular or atomic orbitals. Once excited, these electrons can either lose their energy and return to their orbital, or they can travel

through the cell until they reach an electrode, where current begins to flow through the material to cancel the potential and this electricity is captured. Because of the special composition of solar cells, electrons are only allowed to move in one direction.

(3) A solar cell array converts solar energy into direct current (DC) electricity that can be used [173,174].The semiconductor materials used in solar cells are distinguished by their intermediate electrical conductivity between a conductor and an insulator [175].

1.12.2. Types of solar cells

There are various methods of classifying photovoltaic cells based on their semiconductor materials, morphology, and fabrication technique, which can be easily studied into three main categories called generations that have been developed to date [176,177].

Since Chapin and Fuller discovered the principle of producing electricity from the sun's rays using a photovoltaic process in the 1960s [178], the trend has been dominated by silicon (Si) solar cell fabrication technology, also known as "first generation". It is distinguished by the rising cost of raw materials in the Si solar cell, followed by the "second-generation" technology, which is characterized by a thin layer (thin film), and other solar cells made of a-Si, CdTe, and $CuInSe_2$ (CIS). With the advancement of technology and solar cell fabrication, a type of solar cell has emerged that uses abundant natural raw materials, is non-toxic, and is capable of producing high efficiency while being fabricated with a simpler process; this type is known as the "third generation," and one of these types is the Dye-sensitized Solar Cell (DSSC), the operating principle of which is a dye reaction. "Fourth-generation" is an abbreviation for "fourth generation" (4GEN). It combines the low cost

and flexibility of polymer thin films with the stability of novel inorganic nanostructures such as metal nanoparticles and metal oxides, or organic-based nanomaterials such as carbon nanotubes, graphene and its derivatives [179,180]. Furthermore, there is disagreement about the fourth generation, with some authors believing it to be part of the third generation and the rest believing it to be different [179,181].

1.13. Dye-Sensitized Solar Cell (DSSC)

This type of solar cell is expected to be able to supply alternative energy concepts at a lower cost of production and with a simpler fabrication technology than its predecessors, which are made from crystalline silicon [176,179,180]. This cell is made up of five distinct layers :

1-A transparent anode made from a glass sheet and treated with a transparent conductive oxide layer (TCO glass) (for example, fluorinated tin oxide (FTO) SnO_2: F coated glass).

2-A mesoporous oxide layer (typically TiO_2) is deposited on the anode to improve electronic conduction.

3-A charge-transfer dye monolayer that is covalently bonded to the surface of the mesoporous oxide layer to promote light absorption.

4-A redox mediator in an organic solvent must be present in an electrolyte to improve dye regeneration.

5-A cathode made of a crystal coated with a catalyst (usually platinum) to facilitate electron collection [181]. Figure (1-12) depicts a typical DSSC construction.

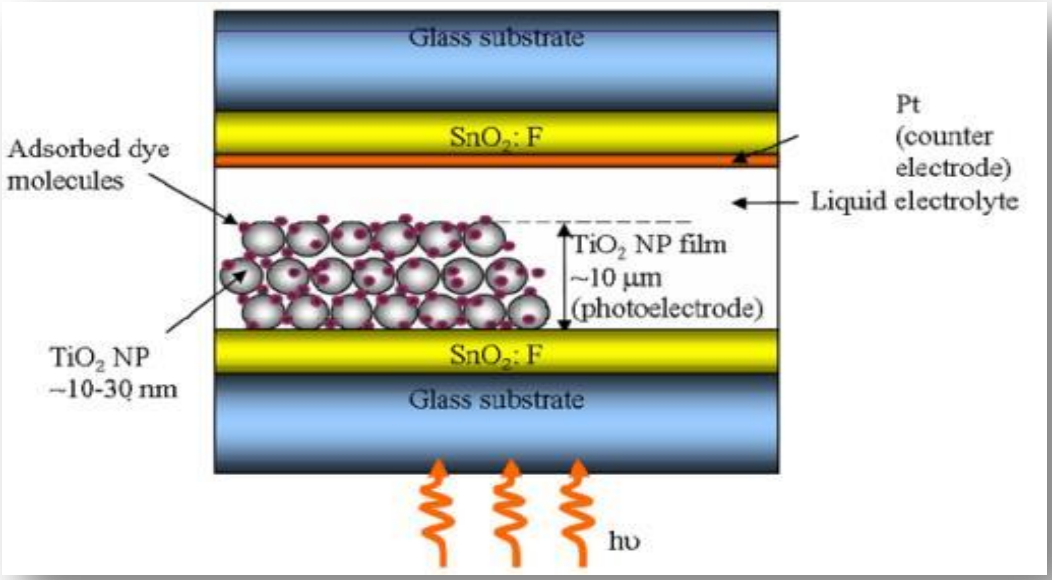

Figure (1.12): Depicts a typical DSSC construction [25].

1.13.1. Transparent conducting substrate

Because of their low cost, abundance, and high optical transparency in the visible and infrared regions of the solar spectrum, transparent conducting substrates, or TCO glass, are commonly used as DSSC substrates. The TCO glass is created by doping bare glass with a metal oxide thin film. electrically conductive TCO coatings that are fluorine doped are the most common type. Tin oxide-FTO (SnO_2:F, FTO) and indium tin oxide ITO (In_2O_3:Sn, ITO). Because of its superior thermal stability at high temperatures, fluorine-doped tin oxide (FTO) glass is used in DSSCs instead of indium tin oxide (ITO) coated glass. The TCO substrate's conducting film sheet resistance is typically 10-20Ω per square area.

1.13.2. Nano crystalline semiconductor film photoelectrode

The photoelectrode (or photoanode) in a DSSC is formed by depositing a thin layer of sensitized wide-band gap nanostructured semiconductor

(typically TiO_2, ZnO, SnO_2, and Sb_2O_5) onto the TCO substrate. To achieve high light-harvesting efficiency (LHE), the nanostructured semiconductor layer must have a large surface area (high roughness) to allow a large number of sensitizer molecules to adsorb [182,183]. Anatase titanium dioxide is the most commonly used form in dye-sensitized solar cells (DSSC). A semiconductive oxide layer with a nanocrystalline structure is used to increase the active surface of light absorption. If the surface is smooth and covered with a monolayer of dye, the amount of incident monochromatic light absorbed is less than 1%. Titanium dioxide must have an n-type conductivity in order to conduct electrons transferred from the sensitizer in a DSSC [184]. This oxide is regarded as the best material for covering the DSSC electrode due to its wide energy bandgap and sufficiently low position of the conduction band edge in relation to the redox potential of organic substances in aqueous solution. As a result, dyes that absorb light in the visible range can be used. The surface development of the layer and the size of the pores present in the layer are two parameters that must be chosen so that the guaranteed performance is maximized light absorption and freely filling the pores by the electrolyte [185].

1.13.3. Dye sensitizer

To sensitize the wide-bandgap nanostructured photoelectrode, dye molecules are used. When illuminated, an electron from the ground state (S^0) of a dye molecule is boosted to the excited state (S*) and then injected into the nanostructured TiO_2 conduction band. The dye molecules should meet some essential requirements based on the DSSC principle in order to promote a high light-to-energy conversion efficiency. To ensure efficient electron injection into the TiO_2 conducting band and to prevent gradual leaching from the electrolyte, the dye molecules must

bind strongly to the surface of the TiO_2 nanostructure [186]. The excited state of the dye must be slightly higher than TiO_2's conduction band, but not by much, to provide a driving force in energy for efficient charge injection into the TiO_2, and the ground state must be sufficiently low in energy to allow for efficient regeneration of the oxidized dye by the redox electrolyte. The dye should absorb light in the visible or near-IR ranges, ideally across a wide range of wavelengths. The electron transfer process from the dye to the TiO_2 must be fast enough to compete with unwanted recombination to the dye's ground state [186,187]. A wide variety of metal complexes and organic dyes have been synthesized and used as sensitizers. The outstanding solar light absorber and charge transfer sensitizer, however, is cis-Di(thiocyanato)bis(2,2'-bipyridyl)-4,4'-dicarboxylate) ruthenium(II), coded as N_3, N-719, and black dyes (structure shown in Figure 1.9). This type of dye has a conversion efficiency greater than 10% [188,189].

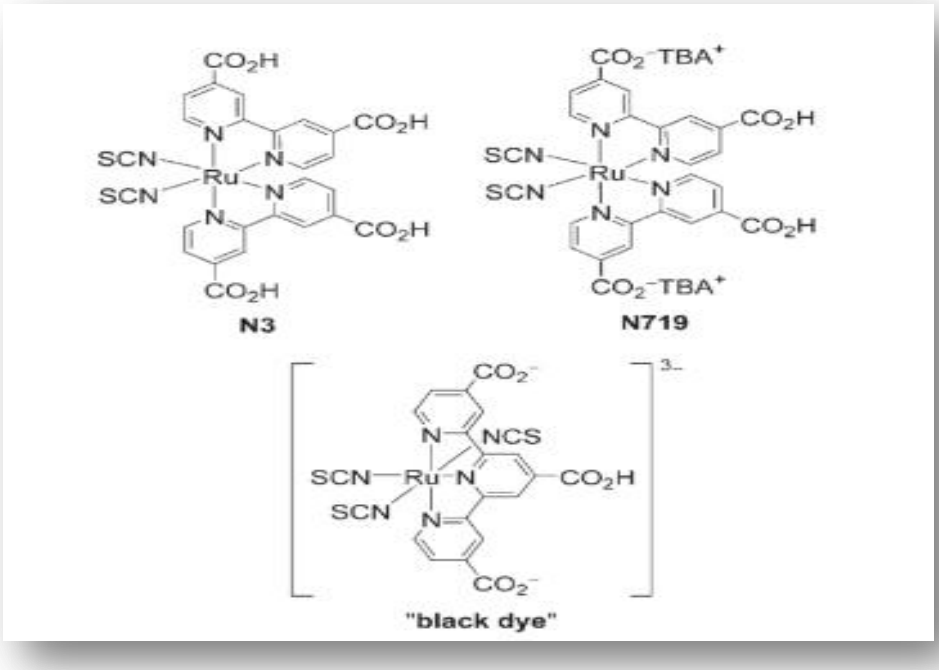

Figure (1.13): Examples of some Ru{polypyridyl dyes used in DSSCs that give cell efficiencies of over 10 %. TBA = tetra-n-butylammonium [190].

Natural dyes have also been used in DSSCs because of their low cost, ease of extraction, nontoxicity, and environmental friendliness [191] . Anthocyanin, chlorophylls, carotenoids, flavonoids, and cyanines are among the dyes found in this plant [192] . Anthocyanin is a natural plant pigment that is also referred to as flavonoids [193]. Anthocyanin pigment responsible for giving red, violet, blue, and orange color to many fruits, vegetables, grains and flowers extracted from them. The color of the natural anthocyanin pigment depends on its pH, so it appears red at (PH<3) and violet at (pH=7-8), so its color changes from bright red to blue when the numbers of the basic hydroxyl group increase (pH>11), as in the figure (1-14). This is often attributed to a change in its molecular structure due to the ionic nature of this dye and what caused the difference in pH values [194,195].This dye in dark pomegranate juice was notable for its abundance in comparison to other plants [196] .

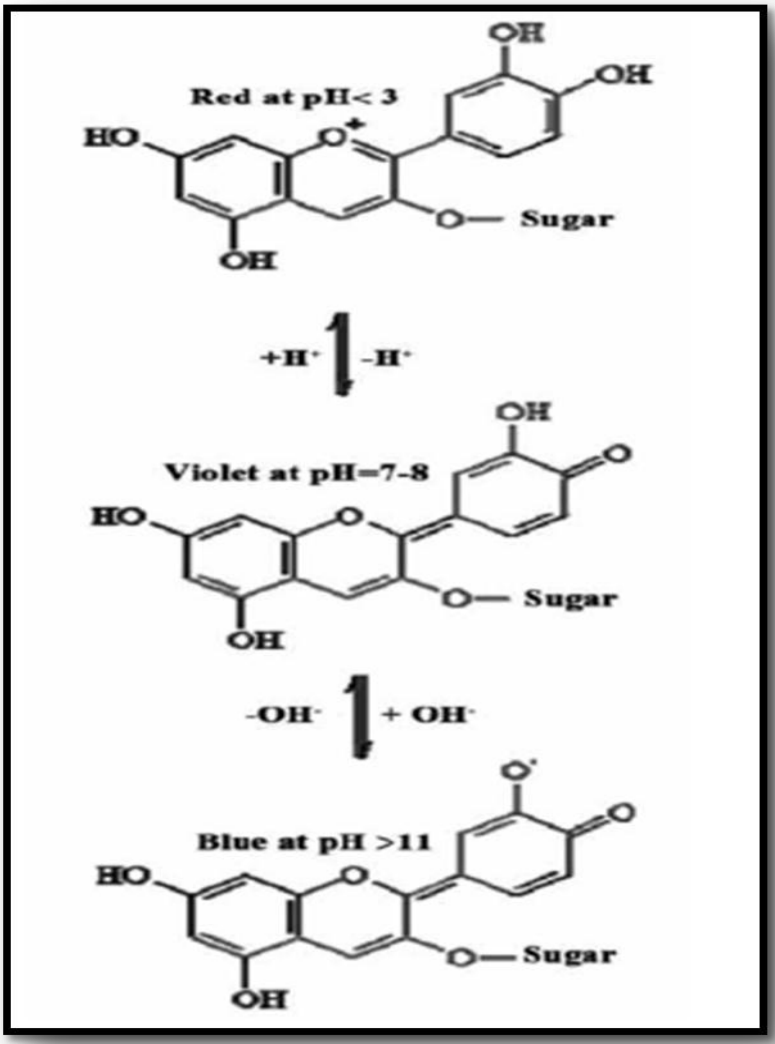

Figure (1.14): The chemical structure of anthocyanin pigment in acidic media, neutral and basic [194].

1.13.4. Redox electrolyte

One of the most important components in DSSCs is the electrolyte [197]. The electrolyte is responsible for the inner charge carrier transport between electrodes and continuously regenerates the dye and itself during DSSC operation, and the electrolyte has a significant impact on the light-to-electric conversion efficiency and long-term stability of the devices [198]. Another definition of an electrolyte is a material that provides pure

ionic conductivity between the positive and negative electrodes of an electrochemical device [199]. The electrolyte properties have a strong influence on the long-functional life-time stability of DSSCs. As a result, the electrolyte must have the following properties [200,201].

1.High electrical conductivity and low viscosity for faster electron diffusion.

2. The nanocrystalline semiconductor and the counter electrode have excellent interfacial contact.

3. It should not be the cause of dye desorption from the oxidized surface or dye degradation.

4. It must not absorb light in the visible spectrum .

Solid state electrolytes, liquid electrolytes, and quasi solid state electrolytes are the three types of DSSC electrolytes [202-204] . Because of its excellent solubility, rapid dye regeneration, low absorbance of light in the visible region, suitable redox potential, and very slow recombination kinetics between injected electrons into the semiconductor and triiodide, iodide / triiodide ($^{-}I/I_3^{-}$) in a solvent is commonly used as an electrolyte in a DSSC [205].

1.13.5. Counter electrode

The counter electrode is used for electrolyte regeneration. The oxidized electrolyte diffuses towards the counter electrode, where electrons from the external circuit are received. To accelerate the reduction reaction, a catalyst is required, and platinum (Pt) is a preferred catalyst due to its high exchange current density, good catalytic activity, and transparency. The CE's performance is determined by the method of Pt deposition on the TCO substrate [200,206]. Recently, a variety of carbon materials such as graphite, carbon black, and carbon nanotubes (CNTs) have been studied as possible alternatives to platinum (Pt) for counter-electrodes

with a relatively low cost for DSSC [207]. Not only are carbon materials abundant, but they are also known to be highly corrosion-resistant [208,209].

1.14. The operational principle of the DSSC

The operation of a dye sensitized solar cell is depicted in Figure (1-15), and described below .

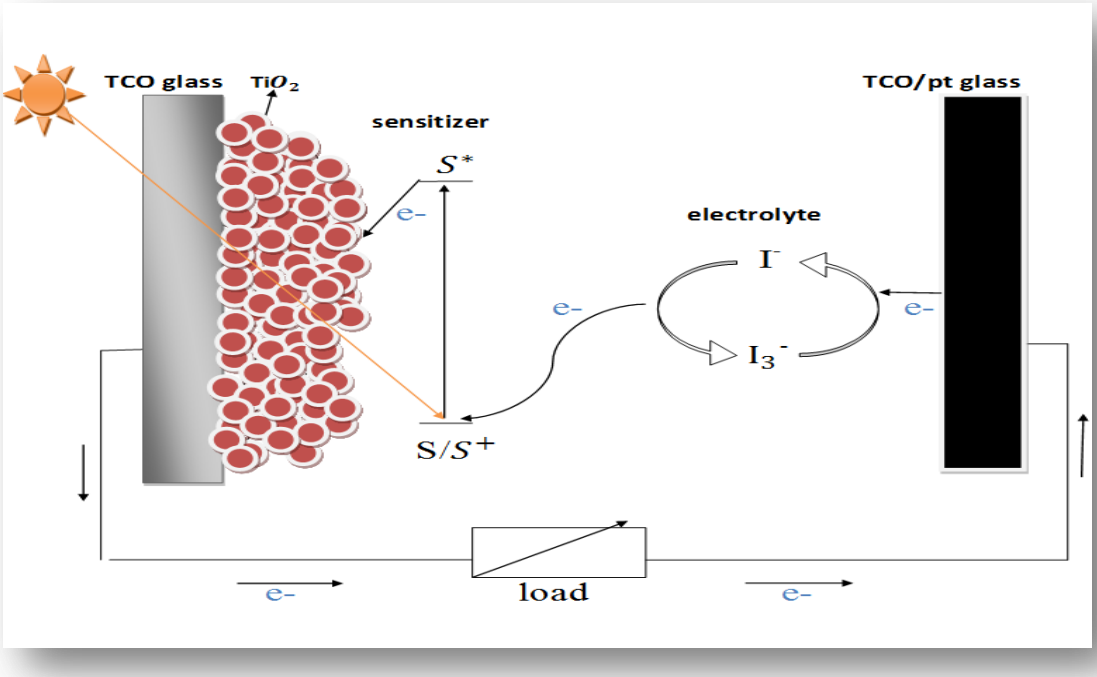

Figure (1.15): A schematic representation of the DSSC's operating principles[210].

1- A photon is absorbed by a sensitizer when it is exposed to light. This causes the sensitizer to be excited to the excited state (S*) .

$$S + h\upsilon = S^* \qquad \text{----(1.2)}$$

(Light absorption by a dye molecule)

2- The excited electrons are injected into the TiO_2 conduction band (CB). The sensitizer that has been excited is oxidized to S^+ .

$$S^* \longrightarrow S^+ + e^-_{cb}(TiO_2) \quad \text{----(1.3)}$$

(Charge injection)

3- Meanwhile, electrons diffuse through the nano-crystalline TiO_2 layer to the conducting substrate's back contact and flow through the external circuit to the counter electrode.

$$e^-(TiO_2) \longrightarrow e^-(CE) \quad \text{----(1.4)}$$

(Charge transportation)

4- The electron from the electrolyte then restores the sensitizer's (S) original state via iodide reduction .However, there are two major (unwanted) recombination reactions that reduce the DSSC's conversion efficiency: The excited electron in TiO_2 can directly recombine with the oxidized sensitizer or the electrolyte's oxidized redox couple.

$$2S^+ + 3I^- \longrightarrow 2S + I_3^- \quad \text{----(1.5)}$$

Dye regeneration

$$S^+ + e^-(TiO_2) \longrightarrow S \quad \text{----(1.6)}$$

Recombination

5- The iodide is regenerated at the counter electrode by reducing tri-iodide.

$$I_3^- + 2e^- \longrightarrow 3I^- \quad \text{----(1.7)}$$

Iodine regeneration

When illuminated, the sensitizer is photoexcited in a femtosecond, and electron injection from the excited state dye (S*) into the TiO_2 conduction band (CB) is a sub-picosecond process. The reduction rate of oxidized

dye by the redox electrolyte occurs on a timescale of nanoseconds. Photoinjected CB electrons recombine with oxidized dye molecules or the oxidized form of the electrolyte redox couple (I_3^- ions) in microseconds [211] .

The main negative factor limiting DSSC performance is charge recombination. This happened when the back-electron transfer in the TiO_2 photoanode–electrolyte interface before reaching the collecting electrode, such as fluorine-doped tin oxide (FTO), was assumed to be the main recombination pathway, lowering the efficiency of DSSC [212]. It is predicted that improving the conduction pathways from the photogenerated carriers' location to the collecting electrode would significantly improve DSSC efficiency [213]. As a result, several approaches are used to prevent recombination and improve transport, including (1) the use of a composite semiconductor photoanode with different bandgaps, (2) the insertion of some doping elements in the TiO_2 photoanode, and (3) the incorporation of charge carriers to direct the photogenerated electron [214,215]. paraphrased formalizedThe addition of CNTs to the TiO_2 photoanode improved the efficiency of DSSC to a limited extent [216].

1.15. Current-Voltage (I-V) Measurement

The most important and widely used technique for evaluating photovoltaic performance is the current-voltage measurement of a DSSC. It is carried out on a Keithley 2400 source meter in the presence of simulated sunlight. Figure (1.16): depicts a typical I-V curve. The I-V measurement can be used to calculate the four parameters (Voc, Isc, FF, and η). The short circuit current (Isc) is the current that flows through a solar cell when the voltage across it is zero. The open circuit voltage

(Voc) is the maximum voltage available from a solar cell when the current through the cell is zero [217]. The maximum power (Pmax) is the condition in which the solar cell produces the most power; the current and voltage in this condition are denoted by Imax and Vmax (respectively). The fill factor (FF) and conversion efficiency (CE) are metrics used to assess the performance of solar cells [218]. The fill factor is calculated by dividing Pmax by the product of Voc and Isc. The conversion efficiency is defined as the ratio of Pmax to the sum of the input light irradiance (E) and the surface area of the solar cell (Ac).

$$FF = V_m I_m / V_{oc} I_{sc} \qquad \text{----(1.8)}$$

$$\%\eta = V_{oc} I_{sc} FF / P_{in} \times 100 \qquad \text{----(1.9)}$$

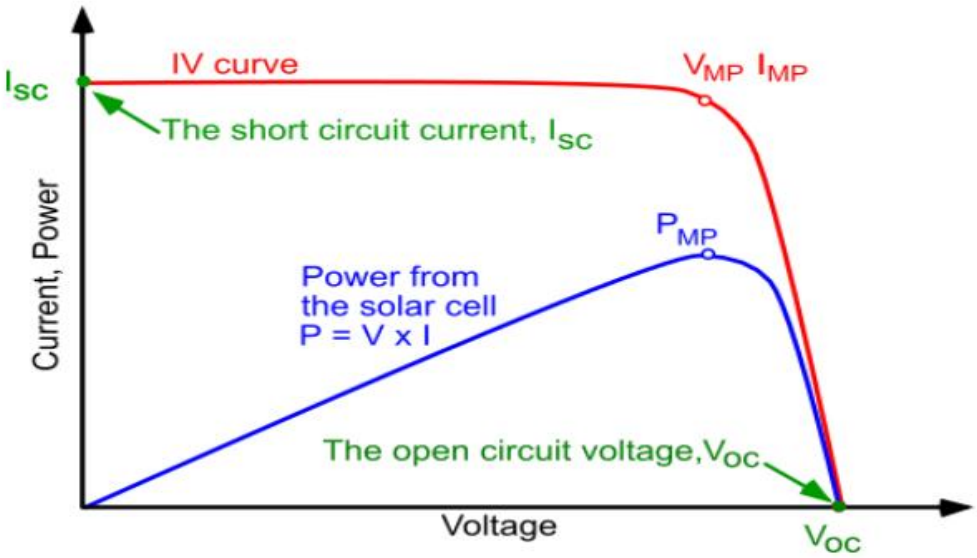

Figure (1.16): Characteristic I-V curve of a DSSC [219].

1.16. Petroleum Analysis

Liquefied petroleum gas (LPG) was used as a source for carbon. LPG is a mixture of light hydrocarbons, most notably propane (C_3H_8) and butane (C_4H_{10}). It is used as a fuel in a wide range of applications around the world, including cooking, heating, power generation, transportation, and has successfully synthesized CNT using it as a carbon source, among many others. However, under moderate pressure, it transforms into a liquid with a much higher energy density, which is advantageous for storage and transportation. LPG is most commonly produced as a byproduct of the extraction and processing of natural gas and crude oil, but it can also be produced as a byproduct of biofuel processing and other industrial processes. However, its composition and constituents can vary depending on the region in which it was produced or intended for sale, as well as the fuel specification followed. The liquefied petroleum gas is analyzed using gas chromatography technology to determine the proportions of carbon components present, which are used to prepare carbon nanotubes [220,221].

Gas chromatography is a popular analytical technique for separating and analyzing gaseous and volatile compounds. To separate the analytes in gas chromatography, the sample is dissolved in a solvent and vaporized. The sample is divided into two phases: the stationary phase and the mobile phase. A chemically inert gas, such as helium or nitrogen, serves as the mobile phase. Gas chromatography is one of the few types of chromatography that does not require the use of a mobile phase to interact with the analyte . The stationary phase can be either a solid adsorbent, as in gas-solid chromatography (GSC), or a liquid on an inert support, as in gas-liquid chromatography (GLC). In gas-solid chromatography, a solid adsorbent is used as a stationary phase, and separation occurs via the

adsorption process, whereas in gas-liquid chromatography, the stationary phase consists of a thin layer of nonvolatile liquid bound to a solid support, and separation occurs via the partition process. The most commonly used technique is gas-liquid chromatography. The to-be-separated sample is first converted into vapours and then mixed with the gaseous mobile phase. Sample components that are more soluble in the stationary phase travel slower, while components that are less soluble in the stationary phase travel faster. As a result, the components are separated based on their partition co-efficient [222] .

1.17. Characterization of the CNTs and its Composites

Several techniques have been adopted to define and understand the structure and nature of carbon nanotubes and its composite with titanium dioxide.

1.17.1. Raman spectroscopy

Raman effect is the inelastic scattering of light by matter. When a monochromatic light is scattered by matter, it undergoes two types of interaction, resulting in two distinct types of scattered light. One type of interaction does not involve the transfer or exchange of energy between the incident light photon and matter molecules or atoms. As a result, the scattered photon has the same energy or frequency as the incident light. This type of scattering is known as Rayleigh scattering because it is elastic in nature . The second type of interaction involves the exchange of energy between the incident photon and the molecules of the material. As a result, the scattered photon will have a new frequency or energy that is simply equal to the sum or difference of the incident photon's frequency and the natural frequency of the thermally excited and kinetically active species in the material. This type of scattering is known as Raman

scattering because it is inelastic in nature. Stokes and antiStokes Raman scattering are the names given to the shifts to lower and higher frequencies, respectively . Stokes Raman scattering occurs as a result of a transition that begins at the ground state vibrational energy level and ends at a higher vibrational energy level, whereas anti-Stokes Raman scattering occurs as a result of a transition from a higher to a lower vibrational energy level. Because most molecular vibrations are in the ground state at room temperature, anti-Stokes transitions are less likely to occur than Stokes transitions, resulting in more intense Stokes Raman scattering [223]. With a frequency range of 100-4000 cm^{-1}, the appropriate spectrum and Raman intensity are 0.001 percent of the intensity of the source.The Raman spectrum is used to investigate vibrational and rotational modes in a system. It is also used for all types of samples (solid, liquid, and gas). Many carbon materials with varying degrees of sp^2 structures as a type of symmetric model have had their Raman spectra extensively studied [224,225].

Raman spectroscopy is a tool for characterization of carbon nanotubes and functionalized carbon nanotubes, and it is one of the most widely used methods for characterization of carbon nanotubes[226] . The radial breathing modes (RBMs) caused by the higher frequency of disordered D, the G graphite network, and the G^- (second-order Raman scattering from D^- band variation) modes are the most notable Raman features in CNTs. The D, G, and G^- modes are found in graphite, while the RBM is unique to CNTs and represents the tube's isotropic radial expansion. Because the RBM frequency is inversely proportional to the diameter of the tube, it is useful for determining the diameter distribution in a sample. The RBM bands can be used as a diagnostic tool to confirm the presence of CNTs in a sample. Raman spectroscopy was used to evaluate the

composite of CNTs with different materials, which shows the state of dispersion and the polymer-filler interactions reflected by shifts or width changes of the peaks [227].

1.17.2. Diffraction Technique

The diffraction technique works by focusing a monochromatic ray beam on a material sample in order to obtain structural information hidden in its crystal lattice [228]. X-ray powder diffraction (XRD) and energy dispersive X-rays diffraction (EDX) are two diffraction techniques used in this study. EDX provides a quantitative estimate of the metal content or impurities of carbon nanotubes [229]. XRD is widely regarded as the most reliable method for crystal characterization [230], but it is not without limitations. The monochromatic beam is created by combining polychromatic beams produced in a cathode ray tube; the monochromatic rays then strike the sample atomic planes. This produces diffracted, transmitted, reflected, scattered, and absorbed beams in accordance with Bragg's law[231]:

$$n\lambda = 2d\sin\theta \qquad \text{----(1.8)}$$

Where n is an integer that defines an order of the diffracted beam, λ represents wavelength of the incident X-ray beam, d means the distance between near atomic planes or d- spacing, and θ represents angle of an incidence X-ray. The Miller indexes characterize the different crystallographic planes in a crystal (hkl). These are three integral numbers that are related to the reciprocal values of the intersection of a given plane with the crystallographic unit cell axes, and they are an indispensable method for the characterization and quality control of structural materials that employs the Debye-Scherrer method [232]:

$$D = k \lambda / \beta \cos\theta \quad \text{----(1.9)}$$

where: *D* is the average crystal size, k is the shape factor depends on the shape of the crystal, and equal to 0.94 for the heterogeneous shape but equal to 0.89 for homogenous shape , λ = 0.154 nm is the X-rays wavelength of Cu Kα , ß is the full width intensity at half maximum of the peak and θ is the Bragg's angle . The XRD patterns for CNTs typically shows two distinct peaks at $2\theta=26^{o}$ when compared to normal graphite at $2\theta = 26.5^{o}$, this peak shows a downward shift due to an increase in the sp^2; C=C layers spacing [233] and $2\theta\approx43^{o}$ appear, which can be attributed to diffraction from the carbon nanotubes' C(001) and C(002) planes. The second peak in MWNTs is stronger than in SWNTs [231].

1.17.3. Thermo Gravimetric Analysis TGA

TGA is a thermal technique that measures changes in material weight as temperature increases [234] . The weight changes represent changes in the materials' physical and/or chemical properties, such as decomposition, oxidation, and volatilization. TGA is frequently used in the investigation of polymeric materials [235]. TGA is one of the simplest techniques for characterizing nanomaterials, particularly carbon-based nanomaterials. Other than drying specimens, TGA typically does not require any special sample preparation. During the thermogravimetric analysis, samples are heated in a specific atmosphere, while the mass loss of the sample is tracked as the temperature rises. TGA has previously been reported as a reliable method for evaluating the thermal stability, purity, and composition of carbon nanomaterials [236,237].

TGA can be used to determine the percentage of amorphous carbon, metal catalyst content, and sample purity in carbon-based nanomaterials

such as carbon nanotubes (CNT) [237]. This TGA test requires approximately 5 to 10 mg of sample, with no special sample preparation required. During the TGA run, amorphous carbon in the sample decomposes at temperatures between 200 and 400°C, which is lower than for graphitic structured carbons (graphene, graphite, carbon nanofibers, single-walled carbon nanotube [SWCNTs], and multi-walled carbon nanotube [MWCNTs]. As a result, the decomposition curve can be used to calculate the amount of amorphous carbon in the sample [238,239]. The oxidation temperature of SWCNTs is typically less than 600 °C. However, some MWCNTs have higher oxidation temperatures [239]. The residual mass after 700°C is regarded as metal catalysts and metal catalyst oxidation products [240,241]. This data can be used to (i) determine the efficacy of the CNTs purification process, (ii) monitor changes in CNTs manufacturing, and (iii) characterize manufactured CNTs for quality control (QC). For example, Mansfield, *et al*. (2014), they used TGA to (1) compare nanoparticle materials produced by different manufacturing processes, (2) identify variability within a single batch, and (3) determine variability from batch to batch. Their findings suggested that TGA is sensitive enough to enable QC at both microscale and nanoscale structures (SWCNTs to MWCNTs) [242] .

1.17.4. Electron Microscopy Technique

Because it allows direct observation of size, shape, and structure, electron microscopy is an essential tool for characterizing CNTs [243]. The most common electron microscopy approaches used for material characterization are TEM, SEM and AFM, with SEM and TEM being mostly used to explain of bundles and the purity of the material. They are, however, limited in the sense that the high electron beam causes damage to the sample. SEM and TEM reveal information about the topography,

morphology, and composition of a material. According to a recent study on the use of AFM, SEM, and TEM for CNTs research, the AFM method provides information about the length of CNTs and the diameter of their bundles; however, the accurate value of the diameter could not be observed because the CNTs did not lie directly on the mica and oscillated under the daze [244].SEM was used to characterize the overall morphologies and dimensions of CNTs. The degree of purity is quantified .TEM detects lattice structures, sidewalls, diameters (both inner and outer), lengths, impurities, and defects in CNTs, and distinguishes CNTs from nanofibers [245,246]. However, AFM supplies imaging with both individual CNTs and CNTs bundles. Accurate 3D reconstruction of the sample topography with atomic resolution at a low cost and in a short period of time [247].

1.17.5. UV-visible Diffuse Reflectance Spectroscopy

The band gap energies of TiO_2 (anatase & degussa P25) and its composites with CNTs were determined using a Cary 100 Scan UV-visible spectrophotometer system and reflectance data R. This is outfitted with a Labsphere integrating sphere diffusing reflectance accessory for measuring diffuse reflectance spectra with $BaSO_4$ as a reference material. The following equation was used to transform the measured reflectance data (R) to the Kubelka-Munk function F (R) [248] :

$$F(R)=\frac{(1-R^2)}{2R} \qquad \text{----(1.10)}$$

$$[F(R).E]^{0.5}=\left[\frac{(1-R^2)}{2R}.E\right]^{0.5} \qquad \text{----(1.11)}$$

where R is the fraction of reflectance. The band gap of the samples is estimated by extrapolating of a tangent line in the plot of $[F(R).h\upsilon]^{0.5}$ versus the photon energy, hυ (h and υ are the Plank's constant and photon frequency, respectively) [249]. After anticipation of the band gaps, the absorpt n edges are calculated by the following equation:

$$E_g = \frac{1239.8}{\lambda} \quad \text{----(1.12)}$$

where *Eg* is the band gap (eV) and λ (nm) is the optical absorption edge.

1.18. Literature Survey For DSSCs

Ahmed M. Ammar *et al.* (2019) here they did three natural dyes were extracted from different fruits and leaves and used as sensitizers for dye-sensitized solar cells (DSSCs). Chlorophyll was extracted from spinach leaves using acetone as a solvent. Anthocyanin was extracted from red cabbage and onion peels using water. Different characterizations for the prepared natural dyes were conducted including UV-vis absorption, FTIR, and steady-state/time-resolved photoluminescence spectroscopy. Various DSSCs based on the extracted dyes were fabricated. The degradation in the power conversion efficiencies was monitored over a week. The effect of the TiO_2 mesoporous layers on the efficiency was also studied. The interfaces between the natural dyes and the TiO_2 layers were investigated using electrochemical impedance spectroscopy. They found that the cell efficiency was 2.23 when using chlorophyll dye but equal to 1.87 when using anthocyanin dye [250].

Yu Jeong Jang *et al.* (2019) They studied the photovoltaic performance of ruthenium-based complex Z907 dye in ss-DSSCs using a solid-state polymerized conductive polymer as hole-transporting material (HTM). We investigated the long-term stability of both liquid and solid-state DSSCs and the findings revealed an improved photovoltaic performance and long-term stability of ss-DSSC. This mainly depends on the transport phenomena of the HTM throughout the interface. The present results (efficiency equal to 6.00) show a pavement for manufacturing highly stable and inexpensive ss-DSSC and the practical use is promising [251].

Charu Pathak *et al.* (2019) in the this work DSSCs were assembled using mixture of natural dyes extracted from pomegranate, beetroot, lemon leaves and spinach leaves and employed as sensitizer for nano-crystalline

TiO_2. The best performing cell gave a Voc of 0.47 V, Jsc of 0.055 mA/cm^2 and η of 0.03 %. [252].

M.Younas *et al.* (2019) in the this work Tungsten oxide/titanium oxide nanocomposites (nWO_3-TiO_2) with three different WO_3-TiO_2 mass ratios (n = 1%, 3% and 5%) were synthesized and used as a photo-anode to fabricate dye sensitized solar cells (DSSC), in conjunction with multiwall carbon nanotube (MWCNTs) as a platinum free (Pt-free) counter electrode. It was observed that [1%WO_3-TiO_2/N719/MWCNT] DSSC exhibited an efficiency enhancement of about 40% as compared to the conventional TiO_2/dye/Pt solar cell, and 18% efficiency enhancement compared to [1%WO_3-TiO_2/N719/Pt] solar cell. The reduced electron-hole (e, h^+) recombination in the nWO_3-TiO_2 nanocomposite due to reduced surface trap states, the increased accumulation of electrons at the photo-anode mediated by the photo-excitation of the dye, the efficient electron transportation and increased light absorption can be attributed to the superior performance of [nWO_3-TiO_2/N719/MWCNT] DSSCs in general [253].

Sancun Hao et al. (2006) reported that the dye-sensitized solar cells(DSSCs) were assembled by using natural dyes extracted from black rice, capsicum, erythrina variegata flower, rosa xanthina, and kelp assensitizers. The short-circuit current (ISC) from 1.142 mA to 0.225 mA, the open-circuit voltage (VOC) from 0.551 V to 0.412 V, the fill factor from 0.52 to 0.63, and maximum power (Pmax) from 58 μW to 327 μW were obtained from the DSSC sensitized with natural dye extracts using liquid electrolyte. In the extracts of natural fruit, leaves and flowerchosen, the black rice extract performed the best photosensitized effect, which was due to the better interaction between the carbonyl

andhydroxyl groups of anthocyanin molecule on black rice extractand the surface of TiO_2 porous film [254].

Prihanto Trihutomo *et al.* (2019) reported that the addition of clathrin protein to the TiO_2 layer was used to increase electron transfer in the semiconductor layer resulting in improved DSSC performance. Clathrin is a protein that plays a role in the formation of transport vesicle membrane in eukaryotic cells. The method used in this study is clathrin protein with a concentration of 0%, 25%, 50%, and 75% added to TiO_2 in DSSC structure. Photovoltaic characteristics of DSSC were measured using a data logger to determine the performance of DSSC, layer morphology was analyzed using Scanning Electron Microscopy (SEM), the element content in DSSC was analyzed using Energy-Dispersive X-ray Spectroscopy (EDS), and functional groups in DSSC layers were analyzed using Fourier-Transform Infrared Spectroscopy (FTIR). The result of this study is the addition of clathrin protein can improve DSSC performance, which resulted in the highest performance of DSSC on 75% clathrin protein addition with , , and . From the results of SEM analysis, it appears that clathrin protein molecules fill the cavities in TiO_2 molecules. EDS analysis shows an increase in carbon, oxygen, and phosphorus content in TiO_2 layers with increasing clathrin protein concentration. FTIR analysis shows an increasingly sharp absorption in the FTIR spectrum of protein-forming functional groups by increasing clathrin protein concentration in DSSC [255].

1.19. Aims of the Study

1- Synthesis of CNTs using flame fragment deposition method (FFD) using Iraqi liquefied petroleum gas (LPG).

2- Synthesis of binary composites having different ratios from combination of TiO_2 and synthesized CNTs.

3- Extraction of dye from pomegranate fruit seeds .

4- Manufacturing low cost dye sensitized solar cells (DSSCs)with high efficiency.

5- Fabrication of dye sensitized solar cells (DSSCs) utilizing the synthesized materials .

6- Utilization of CNTs and CNTs/TiO_2 as a roles in the proposed DSSCs .

2.1. Chemicals

Table (2.1) lists chemical materials that used in this work.

Table (2.1): Chemicals

No.	Chemicals	Purity %	Company supplied
1	Acetone (CH_3COCH_3)	99	S.D. Fine-chem. Ltd., India
2	Ethanol (C_2H_5OH)	99.93	Alfa, Aesar
3	Fluorinated tin oxide glass (FTO)		Thomas Baker INDIA
4	Hexachloroplatinic acid ($H_2PtCl_6.6H_2O$)	99	Evonik, Germany
5	Hydrogen peroxide (H_2O_2)(30%)	95	Sigma-Aldrich
6	Isopropanol ($(CH_3)_2CHCO$)	99	BDH
7	Multi-walled carbon nanotube (MWCNTs)	95	Sigma-Aldrich
8	Nitrogen gas	99.99	Emirates industrial gases
9	Nitric acid (HNO_3)	73	CDH- INDIA
10	Titanium oxide nanoparticles (TiO_2) anatase (10-30 nm)	99.50	Skyspring Nanomaterials Inc. , USA
11	Titanium oxide nanoparticles (TiO_2) degussa (20 nm)	95	Evonik, Germany
12	Triton X-100 ($C_{34}H_{62}O_{11}$)	99	Sigma Aldrich

2.2. Instruments

The used instruments are listed in the following table.

Table (2.2): Used instruments.

No.	Instrument	Company	Location
1	Tube furnace	XIN YOO electronic components co. Ltd.	College of Pharmacy, University of Babylon
2	Sensitive balance	BL 210 S, Satorius	College of Pharmacy, University of Babylon
3	Sonication bath	FALC-Italy	College of Pharmacy, University of Babylon
4	Centrifuge	EBA 20 Hettich	College of Pharmacy, University of Babylon
6	Electrical magnetic stirrer	Heidolph- Mr HeiStandard-Germany.	College of Pharmacy, University of Babylon
7	Furnace	Salden Nabertherm LH30/12 Germany.	College of Pharmacy, University of Babylon
8	Gas Chromatography (GC)	Agilent 7890 A	Dora Refinery
9	Programmable Keithley Electrometer (2400)	Tektronix Company	Physics Department / College of Science / Kufa university
10	Volt-Meter	D T 9208A CE Auto Power	Physics Department /College of Science / Babylon University
11	Scanning Electron Microscopy (SEM)	ZEISS model : Sigma VP	Ferdowsi University of Mashhad /Iran

12	X-Rays Diffraction (XRD)	Siemens model D500	University of Kashan/ Iran
13	Fourier Transform Infrared (FTIR) Spectrophotometer	FTIR- 8400S, Shimadzu Japan	Babylon University/Chemistry Department
14	Thermal Gravimetric Analysis (TGA)	Dsc:STA500, Germany	University of Kashan/ Iran
15	Transmission Electron Microscopy (TEM)	Philips model : CM120	University of Kashan/ Iran
16	Raman Spectroscopy	Horiba Japan	University of Kashan/ Iran
17	Energy Dispersive X-Rays Diffraction (EDX)	Oxford instruments, UK	Ferdowsi University of Mashhad /Iran
18	UV-visible	UV-1650PC Shimadzu, Japan	Babylon University/Chemistry Department
19	Flame Fragmentations Deposition Instrument (FFD)	Homemade instrument	College of Pharmacy, University of Babylon

2.3. Carbon Nanotubes Synthesis

The Flame Fragment Deposition (FFD) method, with a homemade chamber instrument was used for the synthesis of carbon nanotubes (CNTs) using LPG as a carbon source [65,66]. Schematic description of this unit is shown in Figure (2-1).

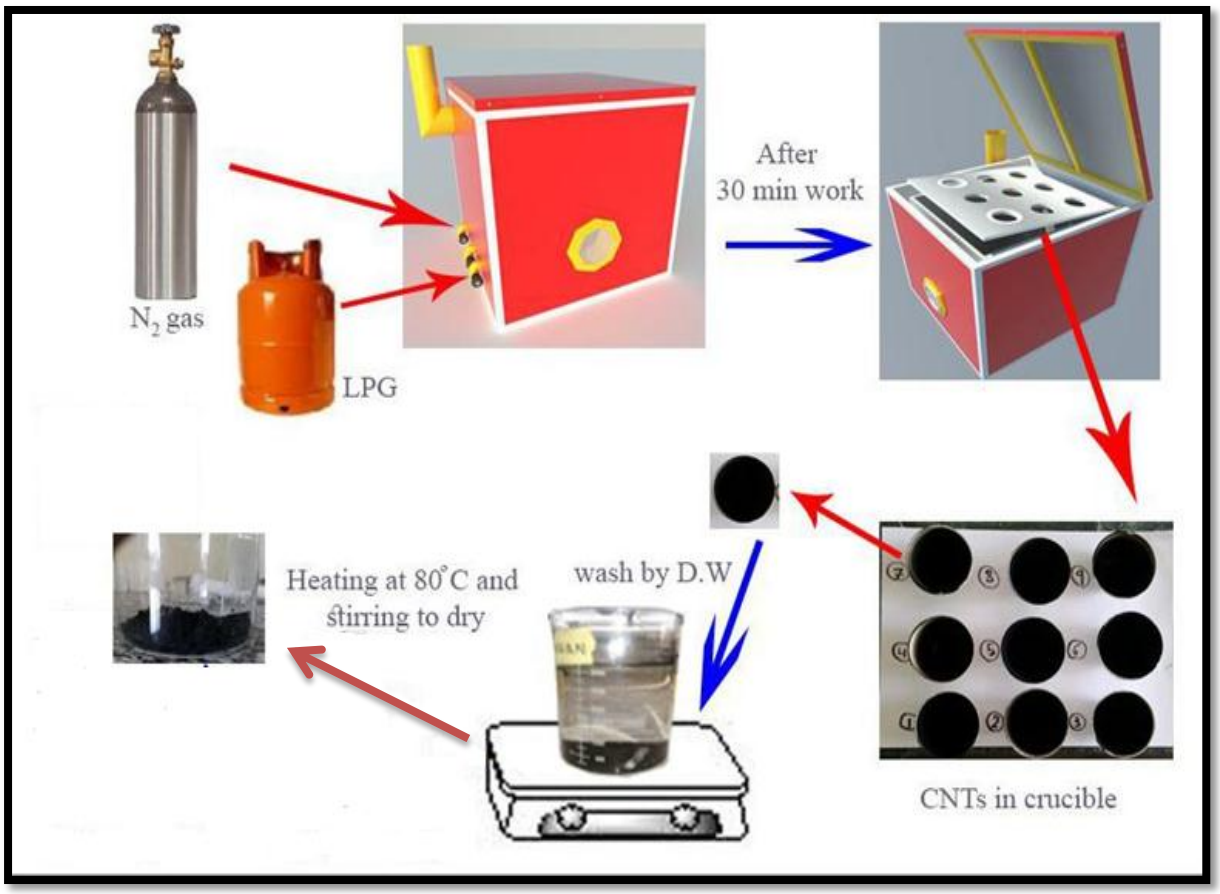

Figure(2.1):Schematic Diagram of The steps used by the Flame Fragmentations Deposition Instrument (FFD) to synthesize CNTs .

2.4. Petroleum Analysis

The model of the gas bottle used as a carbon source in the Dora refinery was analyzed using gas liquid chromatography, and the results are as presented in Figure (2-2).

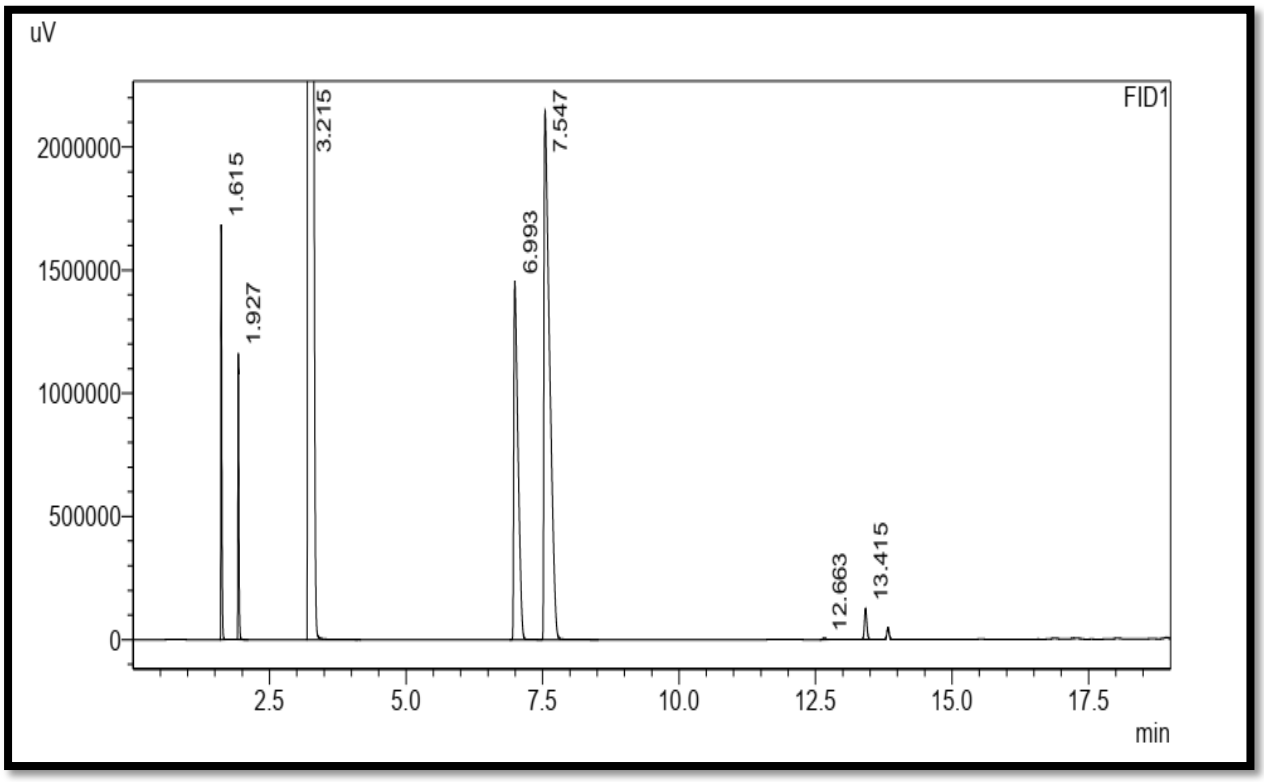

Figure (2.2): Chromatogram of Liquefied Petroleum Gas (LPG) in Dora refinery.

Comparison of time (min.) with area for Liquefied Petroleum Gas (LPG) Compounds in Iraq are shown in Table (2-3).

Table (2.3): Contents of GC (Chromatogram) for LPG in Dora refinary.

Peak	Ret. Time	Area	Height	Conc.	Unit	Mark	Name	Norm. Conc.
1	1.615	1906419	1569752	4.662	%		Methane	5.457
2	1.927	1401262	1110852	1.707	%		Ethane	1.998
3	3.215	79150123	17791261	64.330	%	S	Propane	75.298
4	6.993	7731294	1451862	4.893	%		Iso-Butane	5.727
5	7.547	15278254	2143499	9.633	%	V	N-Butane	11.276
6	12.663	19241	5961	0.010	%		Iso-Pentane	0.012
7	13.415	382573	124537	0.199	%		N-Pentane	0.233
Total		105869166	24207725					

2.5. Purification of synthesized CNTs

The method used in the purification of the synthesized CNTs in this section is a modification of the method described in previous work [65]. Purification of the synthesized CNTs was accomplished in this manner by calcination at 350 ºC for 2 hours, followed by oxidation with hydrogen peroxide H_2O_2 30%, followed by treatment with acetone. In this method, 100 mg of as-prepared CNTs were dispersed in 50 mL of H_2O_2 using an ultrasonic water bath for one hour. The mixture was kept in a refrigerator at 4ºC for 24 hours before being allowed to come to room temperature and gradually heated to 50 ºC until all hydrogen peroxide was removed. The obtained solid was then washed with deionized water and dried at 80 ºC for 6 hours . It was then treated with acetone by dispersing CNTs in 15 mL of acetone and sonicating for 15 minutes, and then the obtained suspension was centrifuged. The obtained solid was dried overnight at 100^{o}C and characterized using X-ray diffraction (XRD), Raman spectroscopy, thermo gravimetric analysis (TGA), Energy Dispersive X-ray Spectroscopy (EDS), and scanning electron spectroscopy (SEM). Purification processes that were utilized in this work are shown in Figure (2.3).

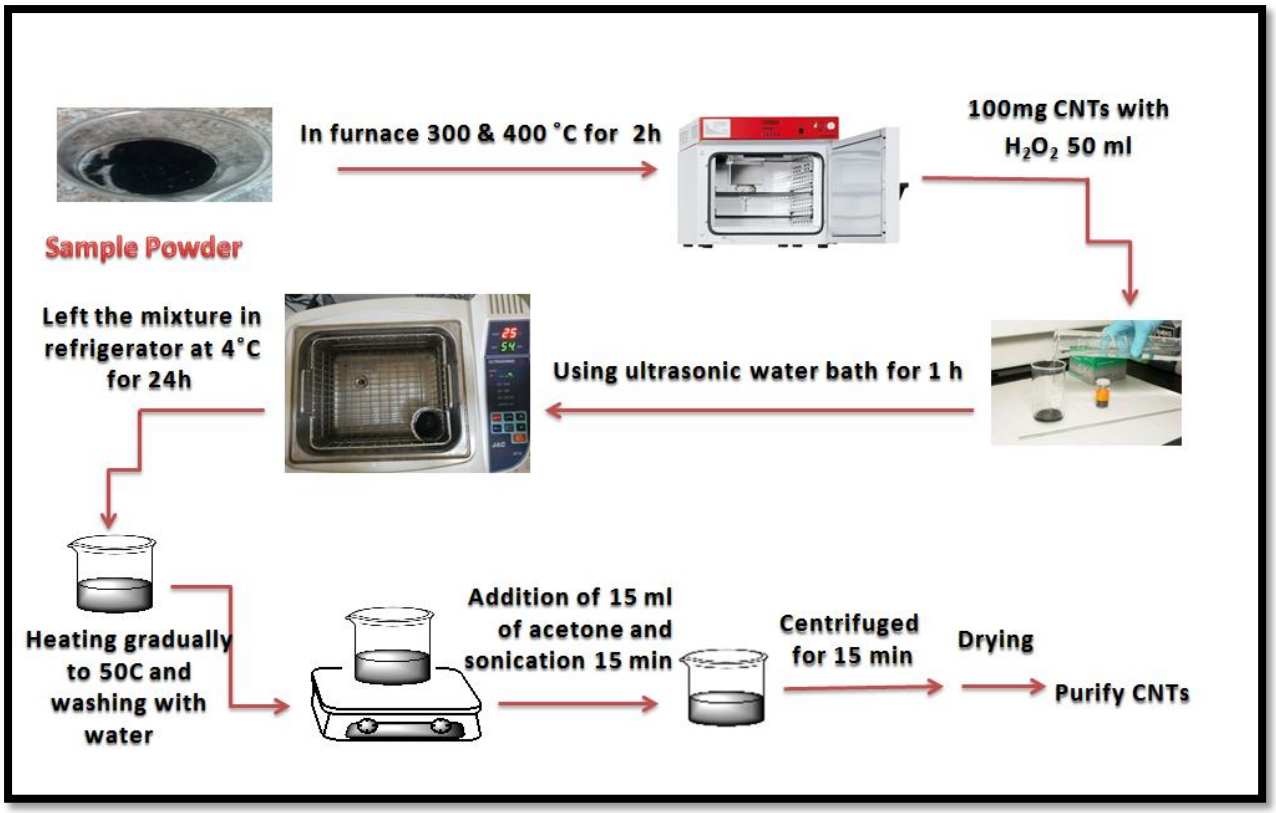

Figure (2.3): Schematic diagram of the steps used in synthesized CNTs purification .

2.6. Functionalization of the synthesized CNTs

Functionalization of CNTs is an important step that can be used to introduce functional groups into the surface and improve its surface properties. The oxidation of the CNTs' surface is critical for the production of the composite. Due to the formation of hydrogen bonds, O-CNTs disperse homogeneously in distilled water as shown in Figure (2.4). FTIR was used to investigate the formed and functioning O-CNTs. In this purpose CNTs (100 mg) were suspended in 75 mL of 30% hydrogen peroxide in a 100 mL round bottom flask with a condenser, and the dispersion was heated to 80 °C at reflux overnight after that added 30 ml of 30% hydrogen peroxide and continuous reflux for other six hours. Following the reflux, the CNTs and hydrogen peroxide suspension were heated to 50 °C until the mixture was dry [256].

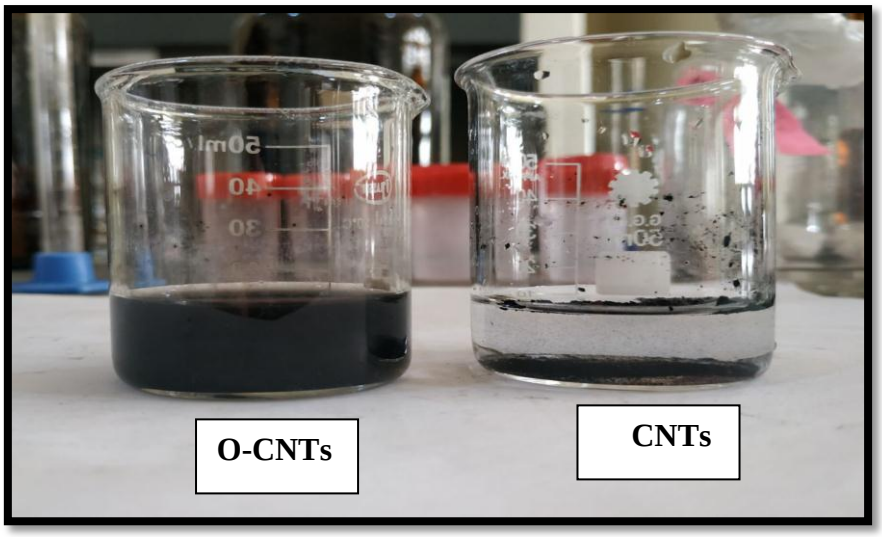

Figure (2.4): Dispersion of CNTs and O-CNTs in water.

2.7. Synthesis of TiO_2/CNTs Composites

A simple evaporation and drying process was used to create different ratios of titanium dioxide nanoparticles (TiO_2) (Anatase , Degussa) /CNTs composite structures. To make TiO_2/CNTs composite, 10 mg CNTs were suspended in 150 mL of deionized distilled water and sonicated for 15 minutes. Titanium dioxide powder was then added to the CNTs suspension while stirring continuously. The suspension containing CNTs and TiO_2 particles was then sonicated for 10 minutes before being heated to 80 °C to accelerate water evaporation. The composite was then dried overnight in an oven at 104 °C [257]. Different composites were created by varying the TiO_2 and CNTs ratios. The mass ratios for TiO_2/CNTs were as follows: 1:0.010, 1:0.025 and 1:0.050 .

2.8. Fabrication of Dye Sensitized Solar Cells (DSSCs)

The prepared photoanodes and counter electrodes were assembled into a sandwich DSSCs configuration, with an electrolyte drop filling the internal space. Using a Keithly 2400 source meter and a 36.83 $mW.cm^{-2}$ intensity of light. The photovoltaic performances of the prepared DSSCs, were estimated including the open-circuit voltage (Voc), short-circuit current density (Jsc), fill factor (FF), and power conversion efficiency (η).

2.8.1. Extraction of the Natural Dyes

Pomegranate fruit seeds were collected and washed with deionized water, squeezed, and then filtered through laboratory filter papers to remove the solids. The filtrate was centrifuged for 15 minute with a centrifuge . Then the deposit was discarded and the filtrate was taken [258]. It is then kept in the dark in the refrigerator until used at 4 °C. The pH of the anthocyanin pigment extracted from the pomegranate was measured using a pH meter, and it was found that it had a pH=3 . When measuring the concentration of the dye in the extract from pomegranate seeds using a device (UV-vis spectrophotometer) as in the Figure (2.5), it was found that the red anthocyanin dye reached its maximum absorbance at 1.131 and wavelength at 511 nm.

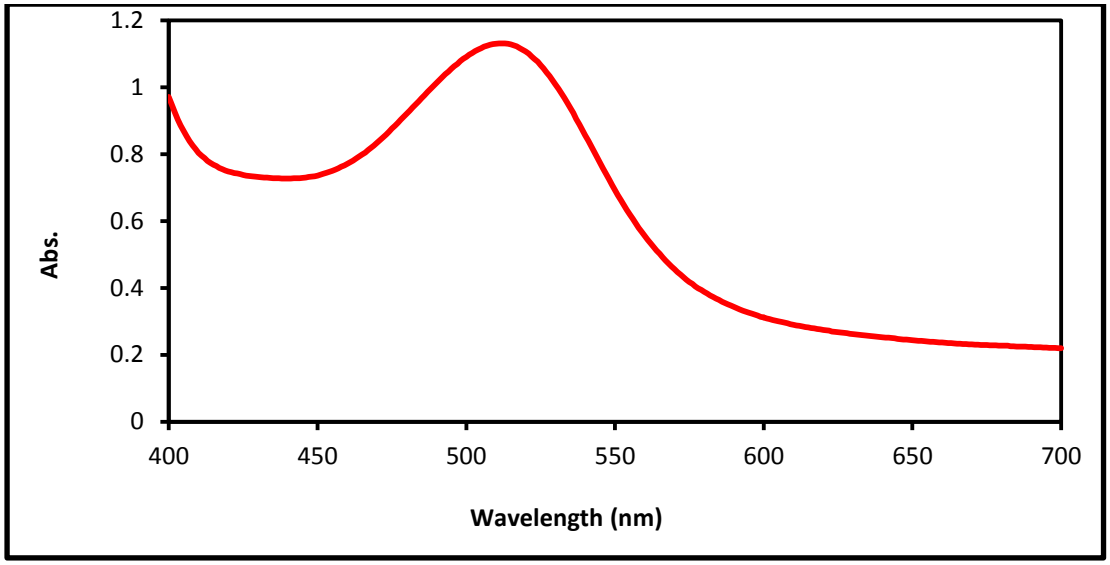

Figure (2.5): Absorption of the extracted red anthocyanin dye at different wavelengths using a device UV-vis spectrophotometer .

Figure (2.6): Preparation of Pomegranate extract and immerges working electrode in Pomegranate solution.

2.8.2. Fabrication of the Working Electrodes (WE)

The FTO glass slides were thoroughly cleaned with isopropanol for 5 minutes, followed by acetone for another 5 minutes. Finally, all cleaned substrates are DIW washed and dried with stream of hot air. To prepare DSSCs, various photoanode materials were used as electrodes, including (TiO_2 anatase & degussa) and its different composites with CNTs. Each time FTO substrates were coated with the prepared paste from its photoanode materials, 0.2 gm of each, 0.4 mL (0.1 M) HNO_3 and one drop of Triton X-100 ($C_{34}H_{62}O_{11}$, M.Wt.646.87). The prepared paste is applied to FTO-glass substrates with using the glass motor to brush the material on the glass and give it a very thin and symmetrical thickness as shown in Figure (2.7) , and the sample is dried for 10 minutes at 80 ^{o}C. Finally, the prepared samples were annealed for 2 hours at 450 ^{o}C before being immersed in a pomegranate dye solution (see Figure (2-6)) for 24 hours in the dark to prevent dye photo degradation. To remove non-adsorbed dye molecules, the surface of photoanode materials was washed with ethanol [259].

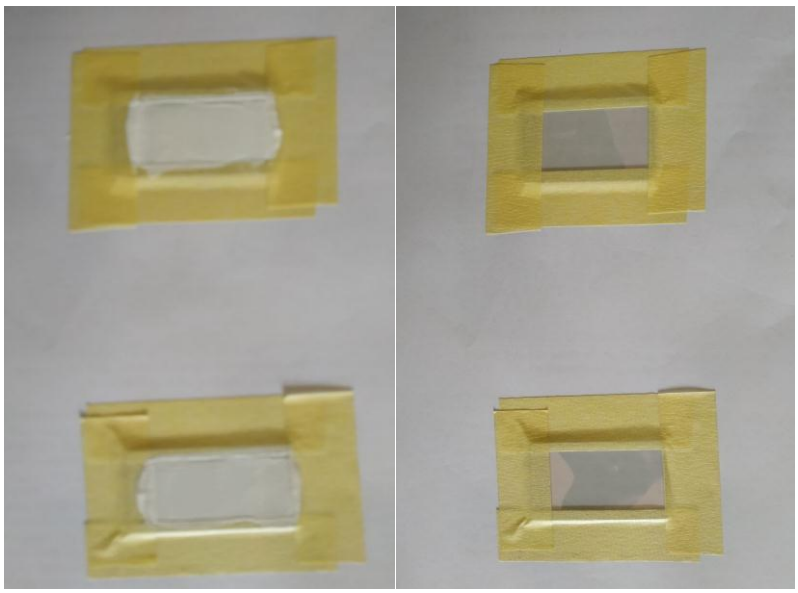

Figure (2.7): FTO glasses fixed with medical tape .

2.8.3. Preparation of the Counter Electrode (CE)

The FTO glass slides were thoroughly cleaned with isopropanol for 5 minutes, followed by acetone for another 5 minutes. Finally, all cleaned substrates are DIW washed and dried at hot air. To prepare the solar cell, three types of cathode electrodes were used, the platinum electrode being the most expensive. To make the Pt CE, the hexachloro platinic acid H_2PtCl_6 was dropped onto the surface of the FTO glass and waiting for it to dry and sintered at 450 °C in a burning furnace for 30 minutes [260]. CNTs CE was made by kneading 0.1 gm of prepared CNTs powder in a mortar with 0.5 mL deionized distil water (DIW) and a drop of Triton X-100 aqueous solution. The CNTs paste is applied to cleaned FTO-glass with a doctor blade or using the glass motor and allowed to dry in the air [261]. Finally, the graphite electrode is prepared by using a candle flame on a clean FTO-glass surface, as shown in Figure (2.8).

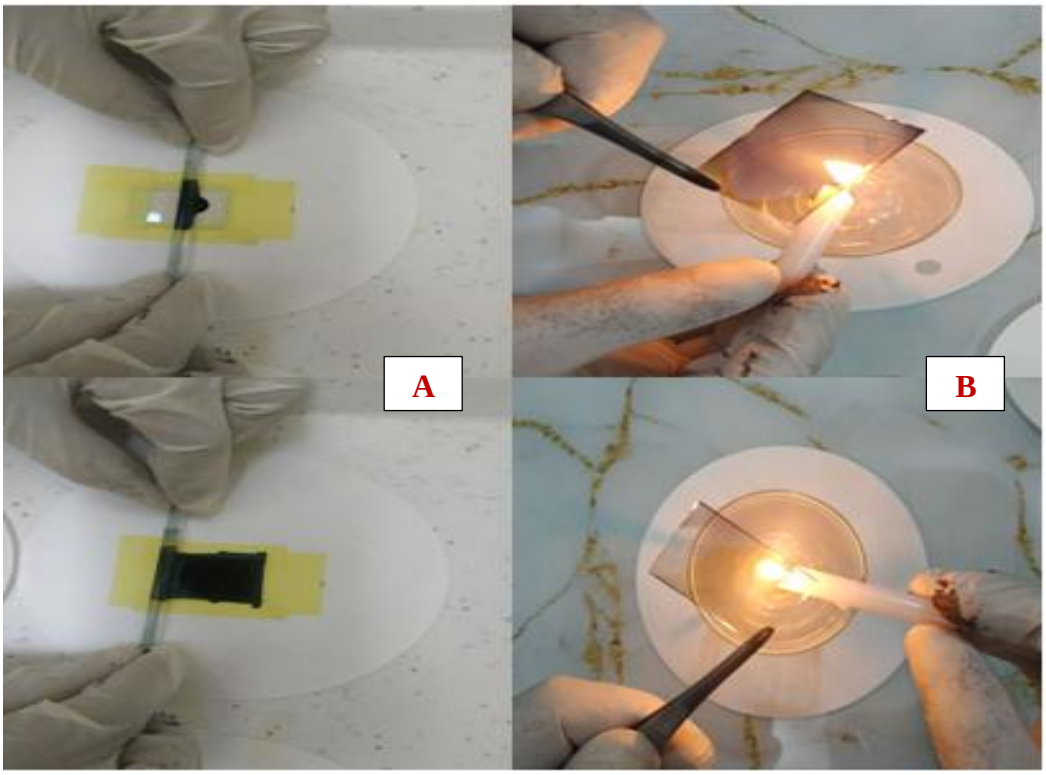

Figure (2.8): FTO glasses with (A)CNT and (B) graphite counter electrode .

2.8.4 Preparation of the Redox Electrolyte

Between two prepared electrodes, a drop of (0.1M) iodine solution is added. To prepare a (0.1 M) iodine solution, dissolve 10 g of potassium iodide (KI) in 25 mL of DIW and add 3.175 g of iodine (I_2). Then shake the flask until the iodine is completely dissolved and the solution is kept in an opaque bottle [262]. The counter electrode is then placed on the working electrode and the solution is kept in an opaque bottle under the condition that the solution does not leak out of the specified area in cell .The find form of DSSC and its connection with Avometer is shown in Figure (2.9).

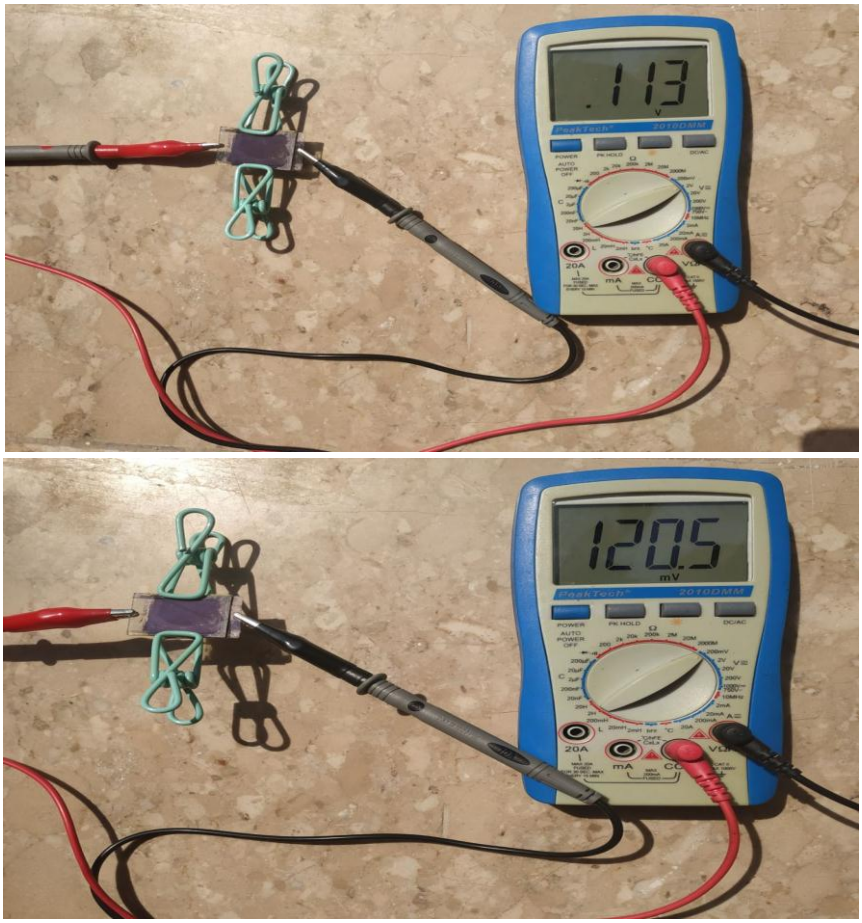

Figure (2.9): The final form of DSSC and voltage generated by the solar cell under sunlight .

a3. Results and Discussion

3.1 Characterization of the synthesized CNTs

The synthesized CNTs in this work were characterized using different spectroscopic and analytical techniques . The used techniques are X-rays diffraction (XRD), Raman spectroscopy, scanning electron microscopy (SEM), energy dispersive X-rays spectroscopy (EDX), transmission electron microscopy (TEM) and thermal gravimetric analysis (TGA).

3.1.1. X-rays diffraction of synthesized CNTs (XRD)

XRD patterns were used to investigate the crystalline nature and quality of carbon nanotubes derived from carbon source materials. Figures (3.1) and (3.2) depict XRD patterns for the synthesized and standard CNTs . From these patterns the peak at (26.0°) for synthesized CNTs and the peak at (25.92º) for standard CNTs (MWCNTs, Sigma - Aldrich) are a typical graphitic peak caused by the presence of carbon atoms in the tubular structure in the samples, corresponding to the (002) reflection. The broad weak peaks around (43.5°) and (53.92º) for synthesized CNTs and the broad weak peaks around (43.46º) and (53.42º) for standard CNTs are attributed to the nanotube structure's (101) and (004) planes respectively [263-265]. The obtained results are summarized in Table (3.1), which shows the angle of diffraction 2θ, d-spacing and the intensities of the diffraction peaks for the synthesized and standard CNTs. These results of XRD patterns for the synthesized CNTs indicate that they are of the MWCNT type due to the convergence of the results and the features of standard MWCNTs, with very slight deviations in the positions of the peaks, possibly due to the difference in the method and conditions of preparation.

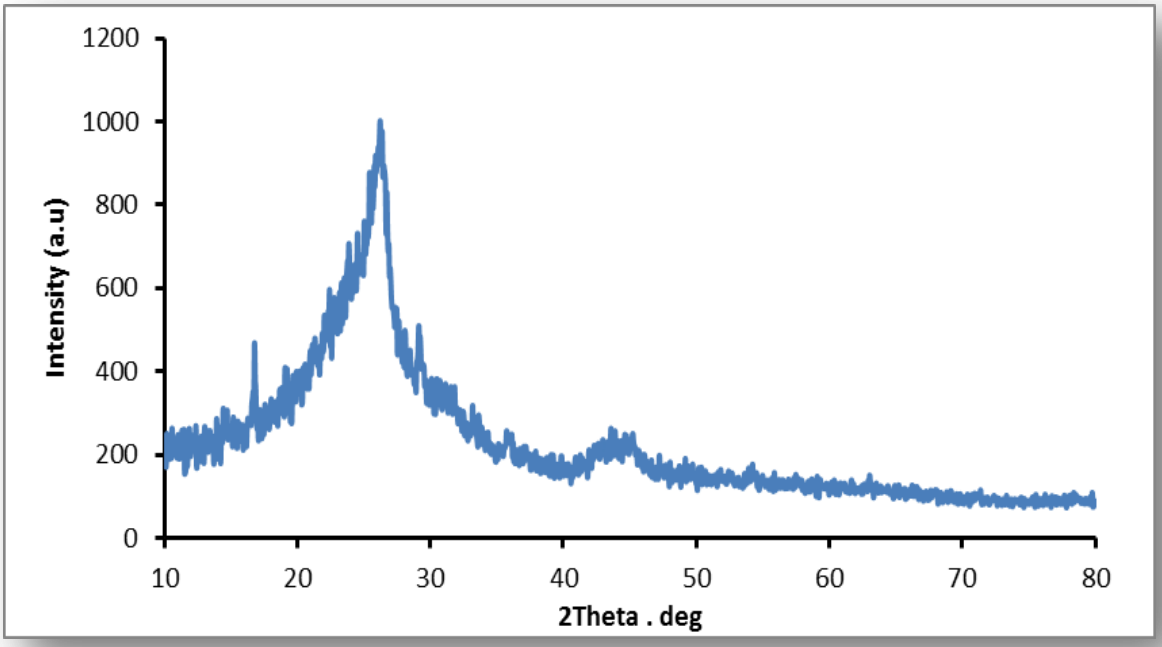

Figure (3.1): XRD pattern of the synthesized CNTs using FFD method.

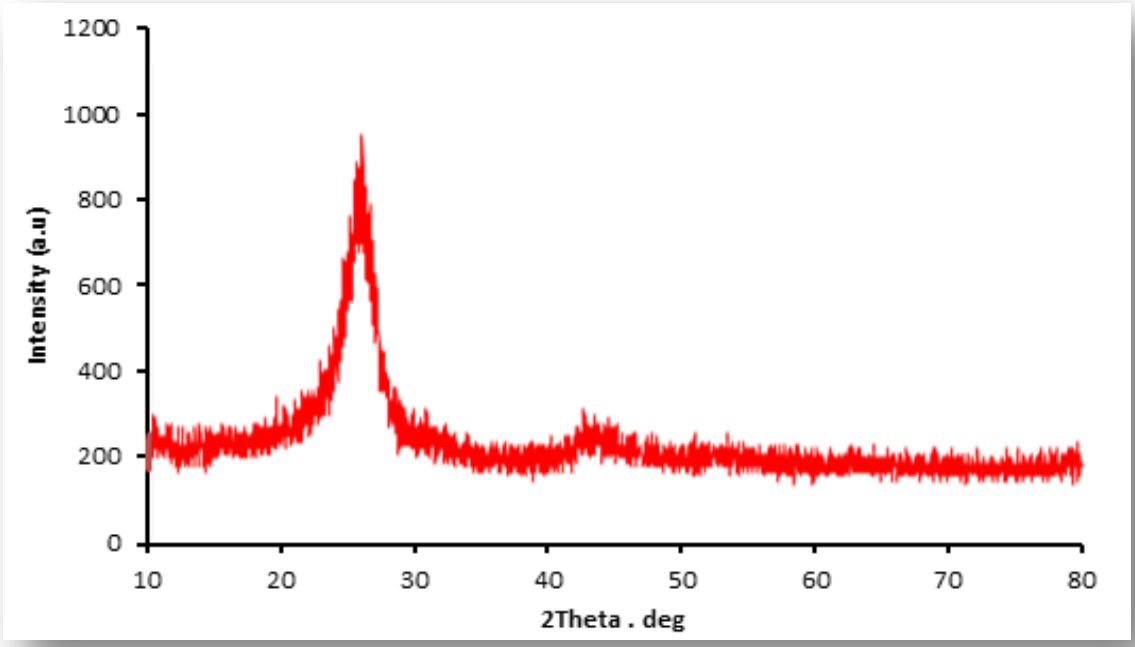

Figure (3.2): XRD pattern of the standard CNTs.

Table (3.1): Comparison of the XRD patterns of the synthesized and standard CNTs.

Sample	2θ. deg	d(A°)	Intensity
Synthesized CNTs	16.775	1.78857	468
	25.875	4.246306	918.79
	26.000	2.154889	1000
	43.575	7.61457	262
	53.925	1.593121	155
Standard CNTs (MWCNTs,Sigma, Aldrich)	25.920	4.015198	990
	43.460	5.550363	270
	53.420	1.540032	165
	53.140	1.553834	160

3.1.2. Raman Spectroscopy

Figures (3.3) and (3.4) show the Raman spectra of the synthesized and standard CNTs. The main peaks in these spectra are in the D and G bands: at 1321 and 1550.7 cm^{-1}; respectively for the synthesized CNTs and at 1354.25 cm^{-1} and 1551.39 cm^{-1} respectively for the standard CNTs. The D band is associated with disordered carbon atoms of CNTs that are sp^3 hybridized, whereas the G band is associated with carbon atoms that are sp^2 hybridized [266]. The second-order harmonic (the G^- band) is

clearly visible at 2661.43 cm^{-1} for synthesized CNTs but equal to 2659 cm^{-1} for standard CNTs , whereas other distinguishable features of MWCNTs, such as the G+D band at 2930 cm^{-1}, are not visible, indicating a very weak band [267,268]. The ID/IG ratio is commonly used to evaluate the structures of carbon nanotube surfaces, which is the most important phenomenon of CNTs with varying amounts of defects. The ID/IG ratio of the synthesized CNTs is relatively high at (0.65), and it is equal to (1.11) for standard CNTs . The presence of a low density of defects on the tubes' walls accounts for this observation. The higher intensity of the G band compared to the D band is most likely due to the lower number of graphene layers, indicating the borderline between few-walled and multi-walled graphene. The Raman spectrum applies to single-walled and multi-walled carbon nanotubes [266,269-271]. Table (3.2): shows comparisons of Raman analysis for standard and synthesized CNTs.

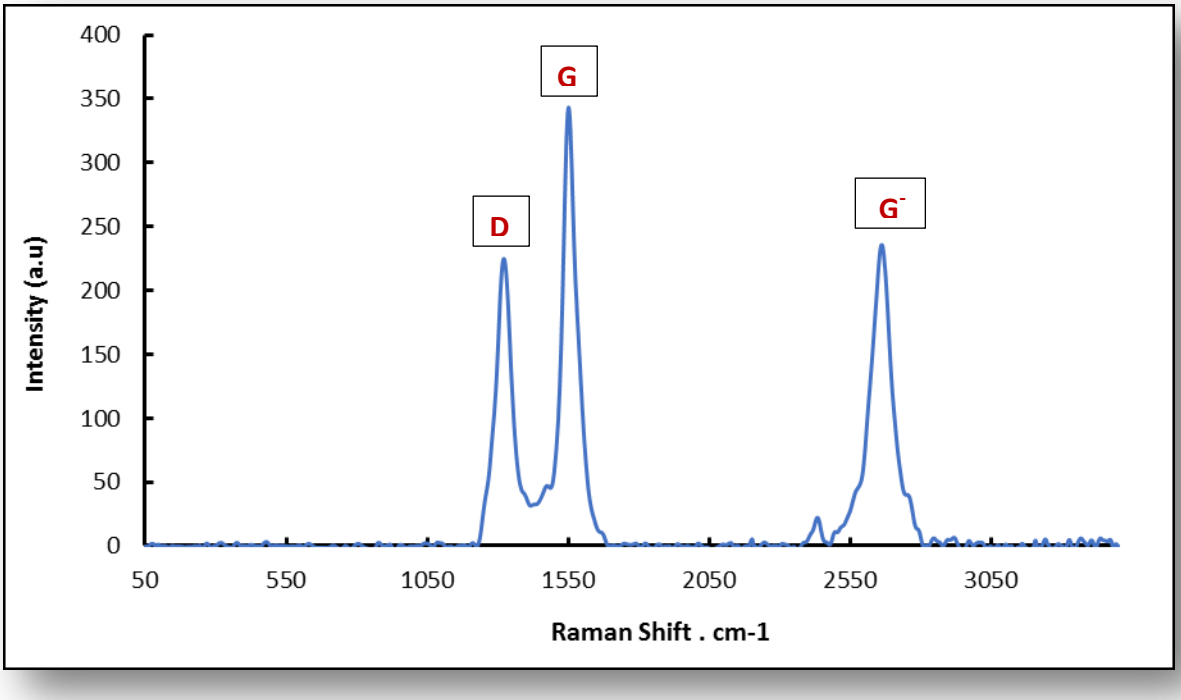

Figure (3.3): Raman spectrum for the synthesized CNTs .

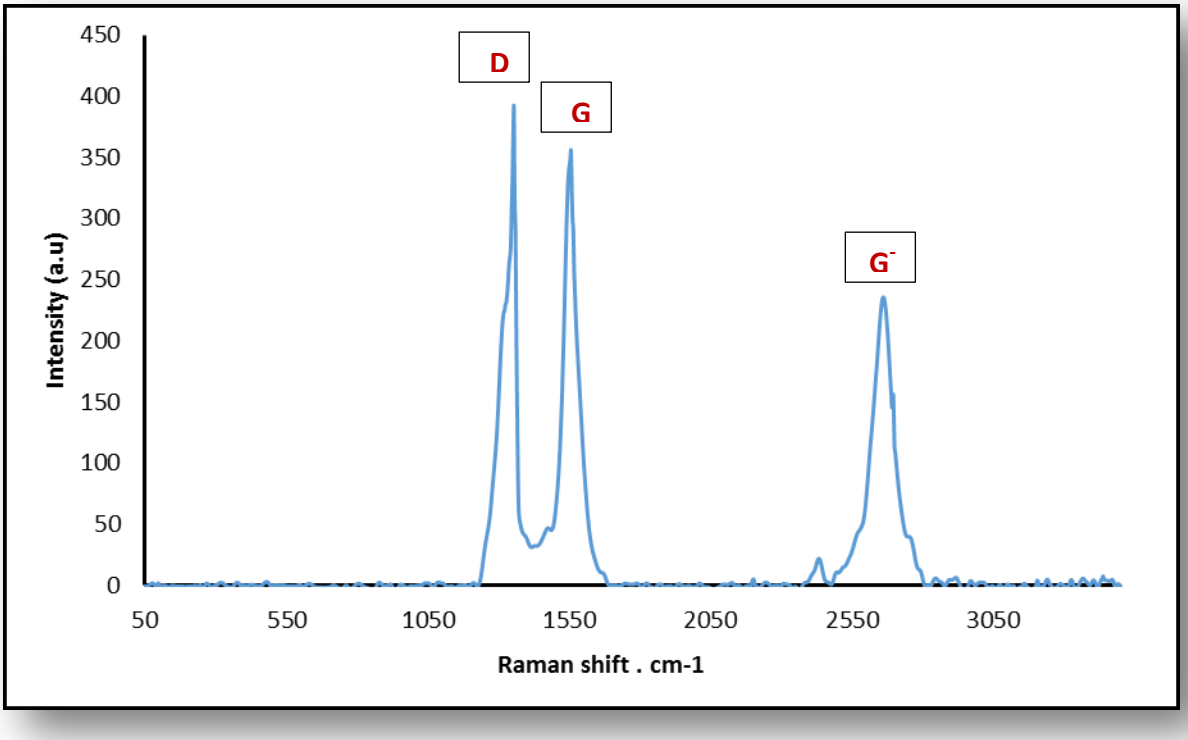

Figure (3.4): Raman spectrum for the standard CNTs .

Table (3.2): comparison of Raman analysis for standard and synthesized CNTs .

CNTs	D-Band		G-Band		I_D/I_G
	Peak cm^{-1}	Intensity	Peak cm^{-1}	Intensity	
Synthesized CNTs	1321.00	225	1550.70	345	0.65
Standard CNTs	1354.25	390	1551.39	349	1.11

3.1.3 Scanning electron microscopy (SEM)

SEM method was used since the diameter of the bundles needed to be accurate. This method primarily provides information on the sample's surface shape as well as its chemical composition. The only variables that can be measured are the size of carbon particles as well as the diameter and length of bundles. It is impossible to find information about the diameter of a single nanotube . The images in Figure (3.5) show the formation of carbon nanotubes clearly and a homogeneous distribution of synthesized CNTs with an average diameter ranging from 31.26 to 78.00 nm, while the average diameter of standard CNTs range from 51.55 nm to 83.82 nm, as shown in Figure (3.6).

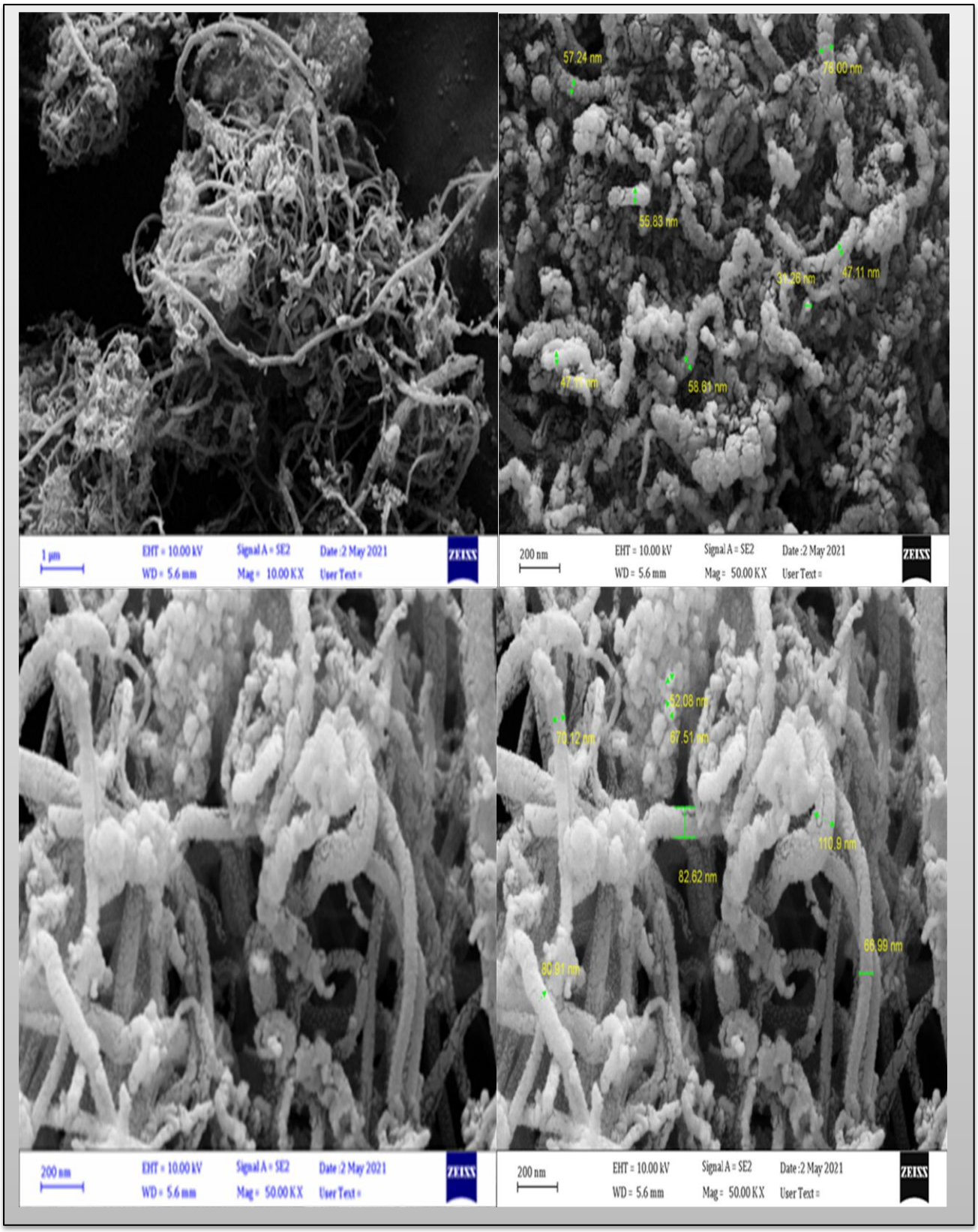

Figure (3.5): SEM images for the synthesized CNTs by FFD.

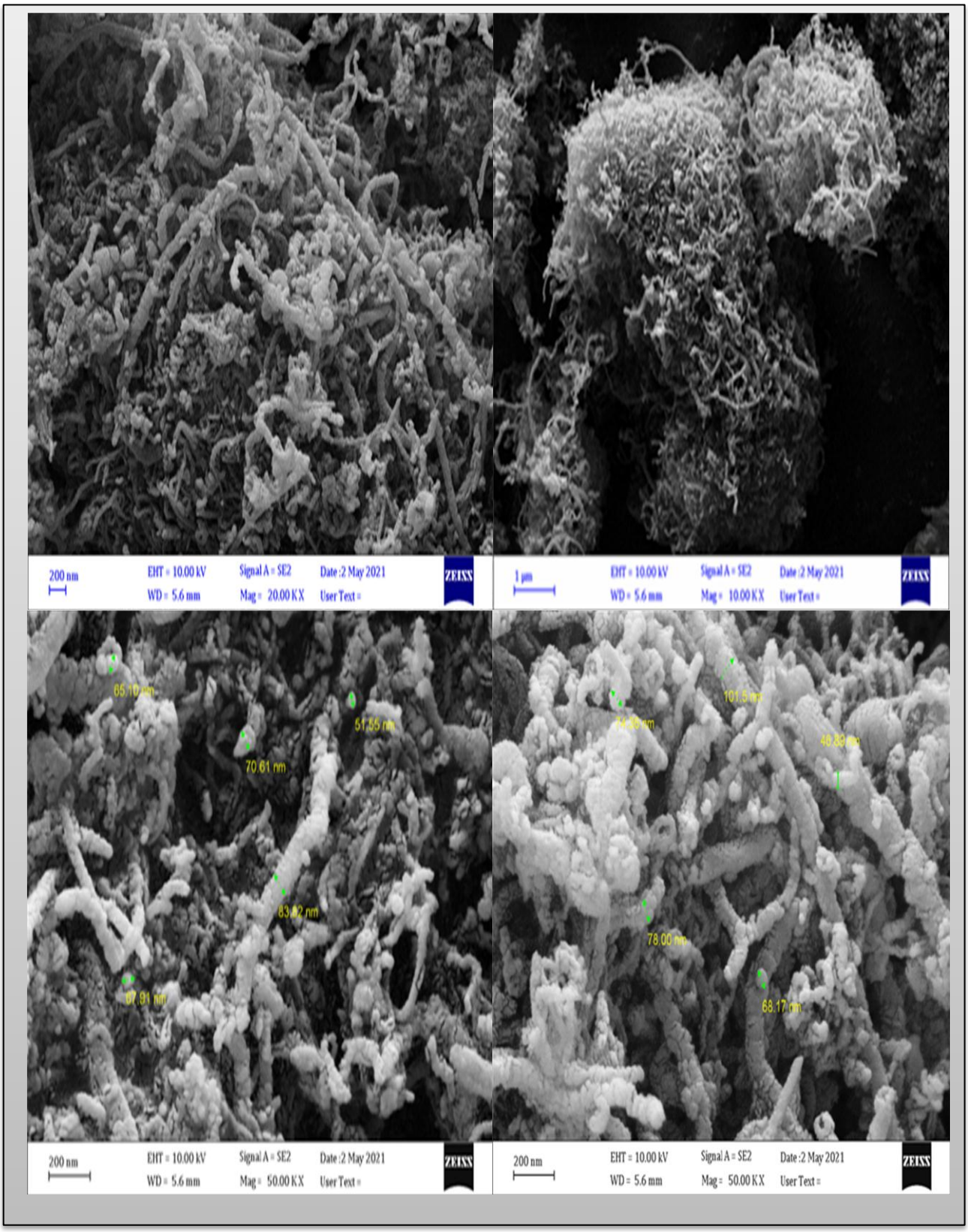

Figure (3.6): SEM images for the standard CNTs (Sigma, Aldrich) .

3.1.4. Energy-dispersive X-rays spectroscopy (EDX)

Using energy-dispersive X-rays spectroscopy (EDX), the elemental composition of the synthesized CNTs was investigated. Figure (3.7) depicts the obtained results , Figure (3.8) shows that of standard CNTs, for comparison. These findings support the oxygen, iron, and carbon content of the synthesized CNTs and starting materials. The quantitative analysis shows the content ratio of the synthesized CNTs, which yielded 89.1% of C, 6.9% of Fe, and 4% of O, while the standard CNTs yielded 93.9% of C, 2.4 % of Fe, and 3.7 % of O. This indicates that dominant element in the synthesized samples is C, as required .Table (3.3) shows the distinctions between synthetic and standard CNTs.

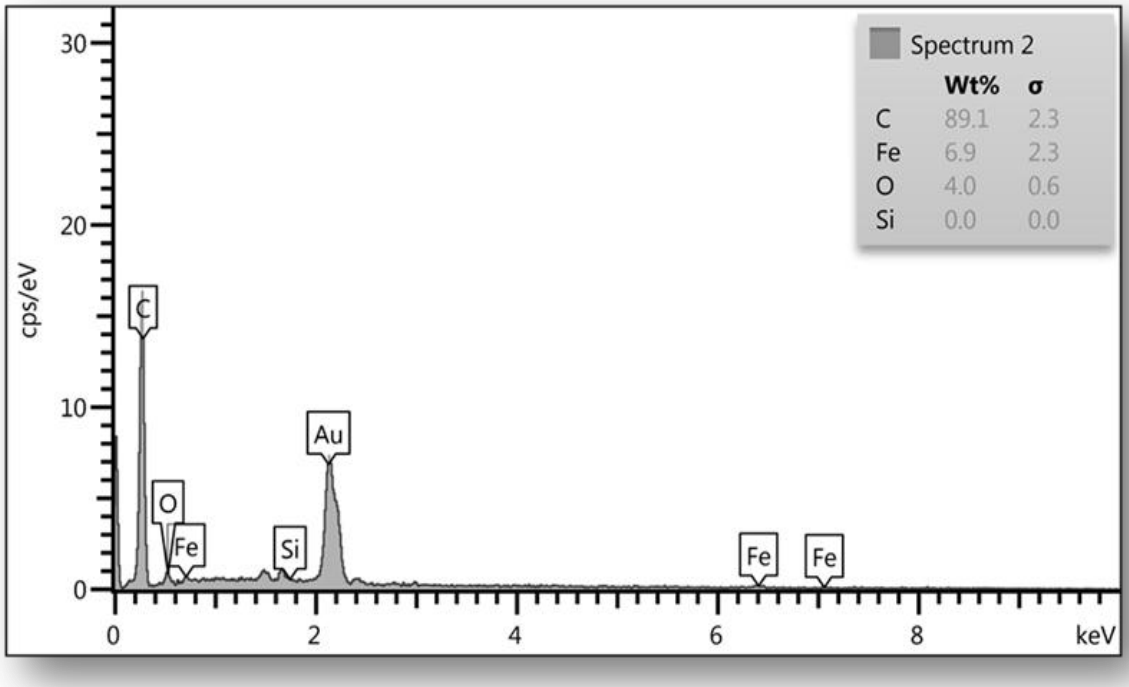

Figure (3.7): EDX analysis for synthesized CNTs.

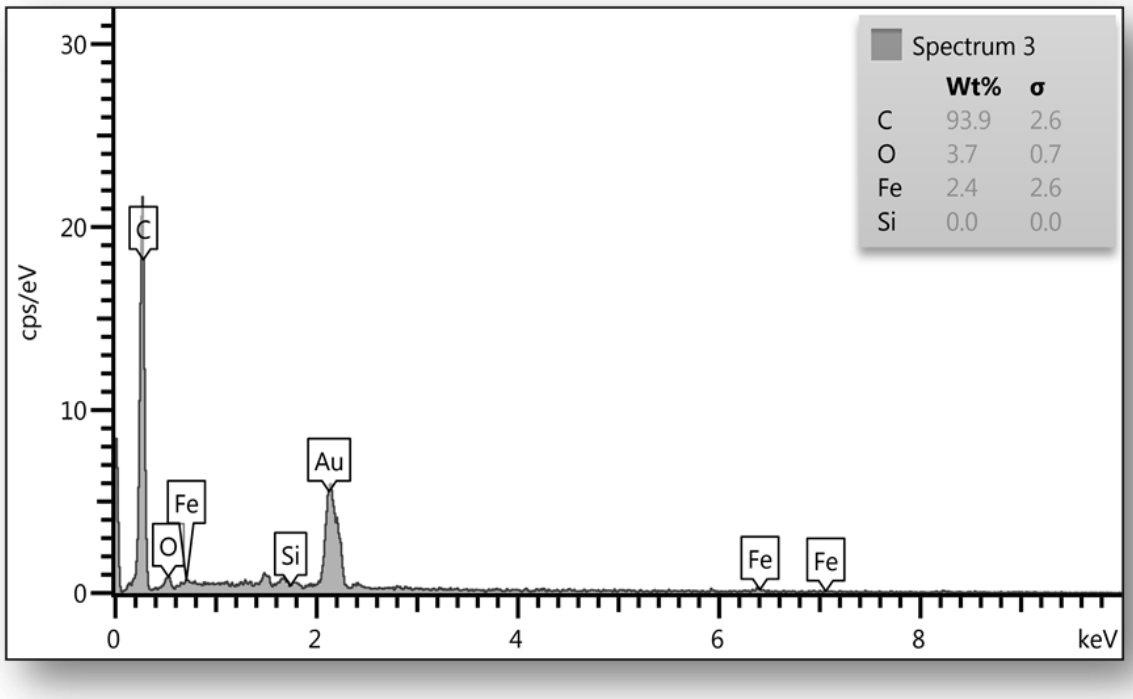

Figure (3.8): EDX analysis for standard CNTs.

Table (3.3): Distinctions in EDX analysis between synthetic and standard CNTs.

EDX analysis of synthesized CNTs			EDX analysis of standard CNTs		
Elemental	**wt%**	**б**	**Elemental**	**wt%**	**б**
C	**89.1**	**2.3**	**C**	**93.9**	**2.6**
Fe	**6.9**	**2.3**	**Fe**	**2.4**	**2.6**
O	**4.0**	**0.6**	**O**	**3.7**	**0.7**
Si	**0.0**	**0.0**	**Si**	**0.0**	**0.0**

3.1.5. Transmission Electron Microscopy (TEM)

TEM was utilized because it can quantify the diameter of nanotubes in a bundle. The diameter of one nanotube and the diameter of the bundle can be determined immediately from the TEM image. Because of its capacity to detect nanotubes at atomic resolution and provide information about surface morphology, this study found that TEM is the ideal approach for thorough analysis of CNTs. The number of nanotubes in the bundle can be determined using the information obtained from TEM. It is widely believed that the diameter of a carbon nanotube may be estimated by measuring the distance between two black lines in a TEM picture associated with carbon nanotubes. In general, the distance between two black lines is smaller than the nanotubes' true diameter. The difference between these two values varies depending on the tube size and alignment with the electron beam, and it can be as much as 30% for sub-nanometer carbon nanotubes. The difference between the two tubes is typically less than 10% for tubes larger than 1.0 nm. The TEM images of the as-grown carbon nanotubes are displayed in Figure (3.9); these samples mostly consist of multi-walled nanotubes with a hollow internal channel bearing at the tip and some few-walled carbon nanotubes. TEM provide a more realistic picture of the synthesized tubular structure. The nanotubes in the TEM image have diameters ranging from 29 nm to 50 nanometers. This indicates that the synthesized CNTs falls within the range of MWCNTs specifications.

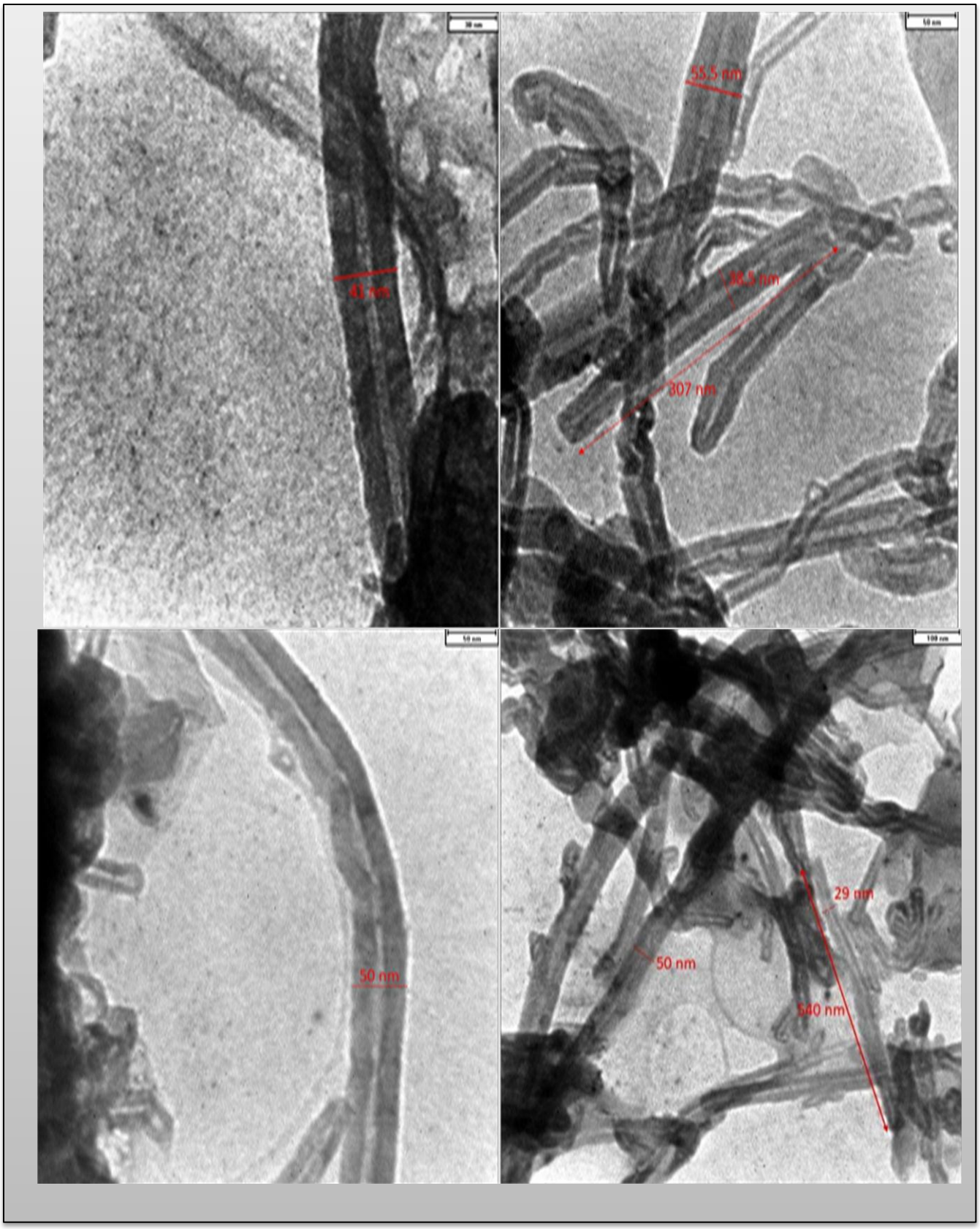

Figure (3.9): TEM images of synthesized CNTs by FDD.

3.1.6 Thermal gravimetric analysis (TGA)

Figure (3.10) indicates the thermal gravimetric analysis (TGA) of the synthesized CNTs, while that of standard CNTs is shown in Figure (3.11), for comparison. The TGA analysis results for the synthesized CNTs after purification show that there are three main regions for losing weight. The first weight loss appears around 100 ºC, representing a loss of around 4%. This can be attributed to the loss of water that may have been adsorbed at the surface of CNTs during purification processes conducted under normal atmospheric conditions. The second weight lose appears around 130-190˚C, referring to a weight loss of around 2%, which can be attributed to the loss of absorbed aromatic molecules that may be present with the liquefied petroleum gas. The third weight loose appears at 200-320˚C, referring to a weight loss percentage of 5% of the sample's weight. This is due to the conversion of amorphous and unconverted carbon to CNTs. The largest loss occurs at 450°C, with a gradual decrease in weight until it reaches approximately 750°C, which is attributed to the degradation of graphene walls of tubular structure. The interference between each ether causes this behavior. These results mostly indicate the formation of carbon nanotubes with high purity level and high quality modulus since the greatest weight loss was induced after a temperature of 450°C.

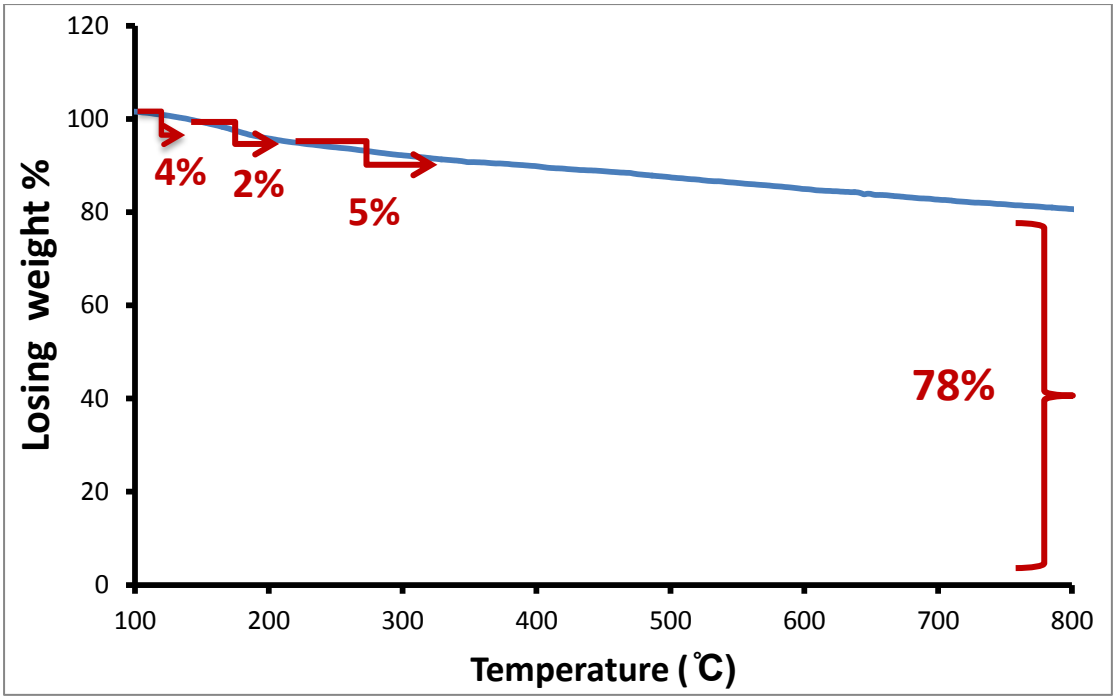

Figure (3.10): Schematic diagram of TGA for synthesized CNTs.

Figure (3.11) shows the TGA of standard CNTs, and the result refers to a small weight loss from (150-170)°C, which is due to the decomposition of residual hydrocarbon impurities that are equal to 5% of the total weight. The dominant weight loss of 85% is due to the decomposition of the CNTs in the temperature range of (233-845)°C .

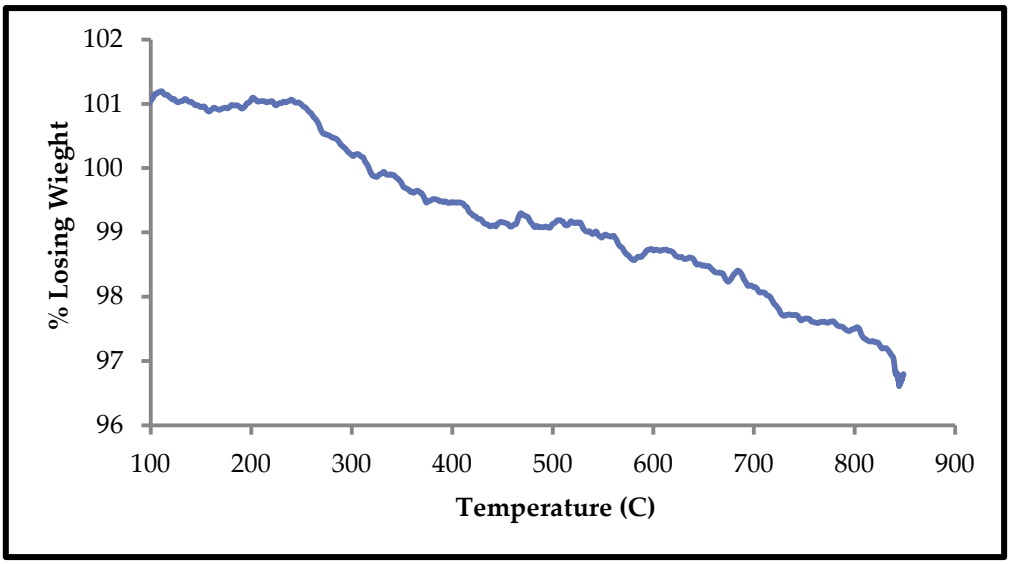

Figure (3.11): Schematic diagram of TGA for standard CNTs.

3.1.7 Functionalization of the synthesized CNTs.

The chemical oxidation of CNTs is carried out using H_2O_2 in order to obtain the hydrophilic surface structure of oxygen within a certain surface group. This oxidation process with H_2O_2 introduces several functional groups, such as -OH (Hydroxyl), -COOH (carboxyl), and others, on the synthesized CNTs' surface [125]. These surface groups are useful during the interaction and chemical bonding between CNTs and TiO_2.

FT-IR was conducted on synthesized CNTs before and after functionalization in the range 400 to 4000 cm^{-1}, as shown in Figure (3.12). Figure (3.12 a) shows the FTIR spectrum of the synthesized CNTs before functionalization. It appears that no effective group are contained on the surface of the synthesized carbon nanotubes. However, after functionalization, CNTs show a broad peak at 3450 cm^{-1}, which refers to the O-H stretch of the hydroxyl group, as shown in Figure (3.12 b). This can be ascribed to the oscillation of carboxyl groups. The carboxylic stretching frequency in the functionalization of synthesized CNTs occurred at 1720 cm^{-1}, indicating that carboxylic groups are formed due

to the oxidation of some carbon atoms on the surfaces of the synthesized CNTs by H_2O_2. The peak at 2920 cm^{-1}, on the other hand, can be linked to asymmetric and symmetric C–H stretching. The stretching of the carbon nanotube backbone can be assigned to the peak at 1639 cm^{-1} [272]. The signal at 1163 cm^{-1} can be related to C–O stretching in the same functionalities, but the peak for the acid functionalized synthetic CNTs was found at 1404 cm^{-1}, which is related to the carboxylic acid group's O-H bending deformation mode. The peak at 2364 cm^{-1} can be associated with the O−H stretch from strongly hydrogen-bonded −COOH [273]. The peak at 1566.2 cm^{-1} is related to the carboxylate anion stretch model [274]. Functionalization process by acidic oxidation of carbon surface can offer not only a more hydrophilic surface but also a larger number of oxygen containing function groups, which increase the ion-exchange capability of carbon material.

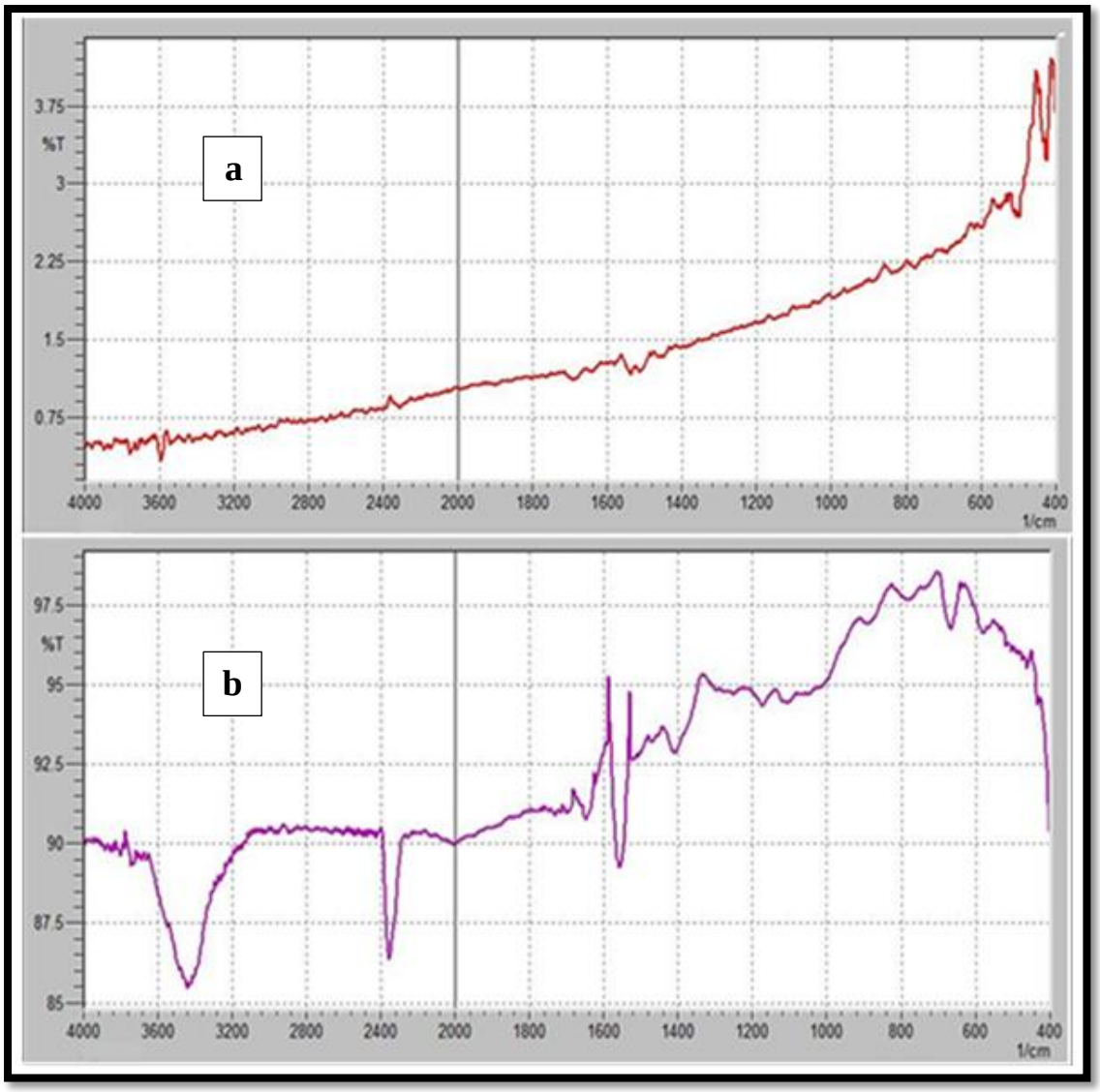

Figure (3.12): FTIR spectrum for the as-synthesized CNTs (a) before functionalization and (b) after functionalization.

3.2. Characterizing of the Synthesized Composite TiO_2/CNTs

3.2.1. X-rays patterns of synthesized TiO_2/ CNTs composites

Figures (3.13) to (3.16) show the XRD patterns of TiO_2 (anatase) and TiO_2 (anatase)/CNTs composites prepared with various weight ratios of synthesized CNTs. The TiO_2 (anatase)/CNTs composite catalysts have XRD patterns that are extremely close to that of TiO_2. Figure (3.13) indicates the XRD pattern of TiO_2 anatase, with several characteristic peaks at 2θ = 25.4 (101), 37.82 (004), 48.07 (200), 53.9 (105), 55.1 (211), 62.7 (204), 68.5 (116), 69.5 (220), and 75 (301). If the characteristic peaks of TiO_2 (anatase) in Figure (3-13) are compared with those of TiO_2 (anatase)/CNTs composites (Figure (3.14) to (3.16)), it is easily understood that for composite ratios of 0.01 to 0.05 of CNTs, the crystallite diameters of the composite catalysts decrease steadily as the ratios of CNTs increase. With the presence of CNTs in TiO_2, these peaks will be less strong and wider [275,276]. The diffraction peaks of carbon nanotubes were not clearly visible, most likely due to the composites being obscured by the much more powerful peak of the high TiO_2 ratio or the low carbon nanotube loading amount. From the XRD data, the average crystallite size of the synthesized samples was determined using Scherrer's equation [277]:

$$d = k\lambda / \beta \cos\theta \text{ ---------(3.1)}$$

where d is the crystallite size, k is a constant (0.9), λ is the wave-length of X-ray (CuKα), β is the half-peak width in radians and θ is the Bragg's diffraction angle in degrees. Table (3.4) show the values of angles of diffraction 2θ, d-spacing, intensities and average crystalline sizes of the TiO_2 anatase and its composites with synthesized CNTs.

Table (3.4): Values of angles of diffraction 2θ ,d-spacing , intensities and average crystalline sizes of the TiO_2 anatase and its composites with synthesized CNTs.

Sample	2θ (deg.)	d(A°)	Intensity (a.u)	Avarege crystalline size (nm)
TiO_2 anatase	25.475	9.043113	1200	21.35102
	37.075	8.242365	108.041	
	37.925	13.6641	251.373	
	48.075	1.73221	319.8224	
	53.825	1.574245	152.7007	
	53.975	1.604245	178.1542	
	54.025	1.616544	186.3024	
	62.275	5.6032	76.148	
	62.775	3.763472	157.6396	
	67.975	2.853711	35.9683	
	69.125	1.655518	66.4547	
	74.925	6.56968	85.3974	
	75.475	8.30052	95.133	
	75.025	11.308	62.5784	
TiO_2 anatase + 0.01 CNTs	25.475	9.08697	885.3341	37.04139
	37.925	11.2348	215.2785	
	48.275	4.731077	313.4544	
	53.970	1.879964	151.385	
	54.175	1.925155	164.667	
	62.670	3.31944	116.7882	
	68.970	3.10784	56.964	
	70.325	2.85939	55.28	
	75.025	5.52064	71.0422	
	75.125	8.34833	70.0868	

TiO_2 anatase + 0.025 CNTs	25.525	7.952767	1004.985	35.64455
	37.975	9.534813	254.9177	
	48.175	6.594479	283.2754	
	48.275	5.496468	286.821	
	54.075	1.900411	182.457	
	54.425	2.00934	130.9912	
	62.575	4.8582	124.2152	
	68.725	7.996894	60.8563	
	69.125	9.145161	49.4718	
	74.925	6.63023	68.1802	
TiO_2 anatase + 0.05 CNTs	25.475	9.08697	974.6275	32.60126
	37.925	11.2348	208.833	
	48.125	2.00253	265.0596	
	48.075	1.98334	239.6097	
	53.925	1.871224	169.0683	
	54.075	1.900411	165.87	
	62.625	8.72269	124.9321	
	68.675	3.366992	52.7263	
	69.375	7.61827	50.7879	
	74.975	4.74842	75.244	

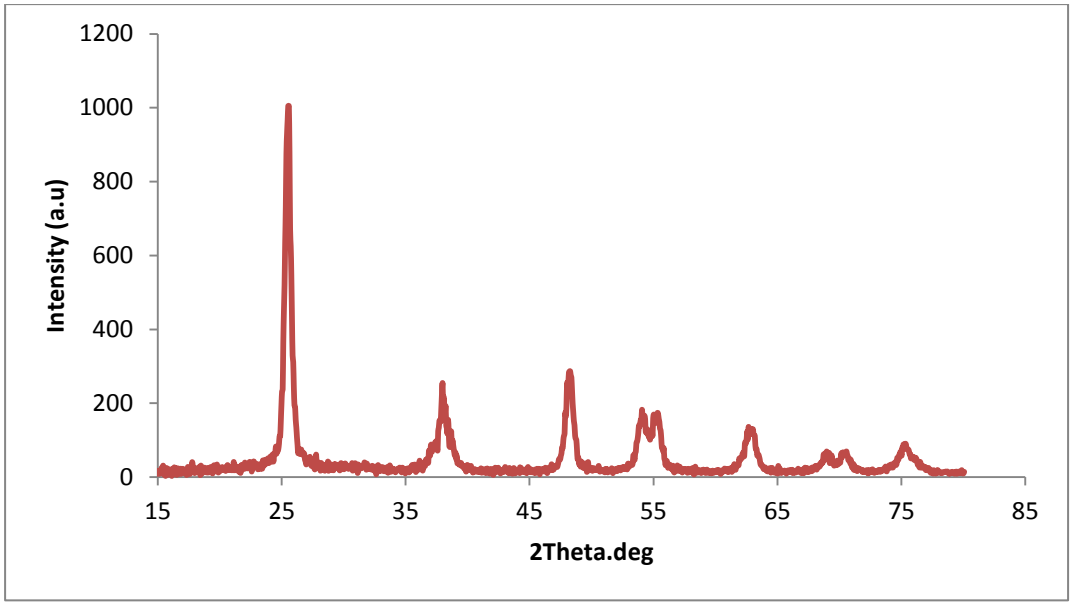

Figure (3.13): XRD pattern of TiO_2 anatase.

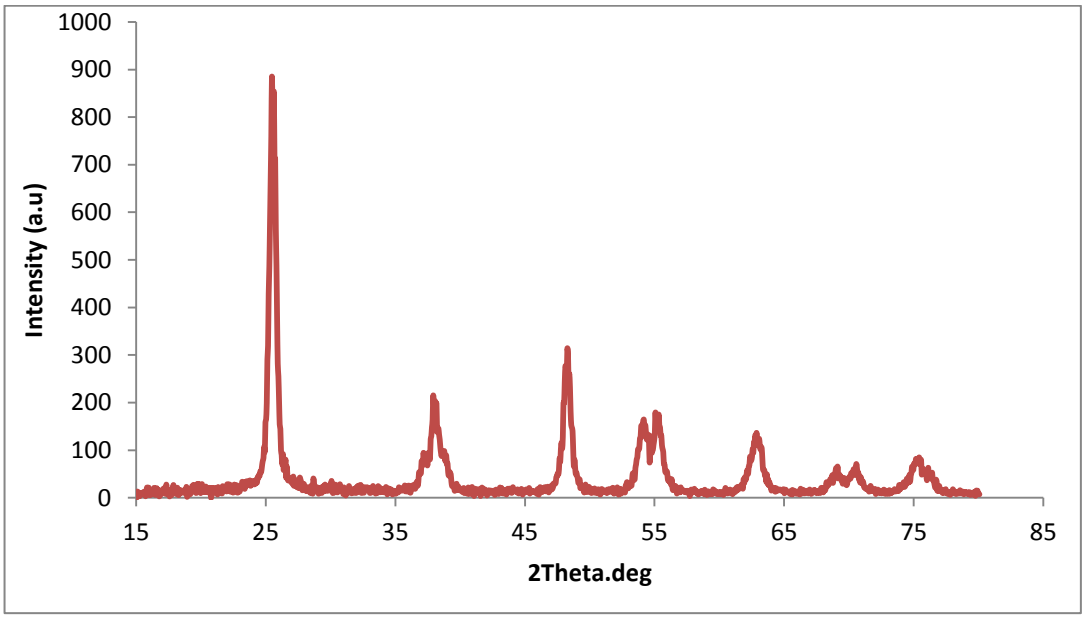

Figure (3.14): XRD pattern of TiO_2 anatase/ 0.01 CNTs composite.

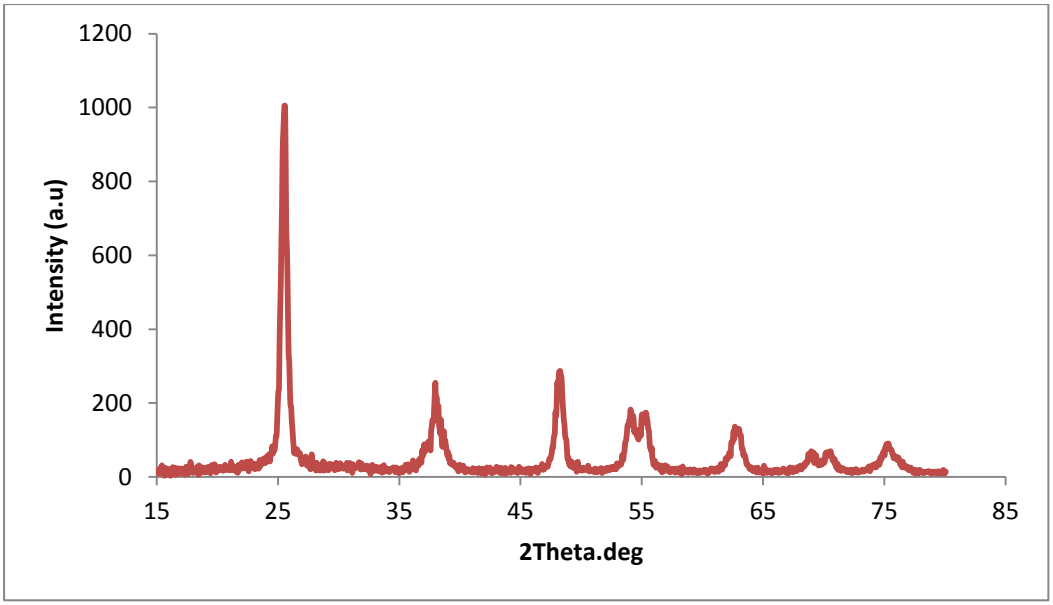

Figure (3.15): XRD pattern of TiO_2 anatase /0.025 CNTs composite.

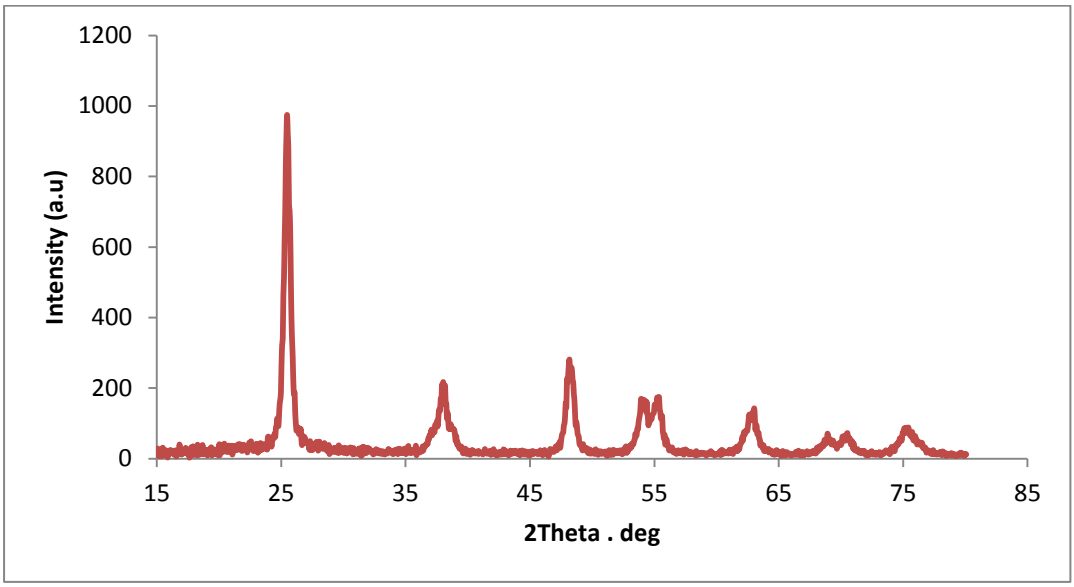

Figure (3.16): XRD pattern of TiO_2 anatase/0.05 CNTs composite.

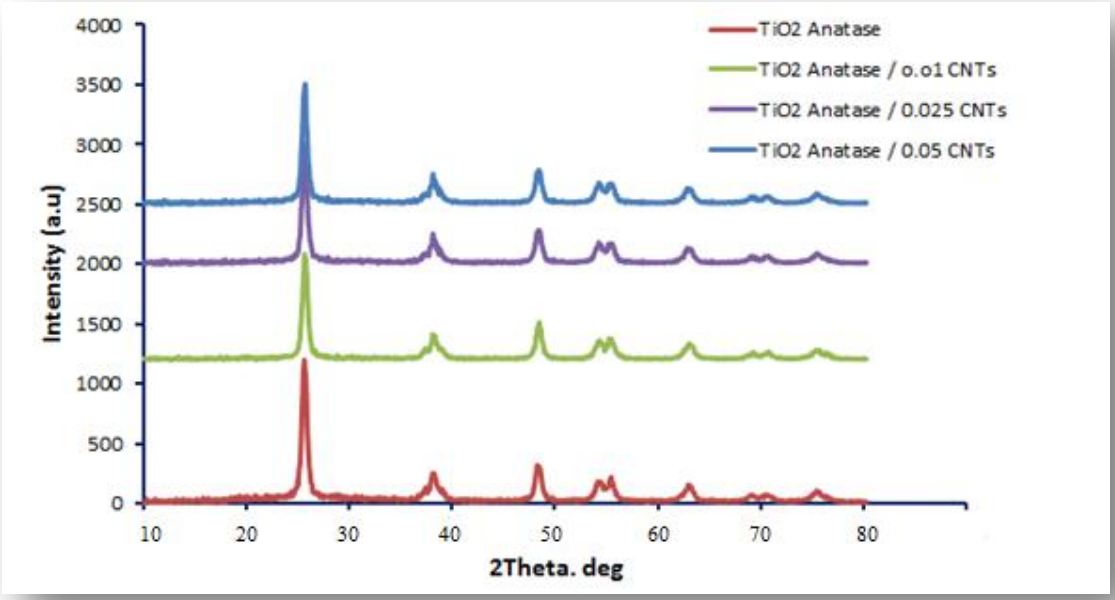

Figure (3.17): XRD pattern of TiO_2 anatase /CNTs composites.

Figures (3.18) to (3.21) show the XRD patterns of TiO_2 (degussa) and TiO_2 (degussa)/CNTs composites generated with various weight ratios of synthesized CNTs. The TiO_2 (degussa)/CNT composite catalysts have XRD patterns that are extremely close to that of TiO_2. Figure (3.18) indicates the XRD pattern of TiO_2 degussa, with several characteristic peaks at 2θ=25.5, 27.5, 36.5, 37.97, 40.9, 48, 54, 55.2,62.8, 68.8, 70.17 and 75.05 for A(101), R(110), A(103), A(004), R(111), A(200), A(106), A(211), A(204), A(116), A(220) and A(215) respectively (A: anatase and R: rutile). According to it, both anatase and rutile crystallites are confirmed in TiO_2 degussa structure, but no brukite phase is observed. If the characteristic peaks of TiO_2 (degussa) in Figure (3.18) are compared with those of TiO_2 (degussa)/CNTs composites (Figure (3-19) to (3-21)), it is easily understood that for composite ratios of 0.01 to 0.05 CNTs at the same state in TiO_2 anatase, the crystallite diameters of the composite catalysts decrease steadily as the ratios of CNTs increase. With

the presence of CNTs in TiO_2, these peaks will be less strong and wider [278]. The diffraction peaks of carbon nanotubes were not clearly visible due to the same reasons in TiO_2 anatase. Table (3.5) show the values of angles of diffraction 2θ, d-spacing, intensities and average crystalline sizes of the TiO_2 degussa and its composites with synthesized CNTs.

Table (3.5): Values of angles of diffraction 2θ ,d- spacing , intensities and average crystalline size of the TiO_2 degussa and its composites with synthesized CNTs.

Sample	2θ (deg.)	d(A°)	Intensity (a.u)	Avarege crystalline size (nm)
TiO_2 degussa	**25.525**	**7.952767**	**1041.013**	**41.68045**
	37.975	**9.534813**	**247.1919**	
	48.175	**2.02332**	**302.7762**	
	54.075	**1.900411**	**205.4946**	
	54.275	**1.954692**	**182.7538**	
	62.825	**19.6765**	**163.9566**	
	68.825	**9.145161**	**71.1557**	
	69.125	**10.69378**	**54.6405**	
	75.075	**9.61204**	**90.750**	
	75.175	**11.343**	**94.7695**	
TiO_2 degussa + 0.01 CNTs	**25.525**	**7.952767**	**1103.588**	**48.21712**
	37.925	**11.2348**	**235.9039**	
	48.175	**2.02332**	**348.9624**	
	54.125	**1.912217**	**198.874**	

	54.270	1.93929	183.6722	
	62.825	10.1162	155.1158	
	68.875	9.145161	62.9633	
	70.275	2.95592	73.5098	
	74.975	6.63023	88.7903	
	75.325	9.61204	91.8664	
TiO_2 degussa + 0.025 CNTs	25.525	7.952767	1274.245	44.46
	37.875	11.2348	238.7854	
	48.075	7.341419	315.7089	
	54.075	1.900411	204.5731	
	54.225	1.93929	194.8584	
	62.575	7.67487	145.9932	
	68.675	6.411245	57.9247	
	70.075	3.45659	59.1	
	74.875	5.52064	82.00	
	75.275	11.343	87.8026	
TiO_2 degussa + 0.05 CNTs	25.252	7.952767	970.8537	40.26903
	37.925	11.2348	221.7239	
	48.125	2.00253	281.4974	
	54.175	1.925155	215.2631	
	54.125	1.912217	150.997	
	62.775	10.1162	132.706	
	68.775	9.145161	51.9174	

	69.175	12.89292	65.6747	
	75.075	9.61204	77.6892	
	75.425	9.509354	81.4908	

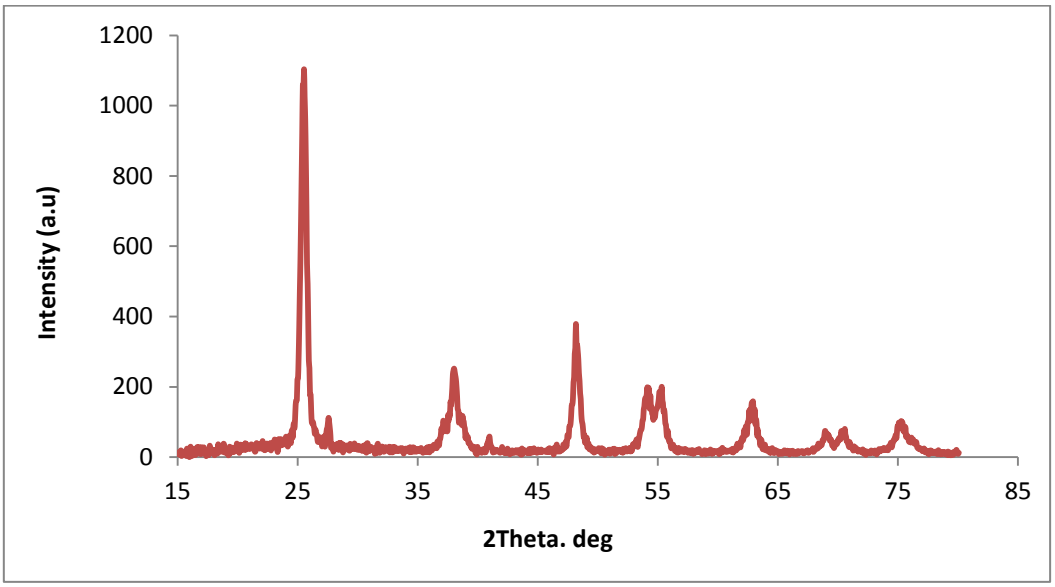

Figure (3.18): XRD pattern of TiO_2 degussa.

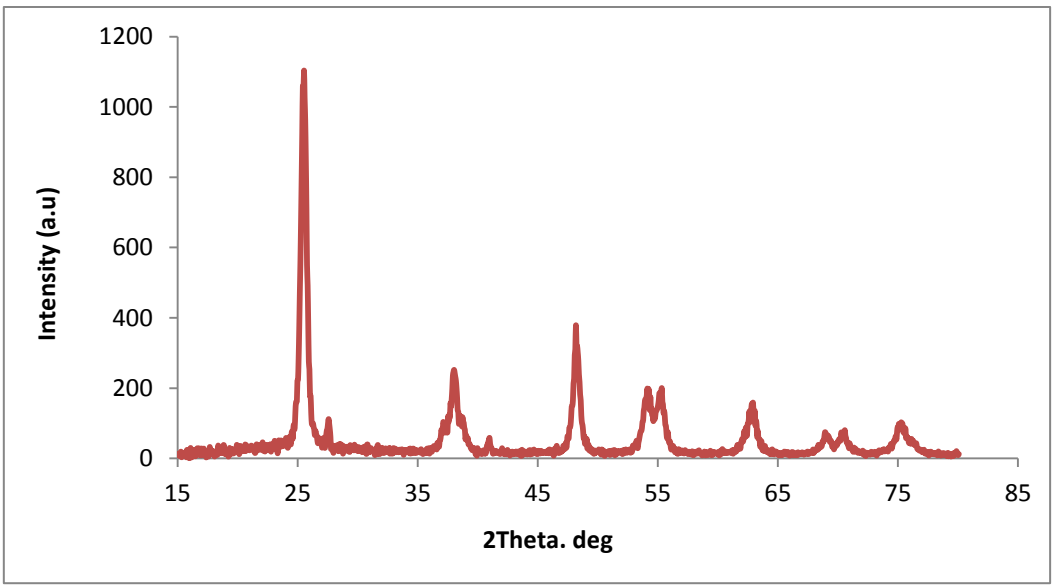

Figure (3.19): XRD pattern of TiO_2 degussa/0.01 CNTs composite.

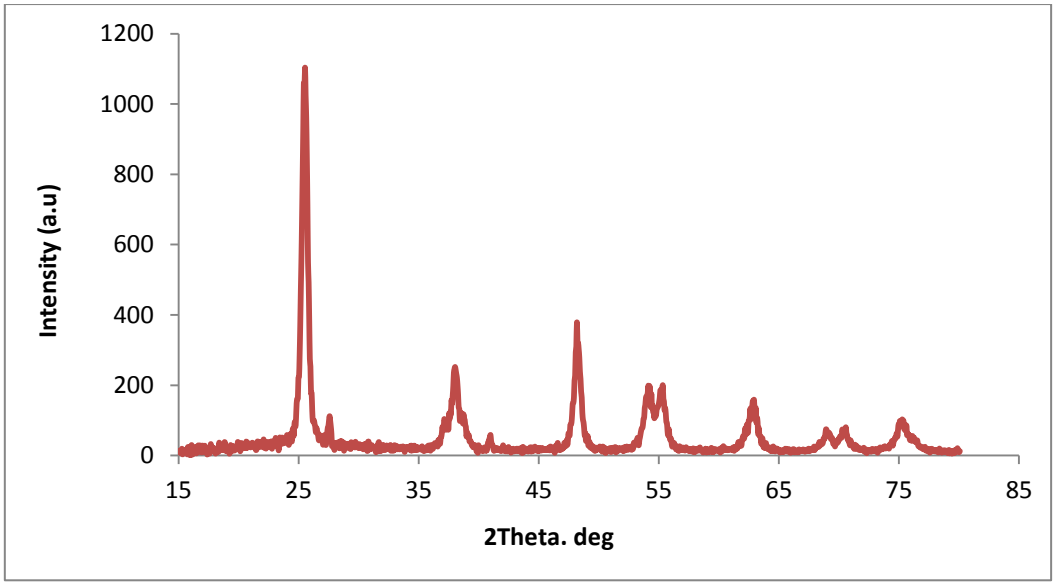

Figure (3.20): XRD pattern of TiO_2 degussa /0.025 CNTs composite.

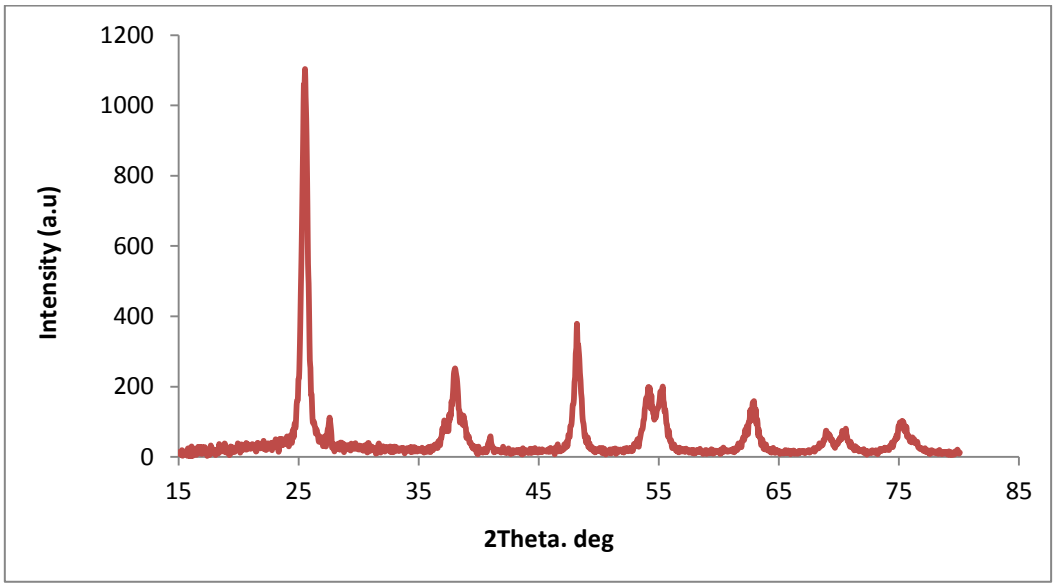

Figure (3.21): XRD pattern of TiO_2 degussa/ 0.05 CNTs composite.

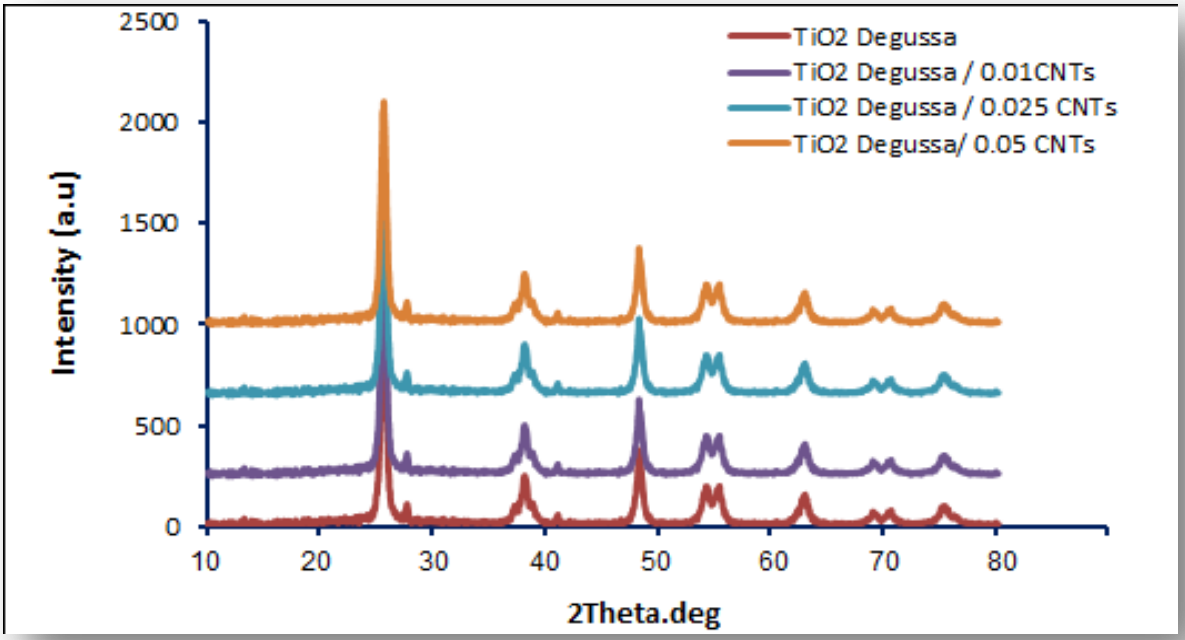

Figure (3.22): XRD pattern of TiO_2 Degussa/ CNTs composites.

3.2.2 Raman Spectroscopy

Raman spectroscopy was also used to distinguish the TiO_2 crystalline phases from the powder mixtures [223].

The pure TiO_2 in the region 100-800 cm^{-1} is visible in the Raman spectra, as shown in Figures (3.23), and (3.27), confirming the presence of TiO_2 (anatase) and (degusa). The TiO_2 anatase spectrum reveals the presence of five distinct Raman lines at 130.9 cm^{-1} (Eg), 160.0 cm^{-1} (Eg), 378.9 cm^{-1} (B1g), 597.8 cm^{-1} (A1g + B1g), and 622.9 cm^{-1} (Eg), which correspond to the Eg, Eg, B1g, A1g + B1g, and Eg Raman active fundamentals of TiO_2. The Eg and A1g modes of the rutile phase are represented by the bands detected at 448 cm^{-1} and 611.5 cm^{-1}.The spectrum measured for this sample in (Figure (3.27)) clearly confirms the presence of both TiO_2 crystalline phases for P25, since it comprises all of the distinctive bands related to the anatase and rutile phases. All of the Raman bands of TiO_2 are the same for TiO_2/CNTs composites, with

the exception of the TiO_2 Raman bands at 150 cm^{-1}. All of the Raman bands for TiO_2 and CNTs are still present, with the exception that the TiO_2 Raman bands for TiO_2/CNTs composites are slightly broadened compared to pure TiO_2. This broadening of the peak corresponds to a decrease in the average crystallite size. Importantly, the two peaks corresponding to CNTs in the Raman spectra for TiO_2/CNTs composites are noticeable. Furthermore, as the load of CNTs increases, these two peaks become more prominent. This is due to the fact that when comparing pure TiO_2 to composites, the composites are slightly broadened [279,280]. The changes in peak broadening are minor, possibly because the CNT ratios utilized in this study were quite modest. Figures (3.25) to (3.32) show the Raman spectra for all synthesized composites.

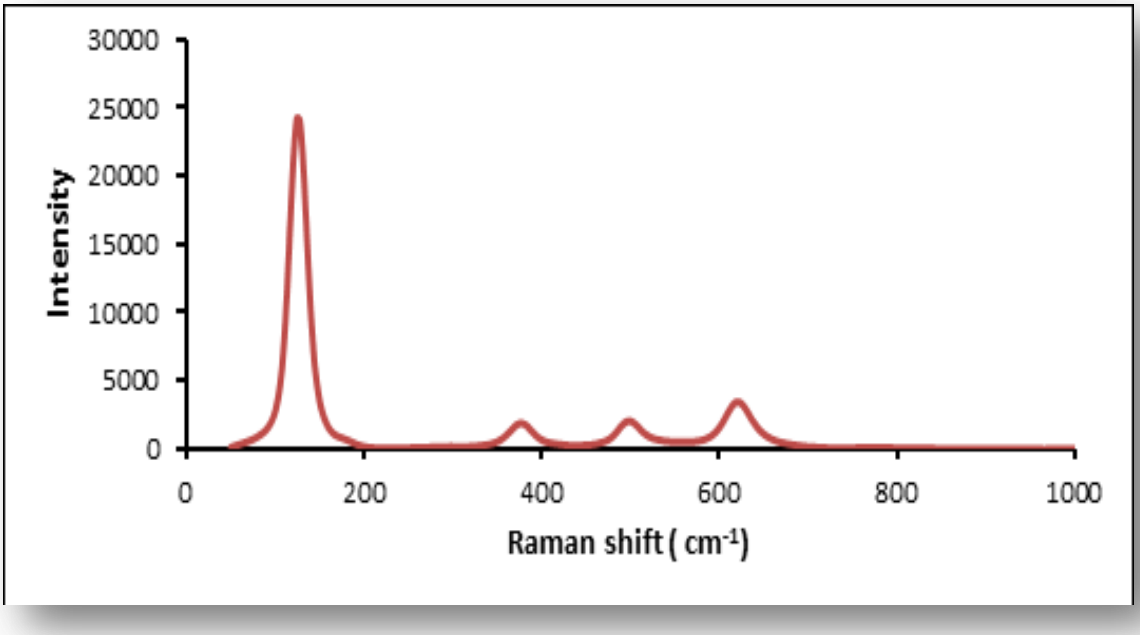

Figure (3.23): Raman spectrum of the TiO_2 anatase.

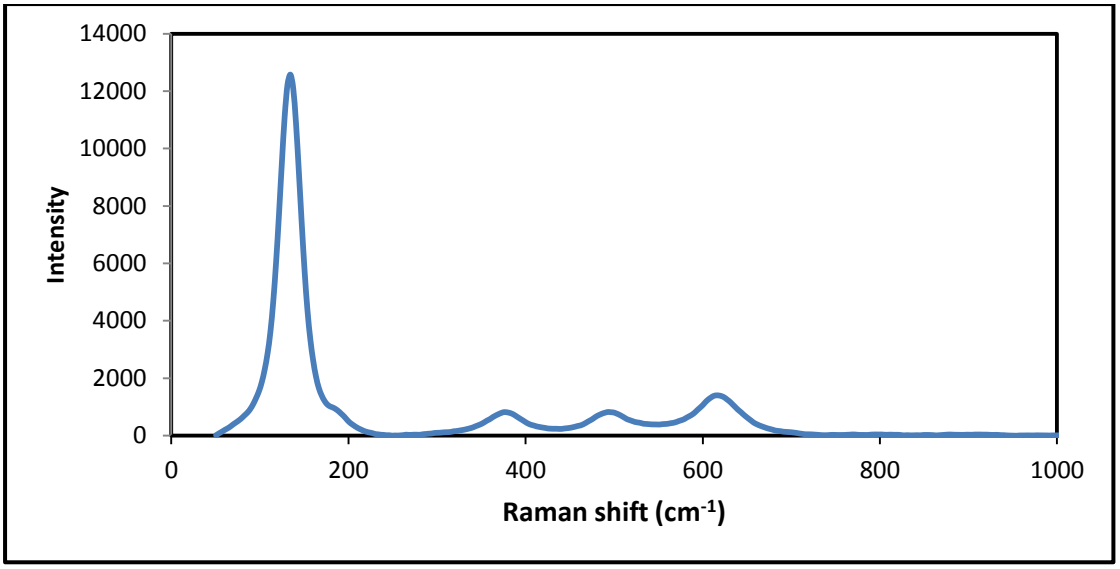

Figure (3.24): Raman spectrum of the TiO_2 anatase/0.01 CNTs.

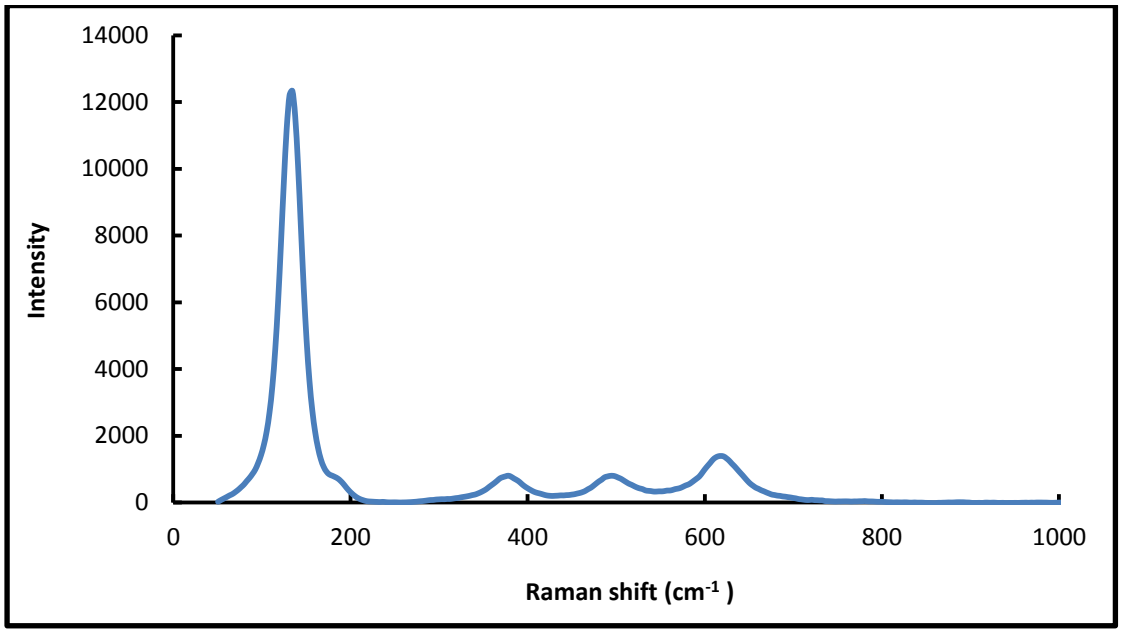

Figure (3.25): Raman spectra of the TiO_2 anatase/0.025 CNTs.

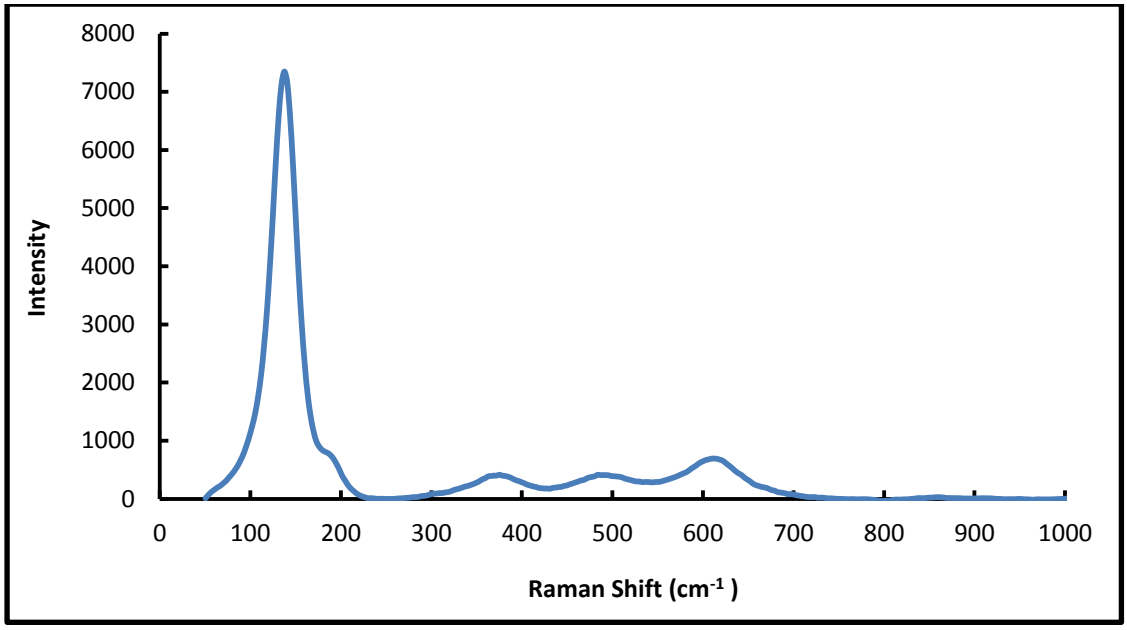

Figure (3.26): Raman spectrum of the TiO_2 anatase/0.05 CNTs.

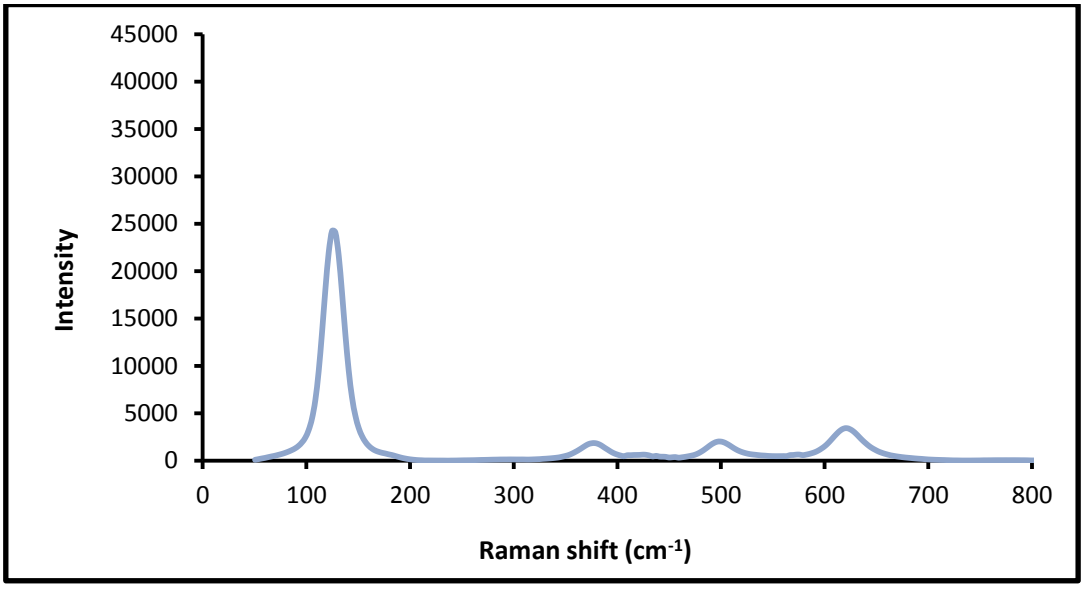

Figure (3.27): Raman spectrum of the TiO_2 degussa.

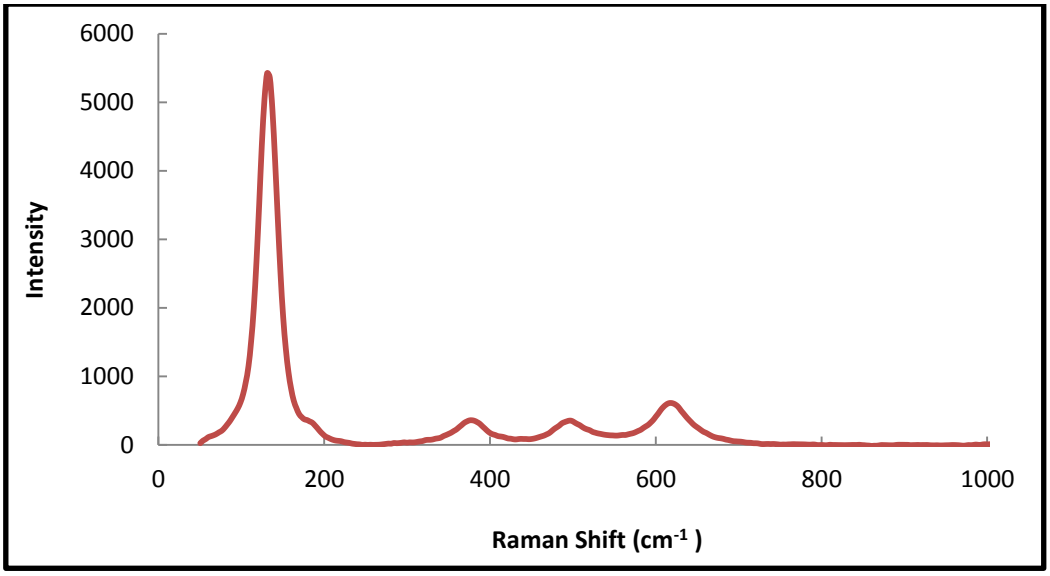

Figure (3.28): Raman spectrum of the TiO_2 degussa/0.01CNTs.

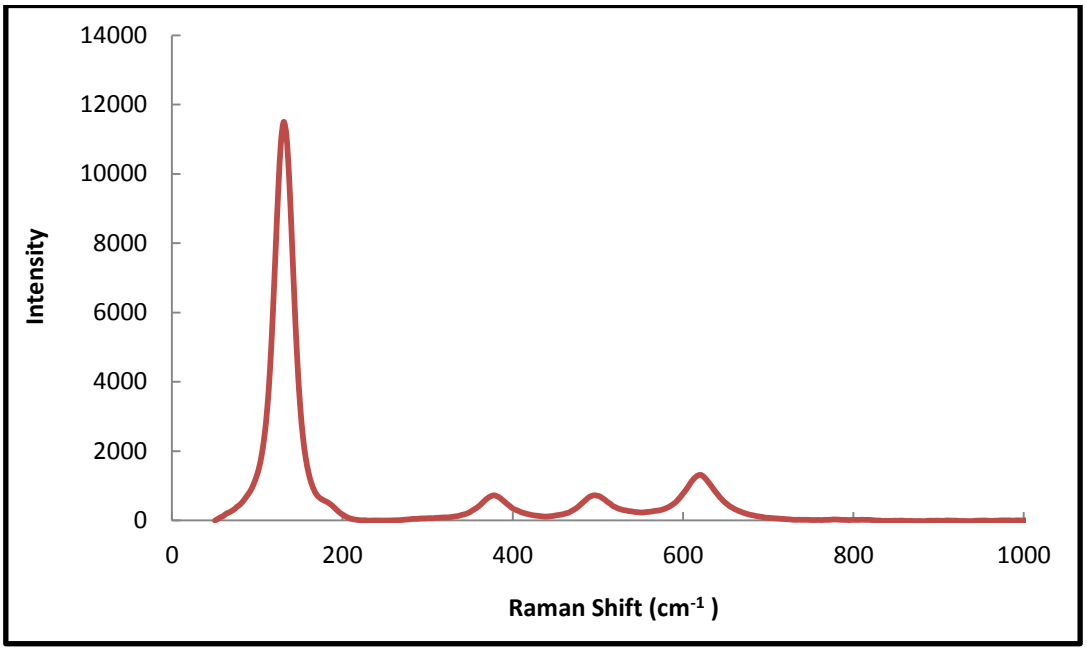

Figure (3.29): Raman spectrum of the TiO_2 degussa/0.025 CNTs.

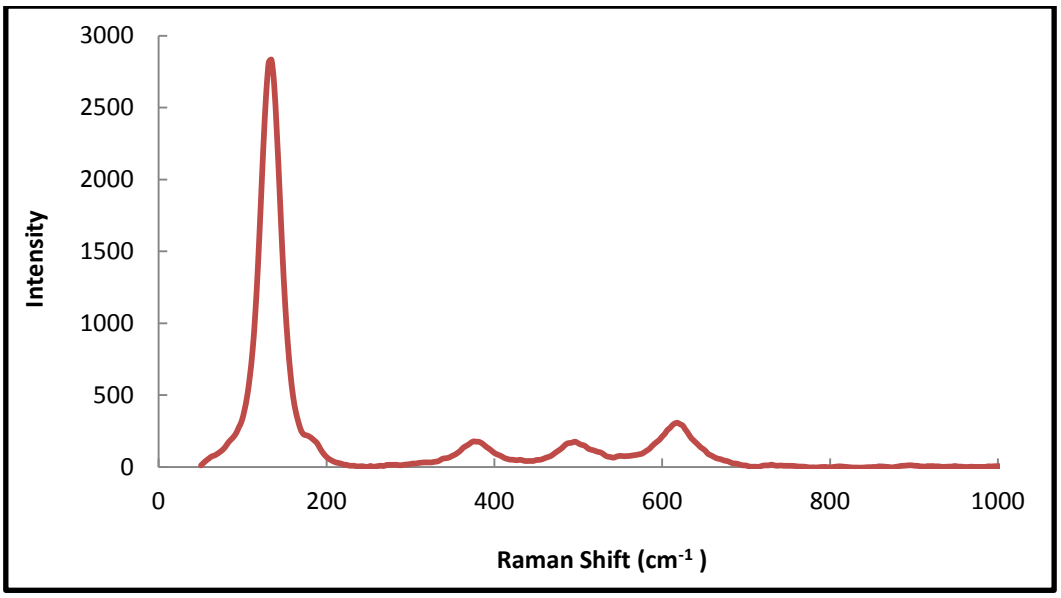

Figure (3.30): Raman spectrum of the TiO_2 degussa/0.025 CNTs.

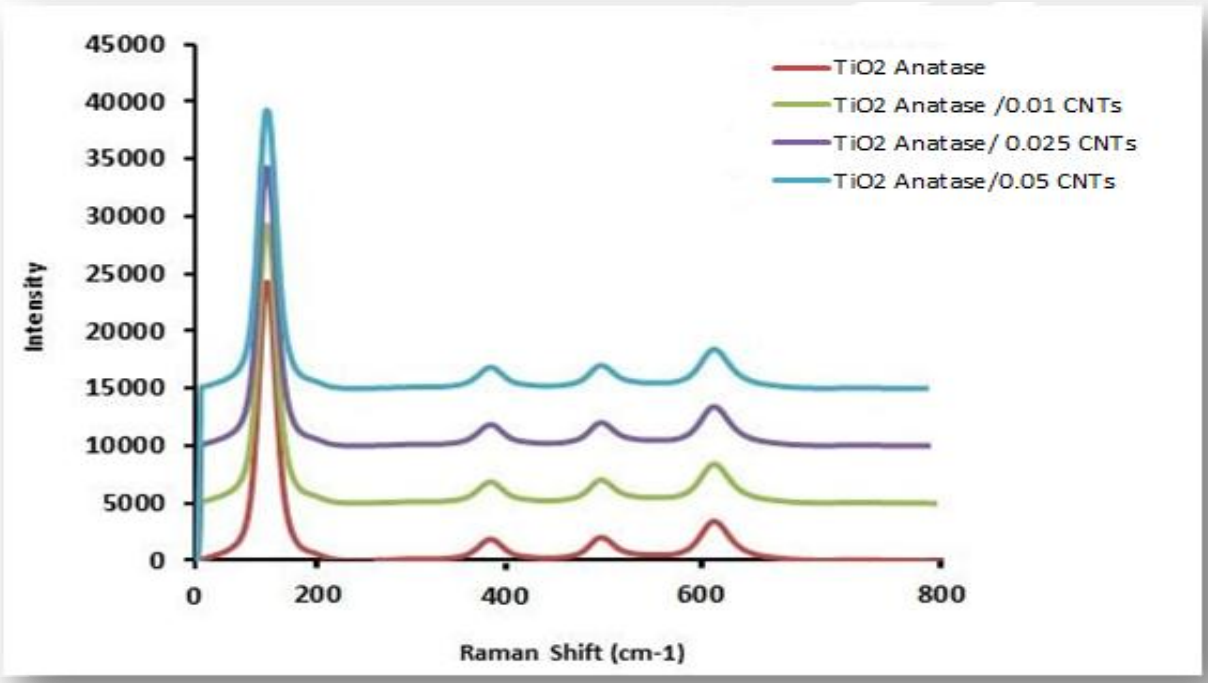

Figure (3.31): Raman spectrum of TiO_2 anatase/ CNTs composites.

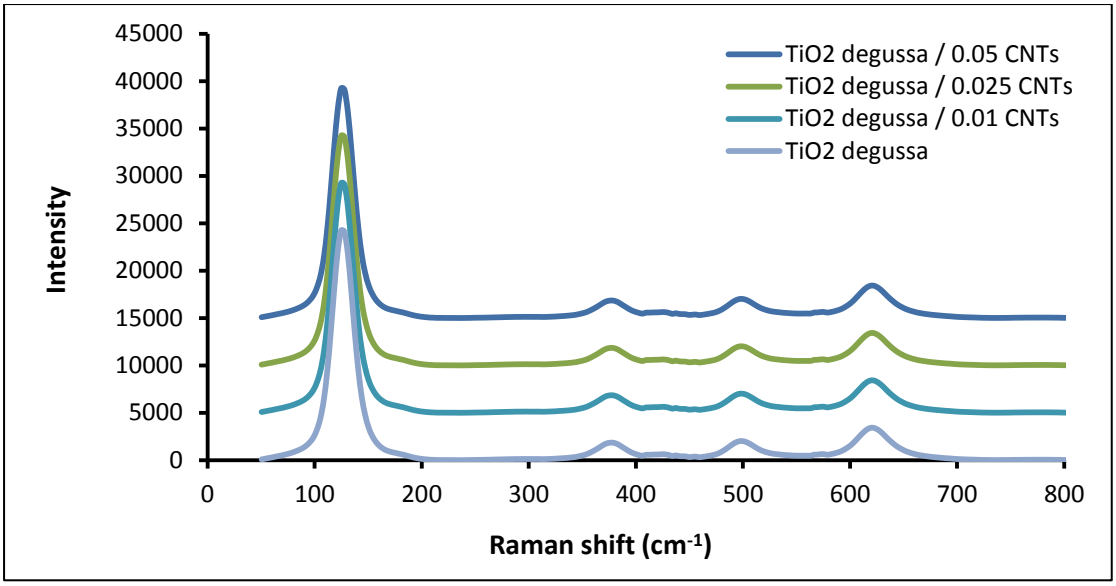

Figure (3.32): Raman spectra of TiO_2 degussa/ CNTs composites.

3.3.3 UV–visible diffuse reflectance spectra

Figures (3.33) to (3.37) show the diffuse reflectance spectra of TiO_2 (anatase & degussa), CNTs, and TiO_2/CNTs composite in the UV–vis. region. The inclusion of CNTs causes the composite material to absorb from 400 to 800 nm, and the absorption even covers the entire visible region. Furthermore, the absorption edge of TiO_2/CNTs nanocomposites exhibits a considerable red shift to a higher wavelength, which might be attributed to electrical interaction between CNTs and TiO_2 [281]. As a result, the TiO_2/CNTs composites should have outstanding photocatalytic activity that can be observed. The composites exhibit strong absorption capabilities not only in ultraviolet but also in visible light, which is important for exploitation and utilization of solar energy resources in solar cell [282].

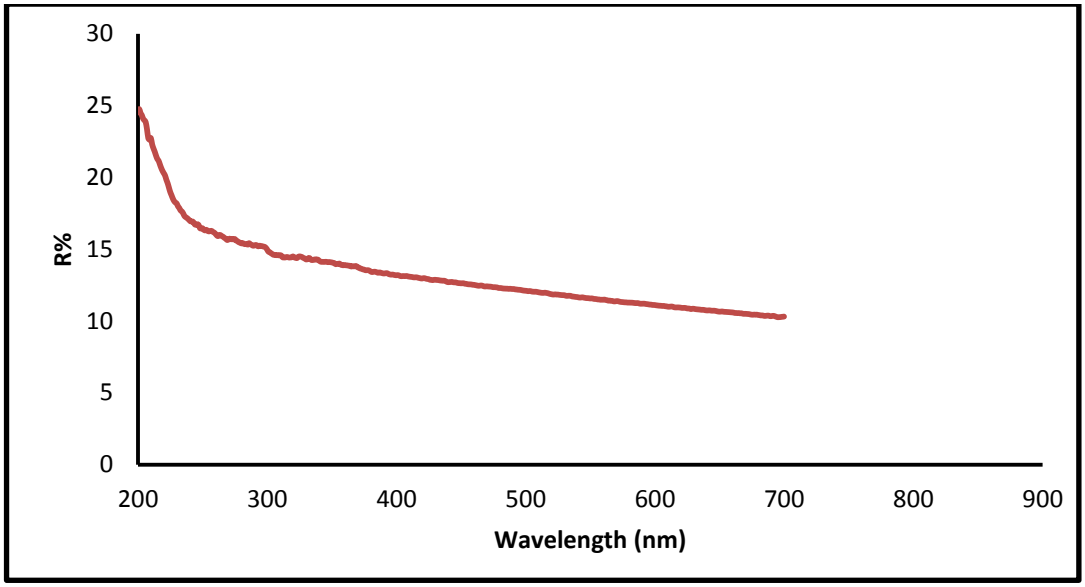

Figure (3.33): UV-Vis diffuse reflectance spectrum of the synthesized CNTs.

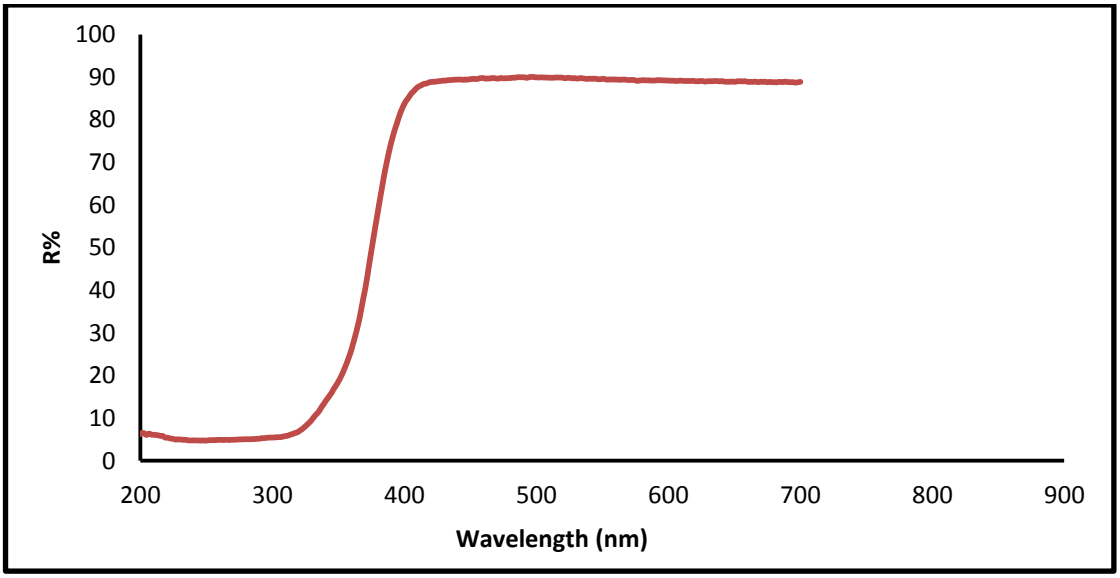

Figure (3.34): UV-Vis diffuse reflectance spectrum of TiO_2 anatase.

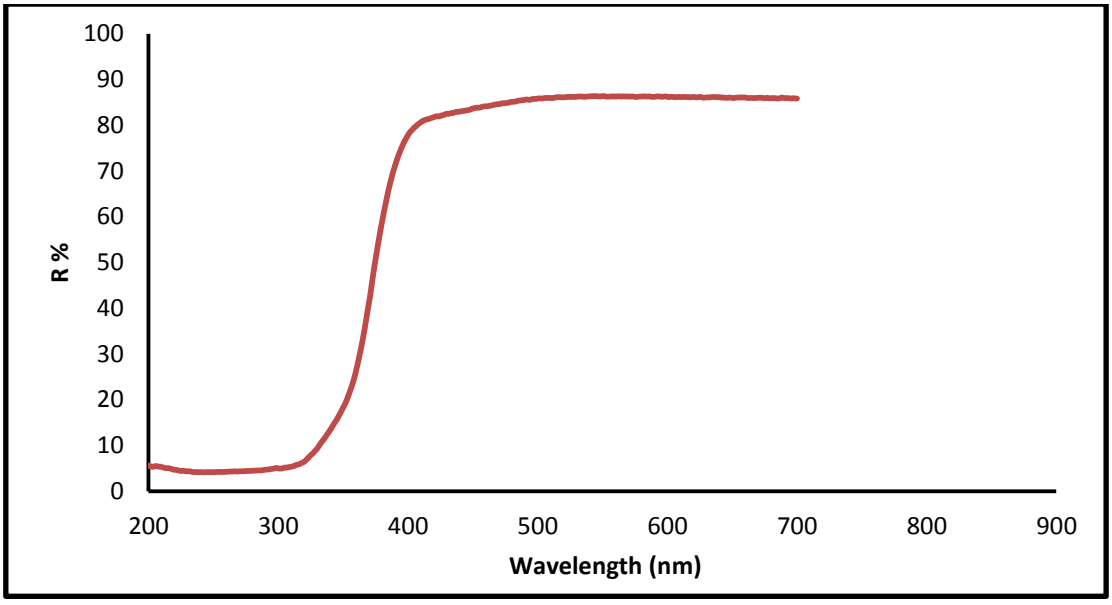

Figure (3.35): UV-Vis diffuse reflectance spectrum of TiO_2 degussa.

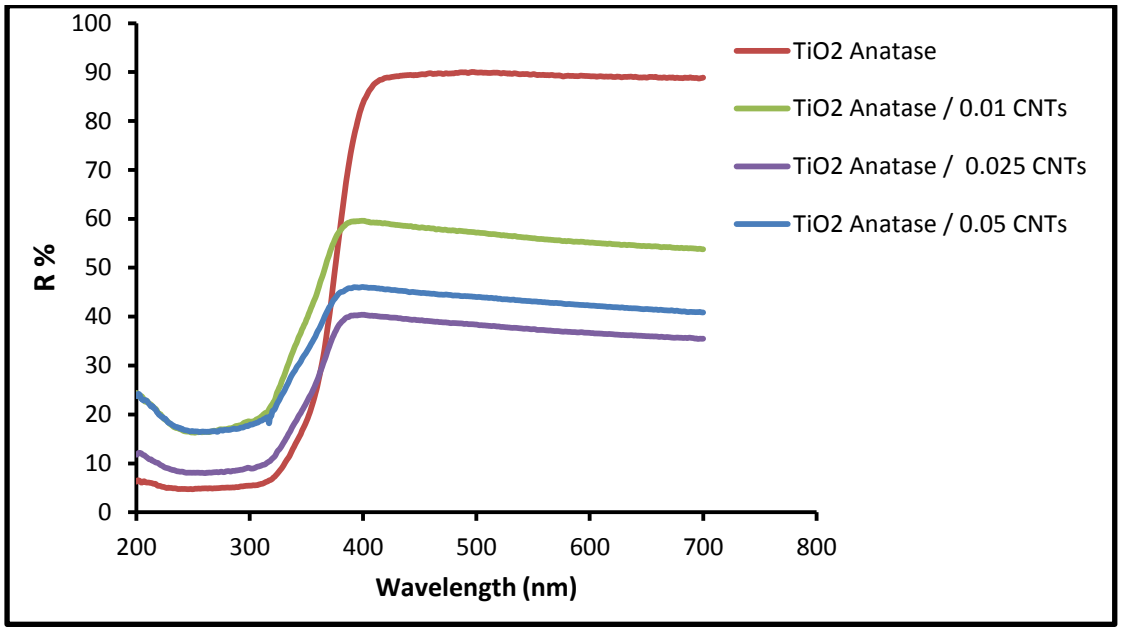

Figure (3.36): UV-Vis diffuse reflectance spectrum of TiO_2 anatase/ CNTs composite.

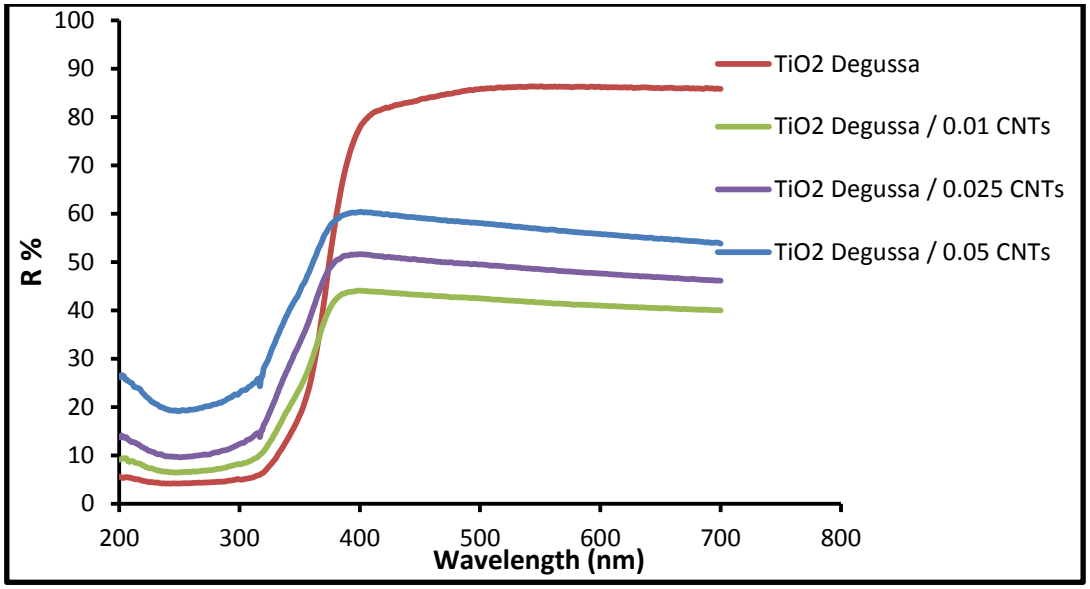

Figure (3.37): UV-Vis diffuse reflectance spectrum of TiO_2 degussa/ CNTs composite.

The diffuse reflectance UV–vis spectra of the different solids samples are measured in terms of Kubelka-Munk equivalent absorption units, as presented in figures (3.38) to (3.46) for synthesized CNTs, TiO_2 (anatase, degusa) and its composites with synthesizrd CNTs, The absorption edges are determined using the following equation once the band gaps have been anticipated:

$$Eg = 1239.8/\lambda \text{ -------(3.2)}$$

where λ is the optical absorption edge (nm) and Eg is the band gap (eV). Table (3.6) shows the band gaps and absorption edges of the synthesized samples.

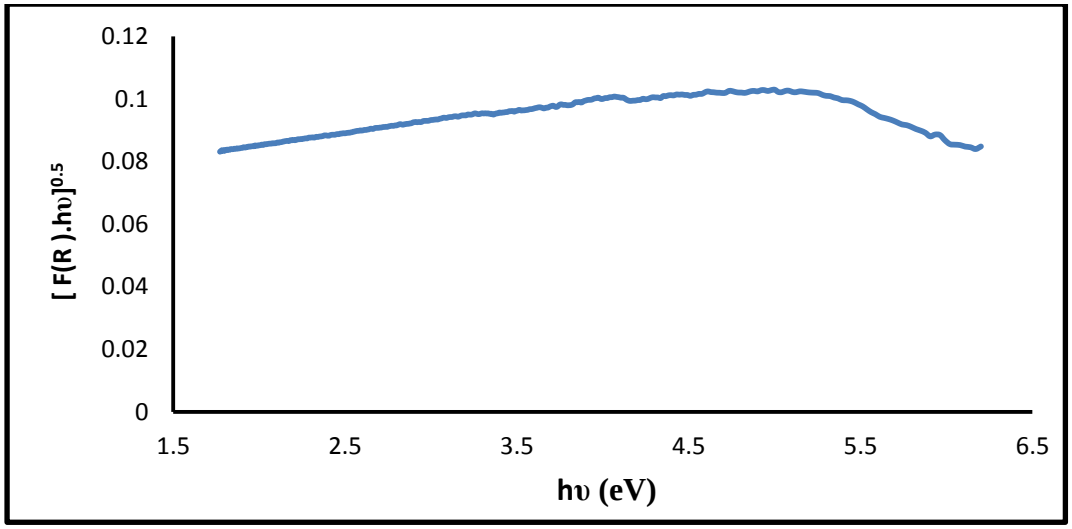

Figure (3.38): Kubelka-Munk curve for estimating the band gap of the synthesized CNTs.

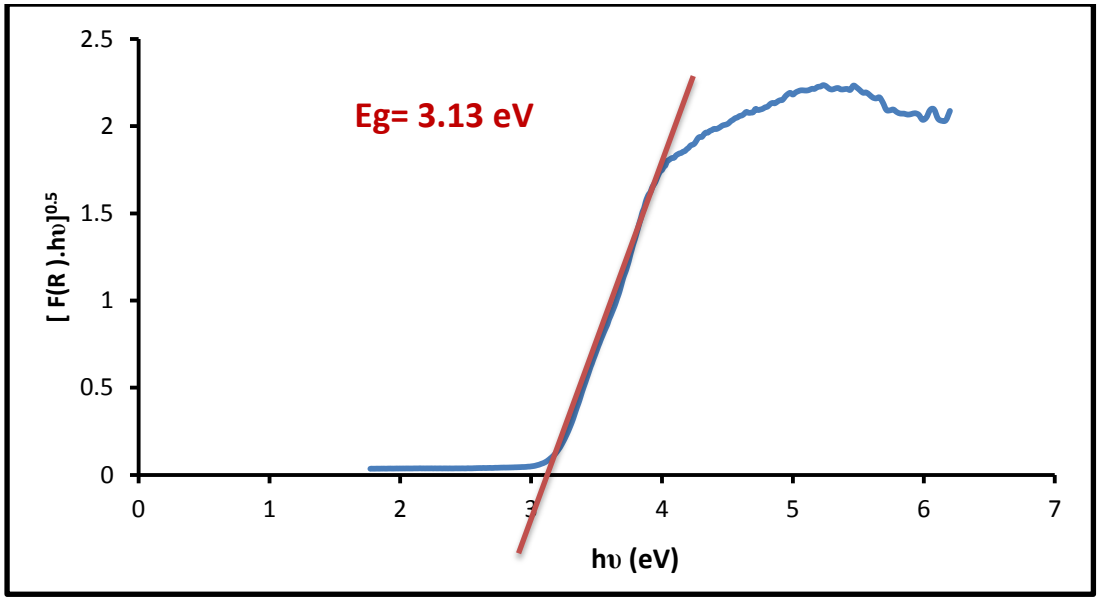

Figure (3.39): Kubelka-Munk curve for estimating the band gap of TiO_2 anatase.

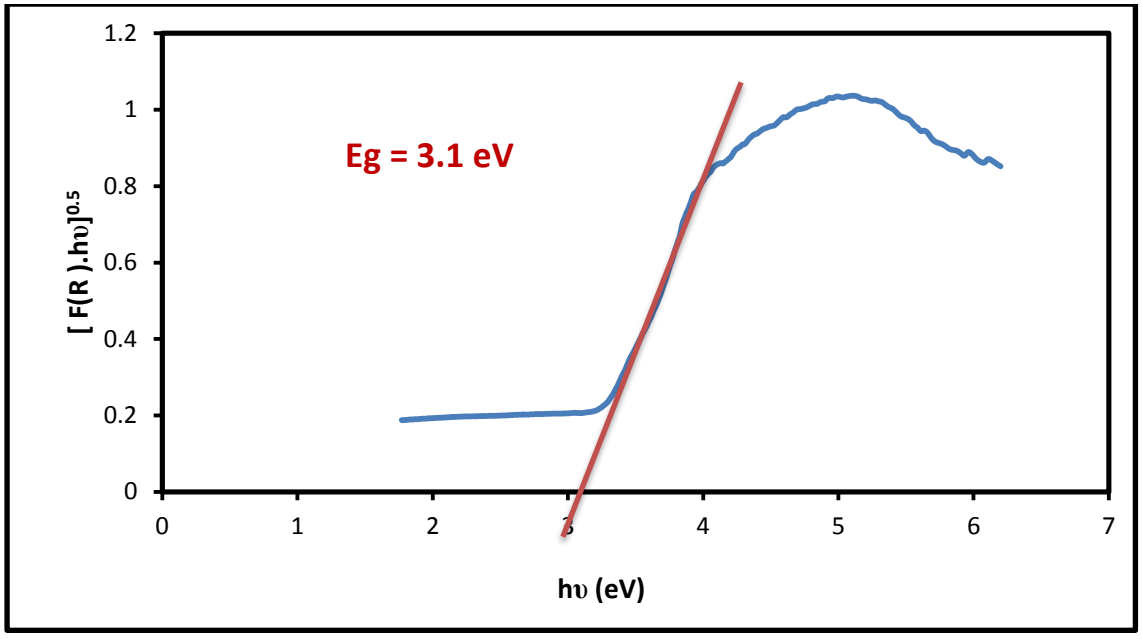

Figure (3.40): Kubelka-Munk curve for estimating the band gap of the synthesized TiO_2 anatase/0.01CNTs composite.

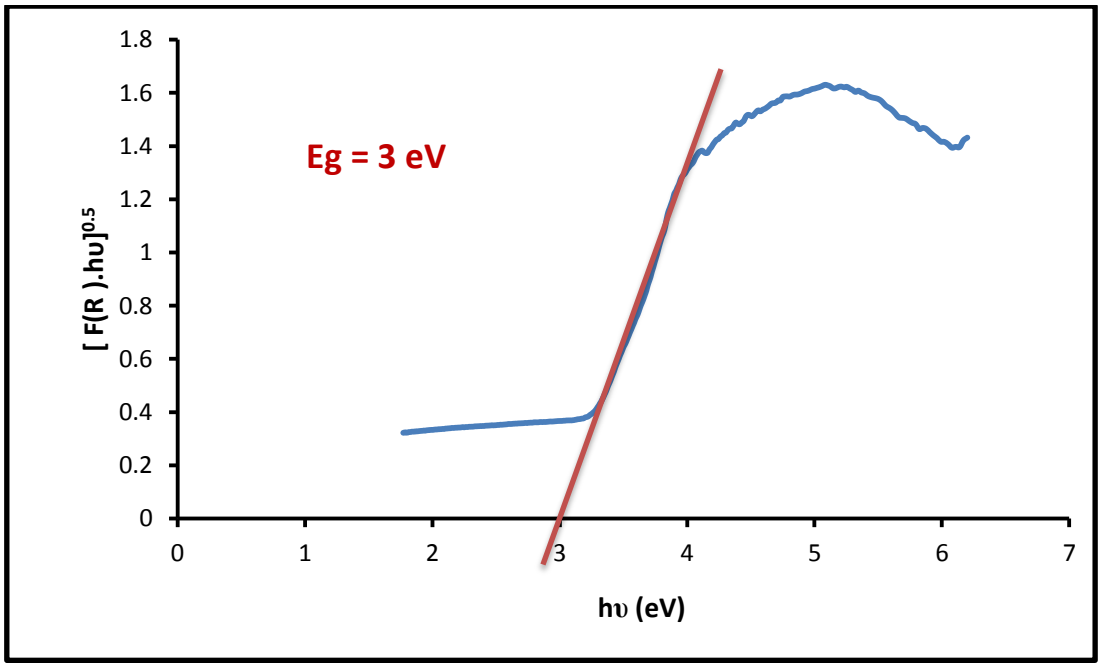

Figure (3.41): Kubelka-Munk curve for estimating the band gap of the synthesized TiO_2 anatase/0.025CNTs composite.

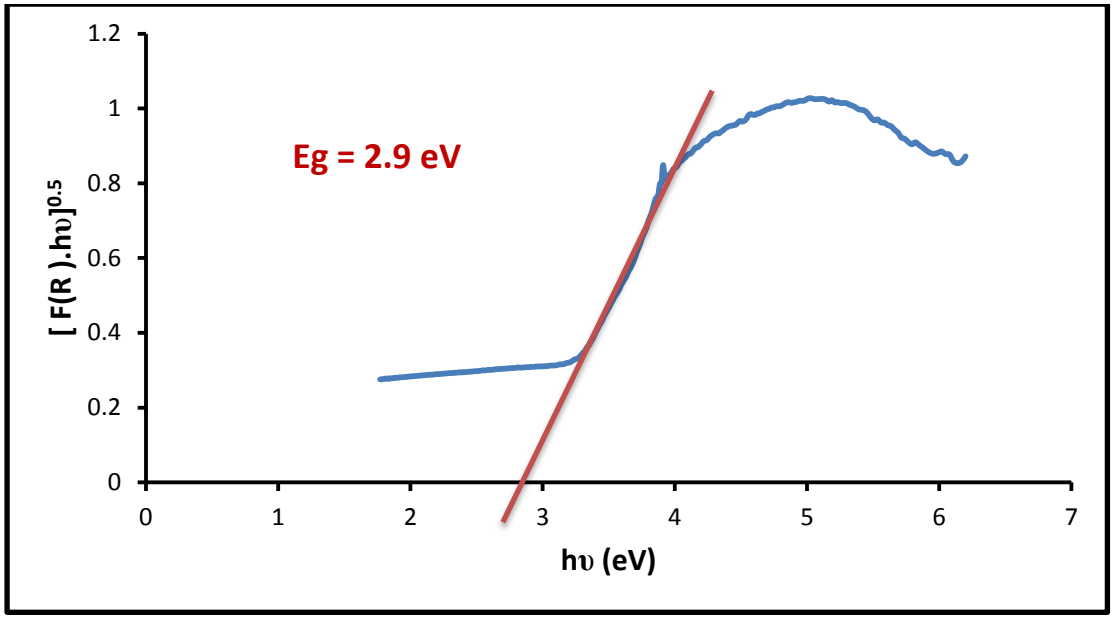

Figure (3.42): Kubelka-Munk curve for estimating the band gap of the synthesized TiO_2 anatase/0.05CNTs composite.

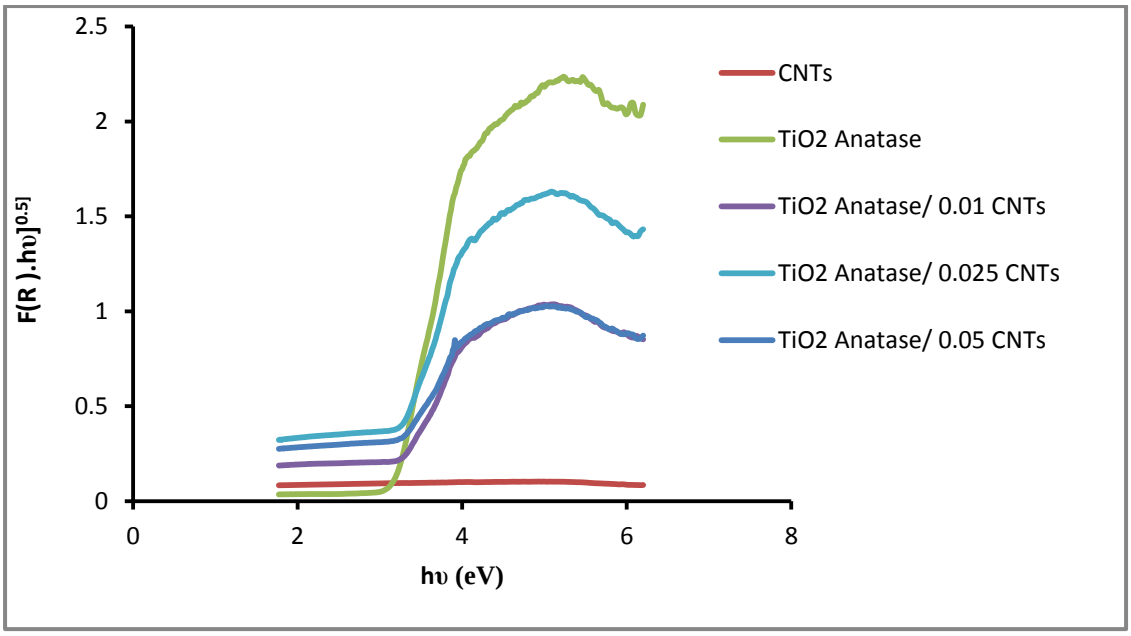

Figure (3.43): Kubelka-Munk curves for estimating band gap of TiO_2 anatase/CNTs composite.

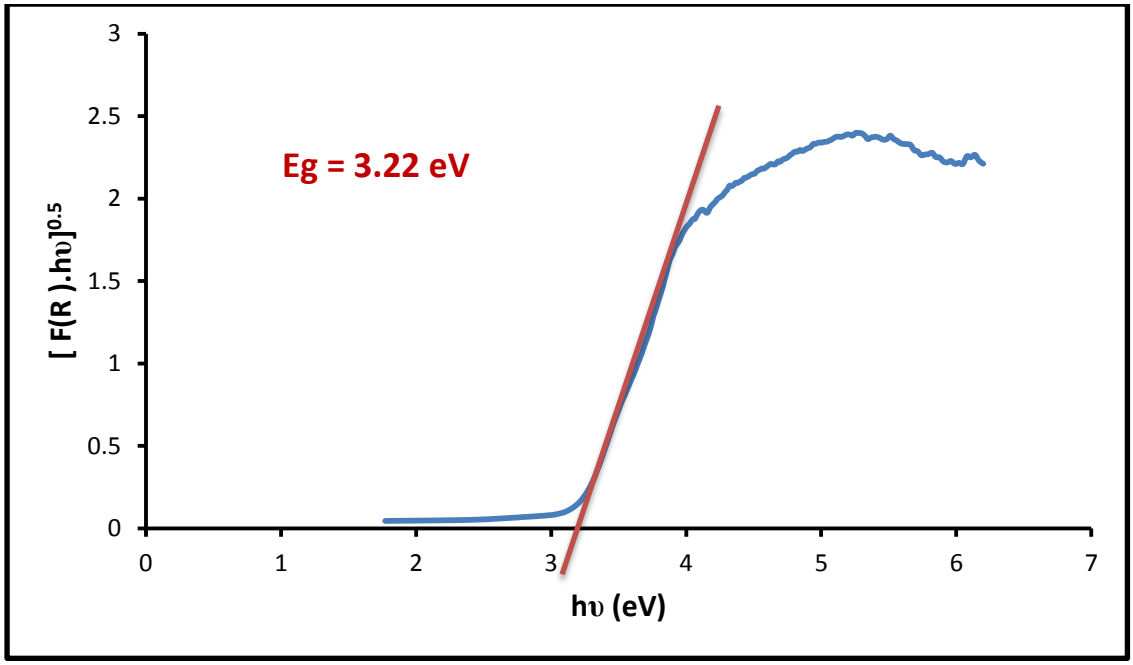

Figure (3.44): Kubelka-Munk curve for estimating the band gap of the TiO_2 degussa.

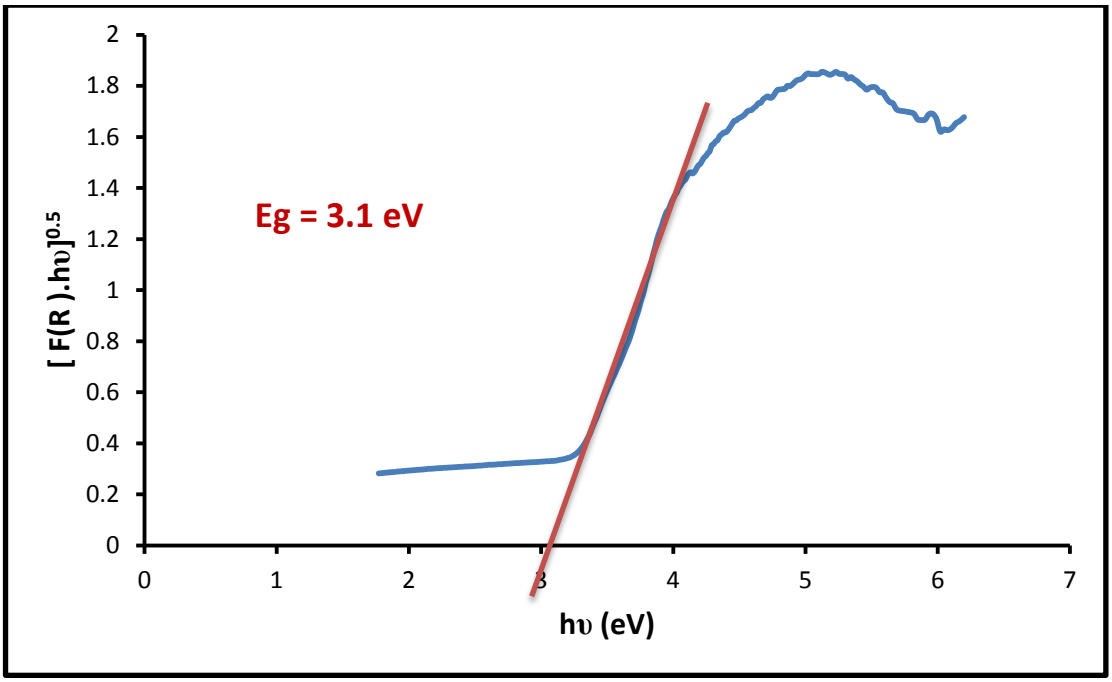

Figure (3.45): Kubelka-Munk curve for estimating the band gap of the synthesized TiO_2 degussa/0.01CNTs composite.

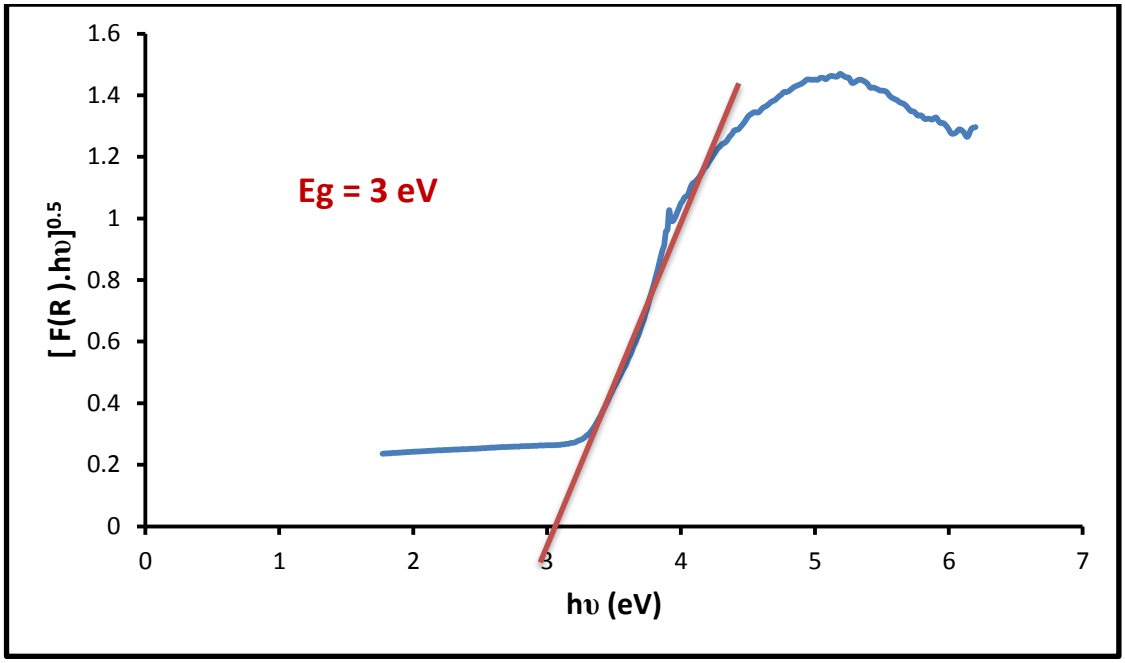

Figure (3.46): Kubelka-Munk curve for estimating the band gap of the synthesized TiO_2 degussa/0.025CNTs composite.

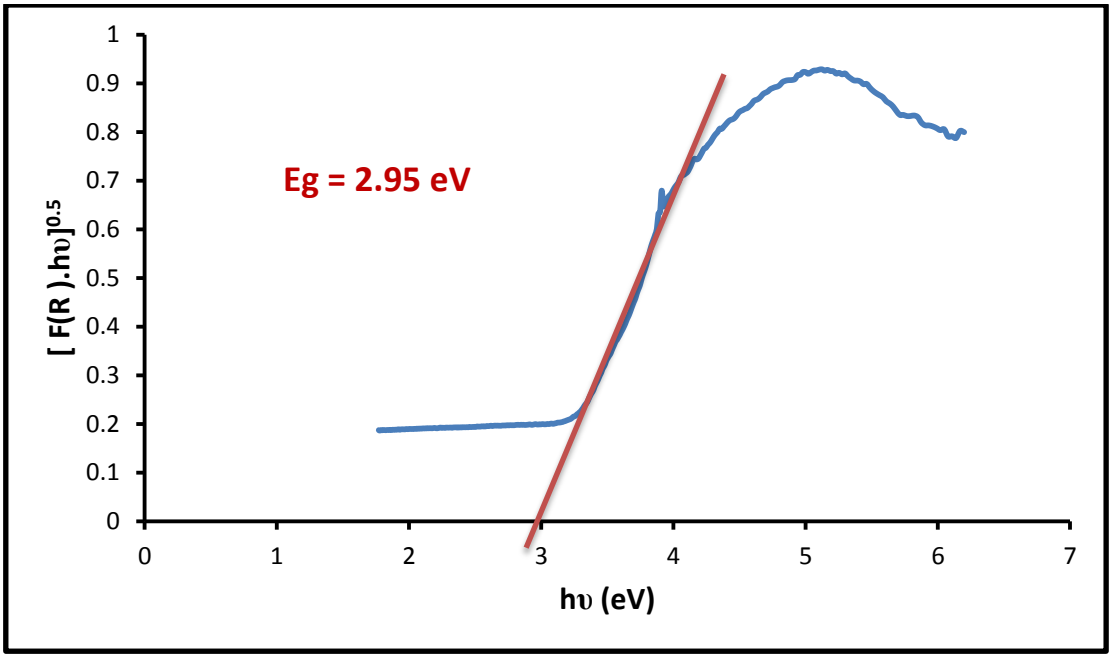

Figure (3.47): Kubelka-Munk curve for estimating the band gap of the synthesized TiO_2 degussa/ 0.05CNTs composite.

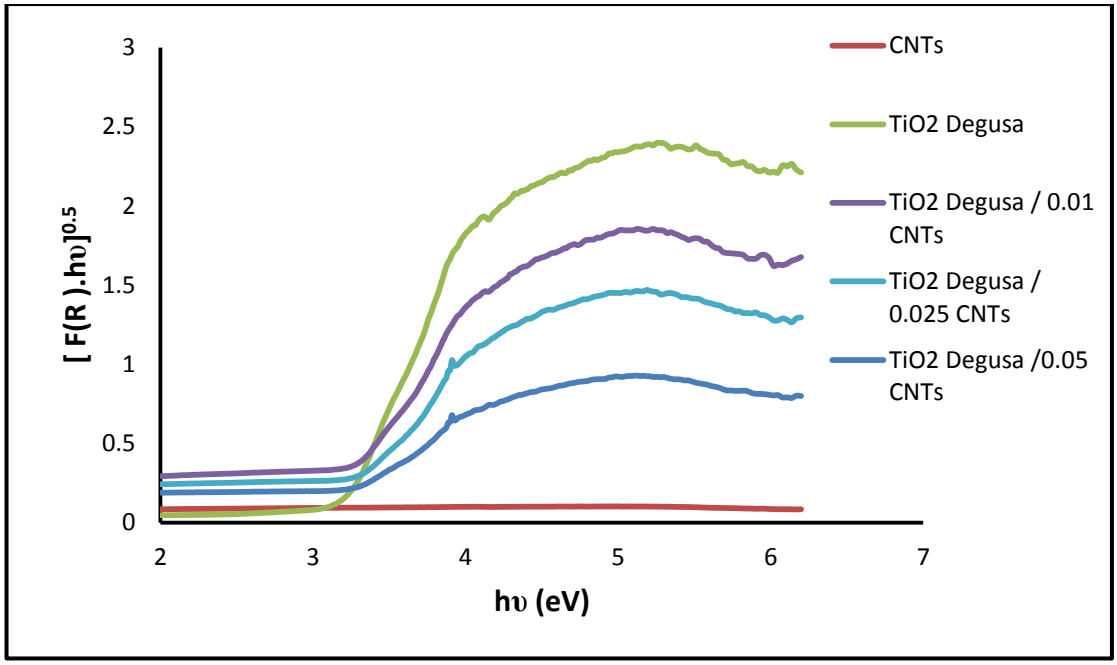

Figure (3.48): Kubelka-Munk curves for estimating band gap of TiO_2 degussa/ CNTs composite.

Table (3.6): The band gaps and adsorption edges.

Sample	Band Gap (e V)	Absorption Edge (nm)
TiO_2 anatase	3.13	396.100
TiO_2 anatase + 0.01CNTs	3.10	399.935
TiO_2 anatase + 0.025CNTs	3.00	413.266
TiO_2 anatase + 0.05CNTs	2.90	427.517
TiO_2 degussa	3.22	385.030
TiO_2 degussa + 0.01CNTs	3.10	399.935
TiO_2 degussa + 0.025CNTs	3.00	413.266
TiO_2 degussa + 0.05CNTs	2.95	420.271

According to the results listed in Table (3.6) and figures (3.38) to (3.46), the band gap values for TiO_2 (anatase & degussa) and synthesized TiO_2(anatase & degussa)/CNTs nanocomposite are 3.13, 3.22, 3.1, 3, 2.9, 3.1, 3 and 2.95 eV; respectively. Reducing band gap energy involves using low energy to accelerate electron excitation from the valance band to the conducting band, resulting in more electron/positive hole pairs and improving the photocatalytic process [283,284]. However, the surface area and density of adsorption active sites influence the photocatalytic reaction as well as the band gap energy value. The small optical differences seen in our composite could be due to the formation of CNTs within the pores of TiO_2 NRs and on their surfaces, which could limit the interaction between incident light and TiO_2 as an active component for light. However, this results in a significant increase in specific surface area and the presence of numerous active adsorption sites, which is expected to improve the efficiency of photocatalytic reaction.

3.3.4. SEM for TiO_2 / CNTs composite

Scanning electron microscopy (SEM) was used to examine the morphology of the used TiO_2 (anatase & degussa)/CNTs composite. Compared to pure synthesized CNTs (Figures (3. 47) to (3.52)), the TiO_2/CNTs preserve the one-dimensional nanostructure of the CNTs. The coarsening of CNTs surfaces indicates the presence of a TiO_2 coated surface. However, the presence of agglomerated particles is not under control during the synthesis procedure and weight fractions of primary materials affect the amount of coated and aggregated TiO_2 .The SEM images of nanocomposite indicate that the CNTs are homogenously distributed throughout the TiO_2 matrix with an obvious agglomeration of the TiO_2 particles. It is noticed from these images that the average diameter of carbon nanotubes increased slightly as a result of the accumulation of TiO_2 nanoparticles on its surface, with a small increase also in the particle size of the composites, some of which are very close to their crystallite size estimated by XRD diffraction measurement by applying Scherrer equation .

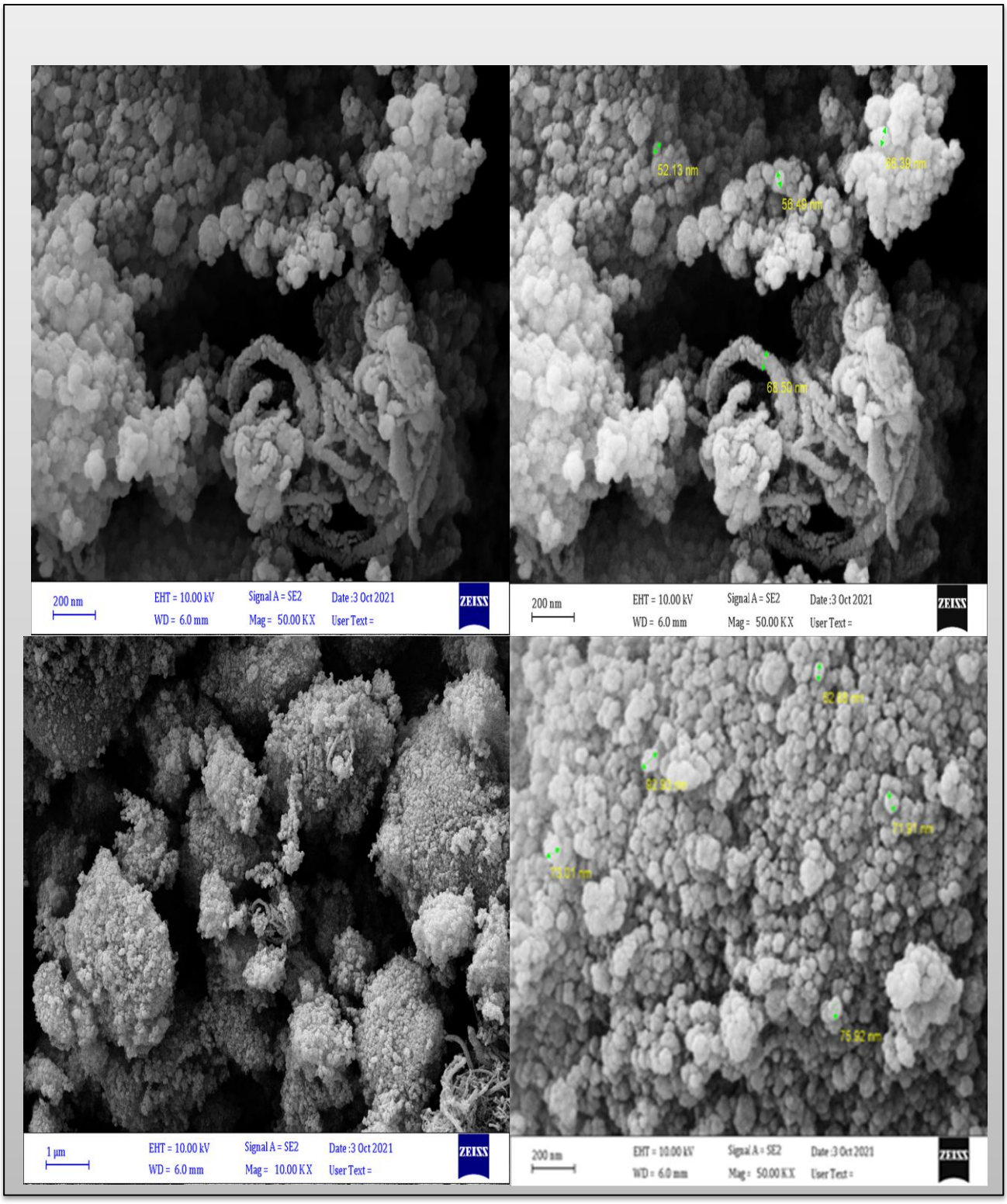

Figure (3.49): SEM images for TiO_2 anatase/0.01 CNTs composite.

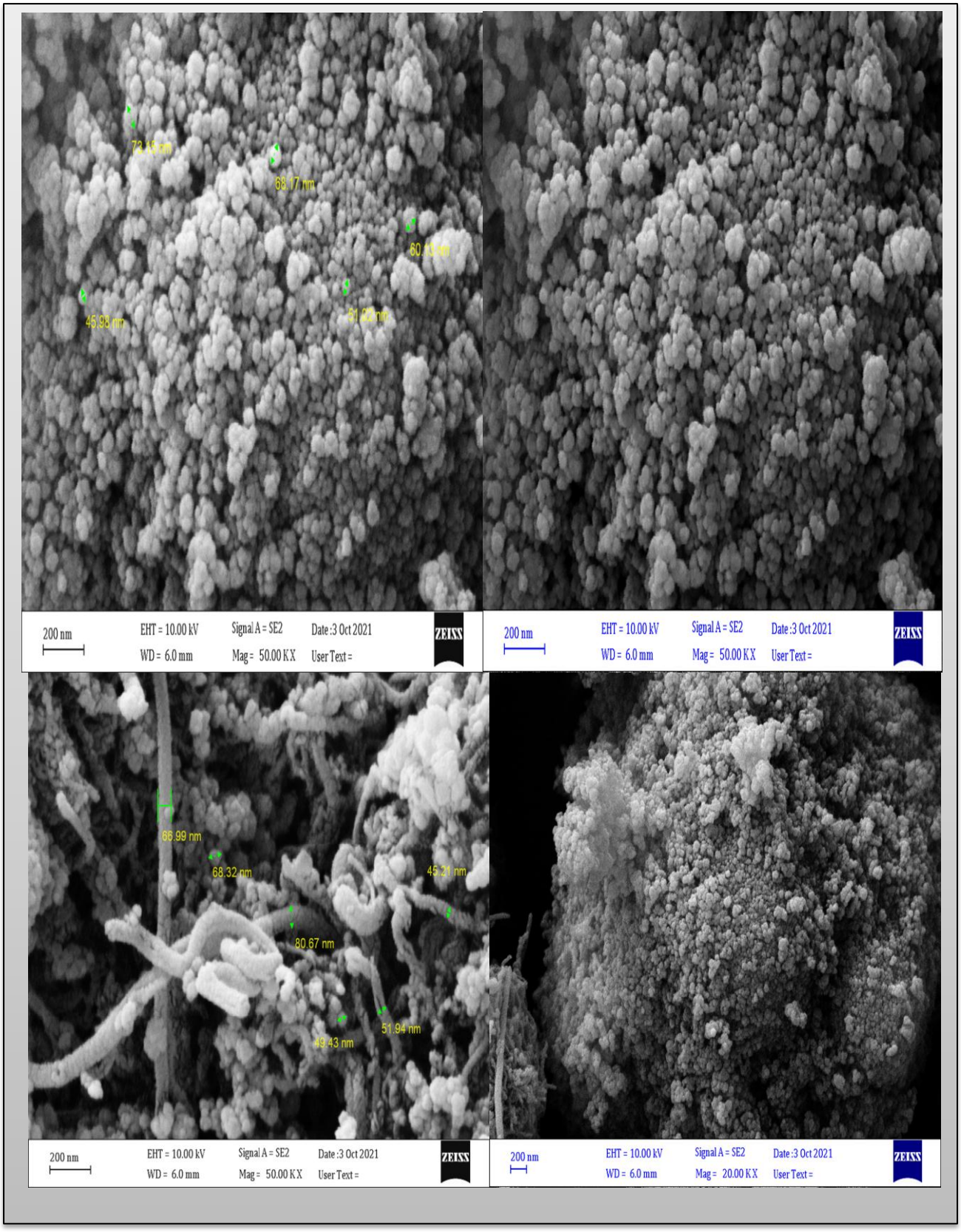

Figure (3.50): SEM images for TiO_2 anatase/0.025 CNTs composite.

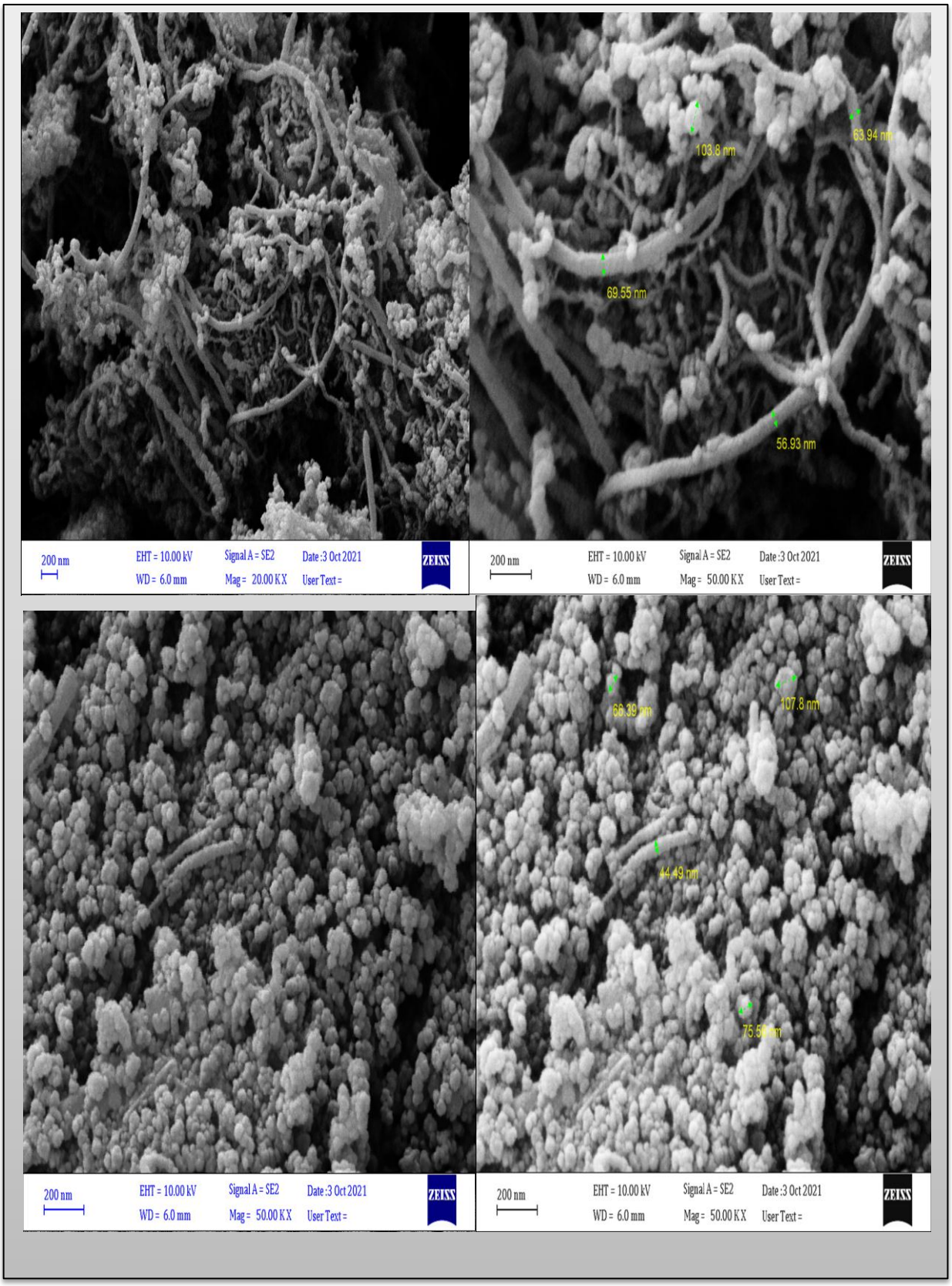

Figure (3.51): SEM images for TiO_2 anatase/0.05 CNTs composite.

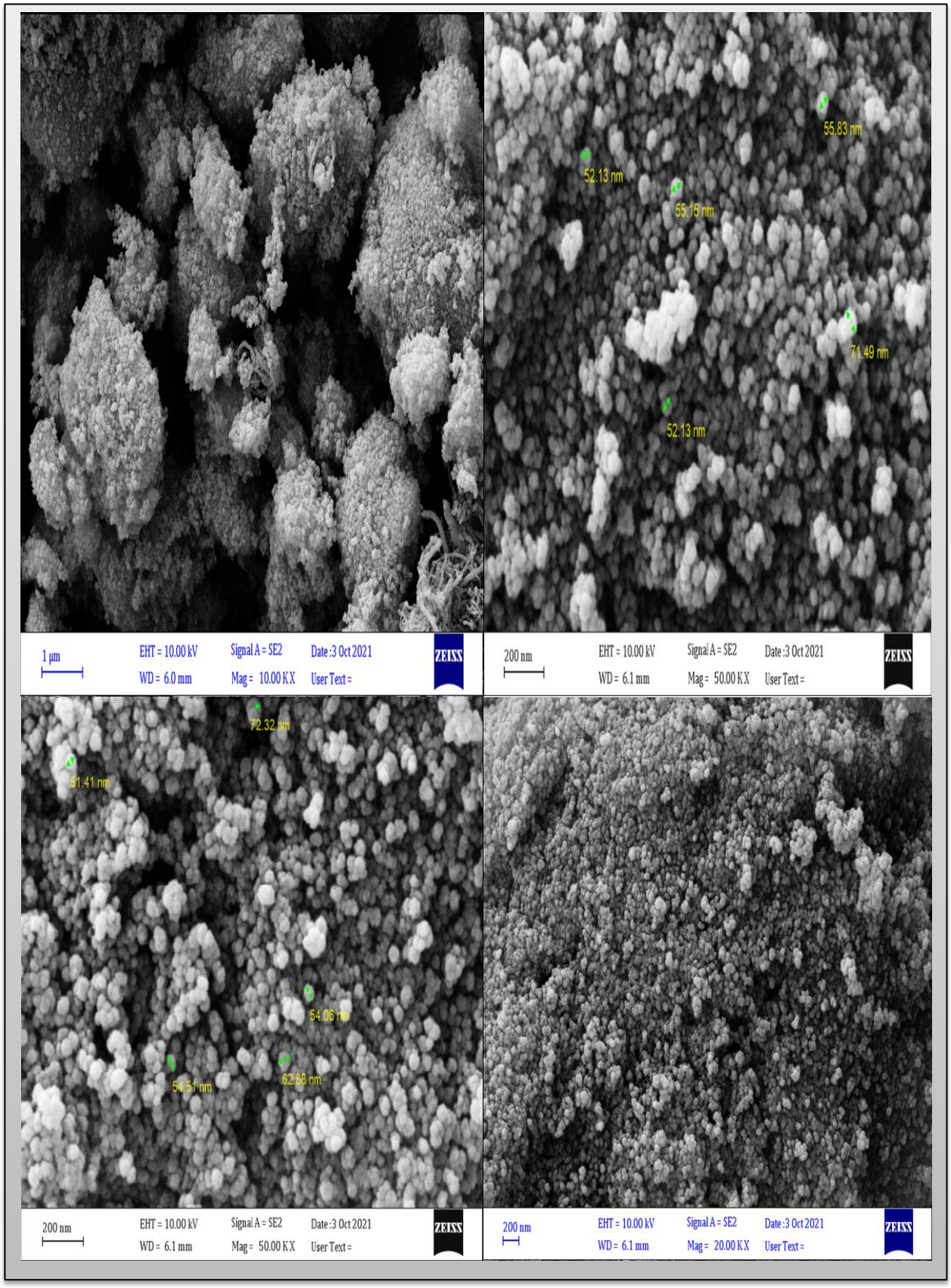

Figure (3.52): SEM images for TiO_2 degussa/0.01 CNTs composite.

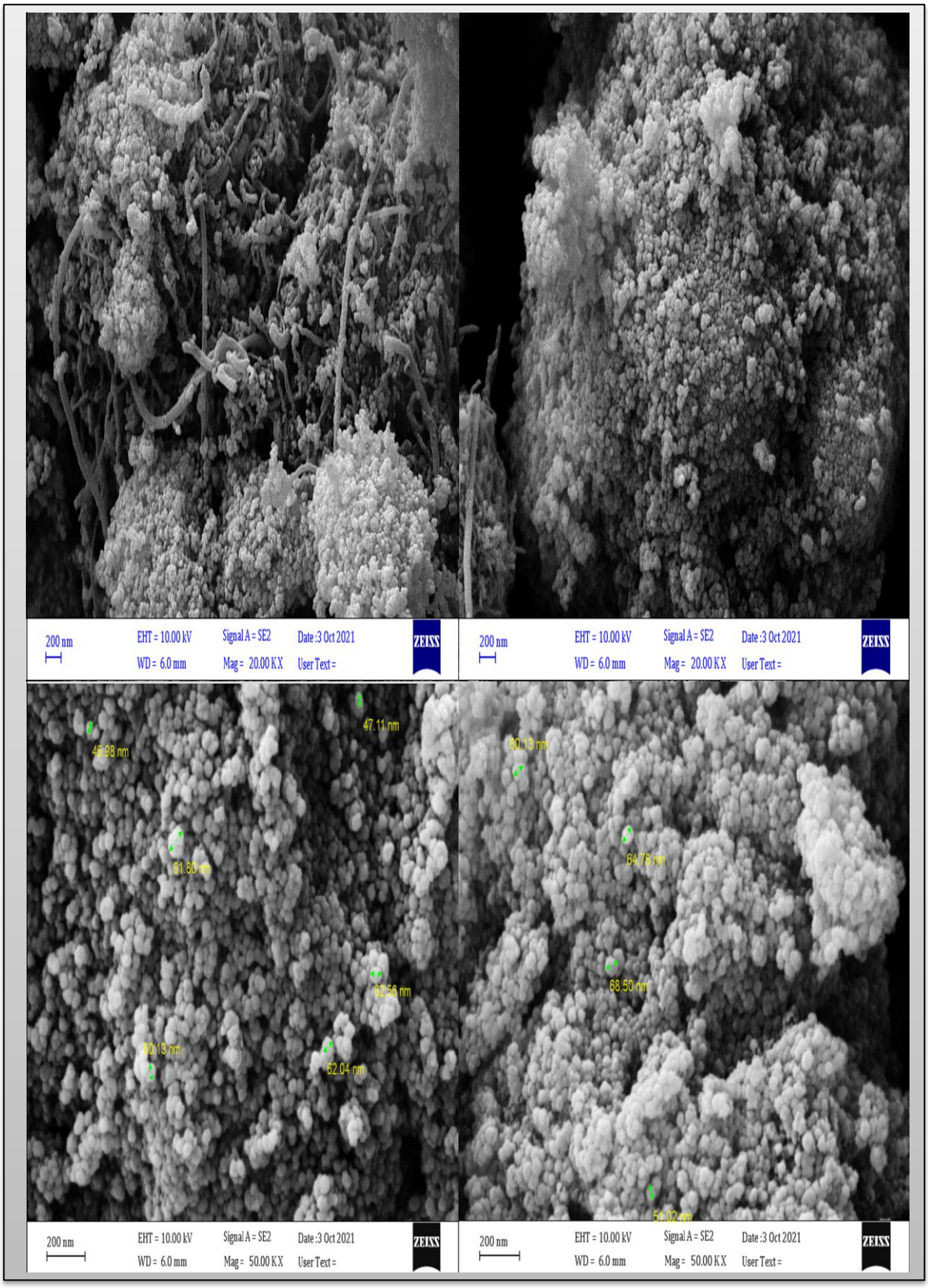

Figure (3.53): SEM images for TiO_2 degussa/0.025 CNTs composite.

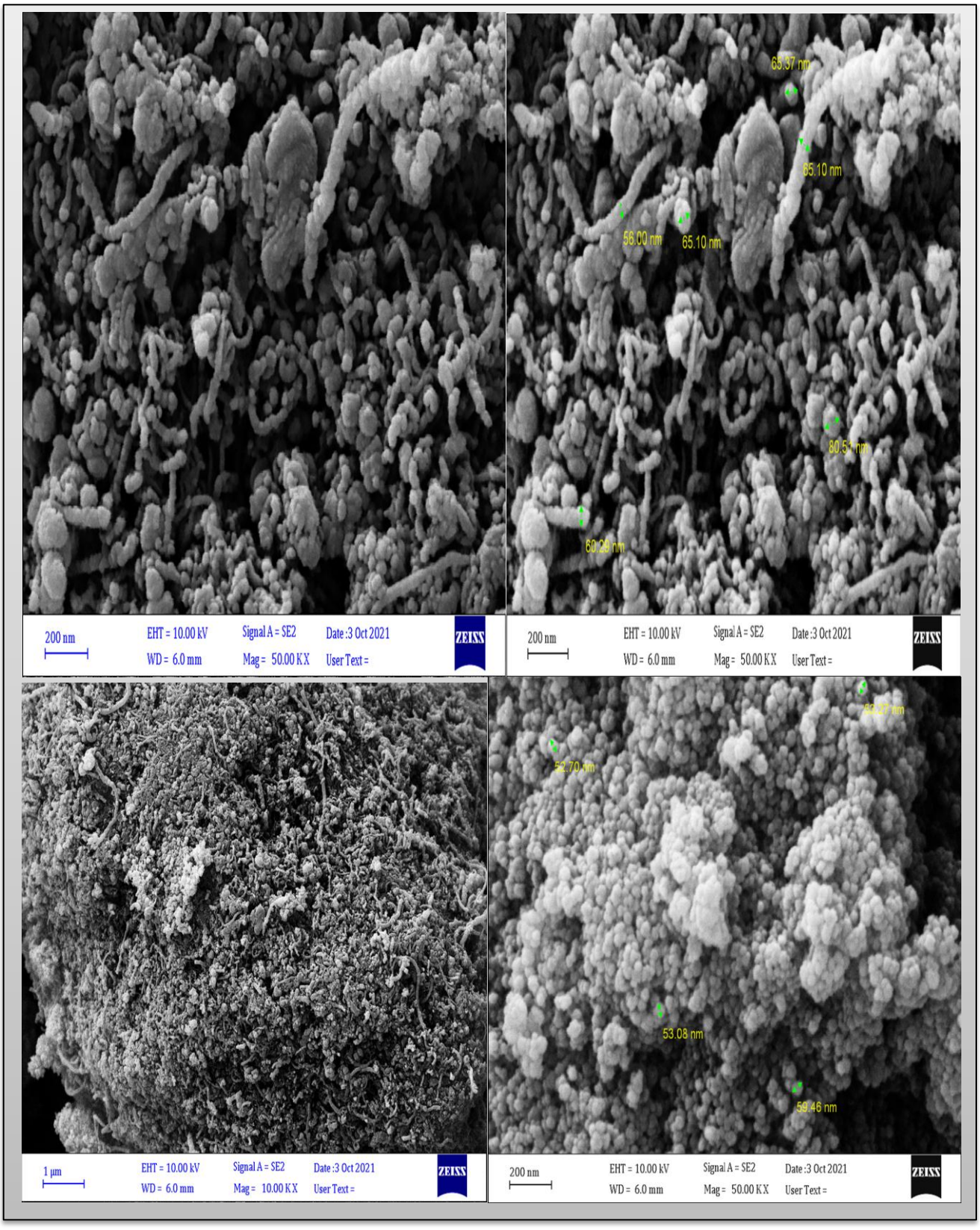

Figure (3.54): SEM images for TiO_2 degussa/0.05 CNTs composite.

3.3. Fabrication of Dye-Sensitized Solar Cells (DSSCs)

The solar cells were made using TiO_2 (anatase, degussa) and its composites with CNTs as the photoelectrode, as well as pomegranate seeds extract as a dye. The I-V and P-V characteristics of DSSCs are illustrated in figure (3.54) to (3.65). Tables (3.6) to (3.11) show the short-circuit current density (Jsc), open-circuit voltage (Voc), fill factor (FF = Jm*Vm/Jsc*Voc), and power conversion efficiency (PCE) of all the cells. The short circuit current is determined by the devices' I–V characteristics. The photoelectrodes used are TiO_2(anatase)/pt , TiO_2(degussa)/pt , TiO_2(anatase)CNTs composite/pt, TiO_2(degussa)CNTs compsite/p, TiO_2(anatase)/CNTs, TiO_2(degussa)/CNTs,TiO_2(anatase)CNTs composite/CNTs, TiO_2(degussa)CNTs compsite/CNTs, TiO_2(anatase)/Graphite, TiO_2(degussa)/Graphite, TiO_2(anatase)CNTs composite/Graphite, and TiO_2(degusa)CNTs compsite/Graphite .

The photovoltaic cells prepared using TiO_2 (degussa) were more efficient than those of TiO_2 (anatase) because the highly efficient commercial photocatalyst, degusa P25 is primarily composed of the anatase phase (80%) and a reasonable amount of rutile (15%). Also, the cells prepared from Pt counter electrode were more efficient than those of CNTs and graphite because Pt has a high exchange current density , good catalytic activity and transparency. TiO_2(degussa)/CNTs composite is considered the best photoelectrode and is more efficient than the others, especially when using Pt as the counter electrode. It is noticed that the type of electrode in the same dye has a very important role in improving the efficiency of the solar cell . Further, with respect to cost, the CNT counter electrode cheaper than the Pt counter electrode and is highly efficient, which makes it reasonable choice for use as counter electrode in DSSCs. The decrease in the efficiency of cells with increasing proportion

of carbon nanotubes and graphite is due to the darkness of the cell and the opacity of the fluorinated tin oxide (FTO) glass, and this would reduce the absorption of light by the dye. Furthermore, for all fabricated DSSCs is measured under intensity (34 mW/cm^2) of light source that is used. For all prepared DSSCs, A=2.25cm^2.

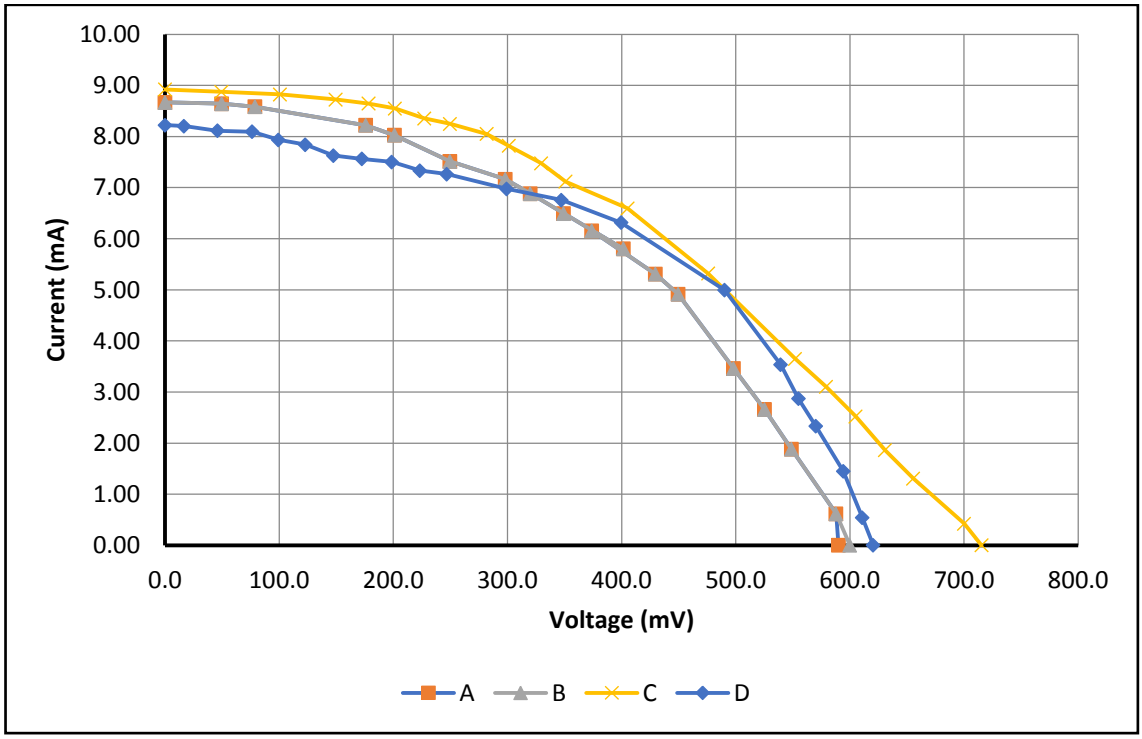

Figure (3.55): I-V characteristics of the fabricated DSSCs using, (A) TiO_2(degussa)/Pt , (B) TiO_2(degussa),0.01CNTs/Pt, (C) TiO_2(degussa), 0.025CNTs/Pt (D) TiO_2(degussa),0.05CNTs/Pt.

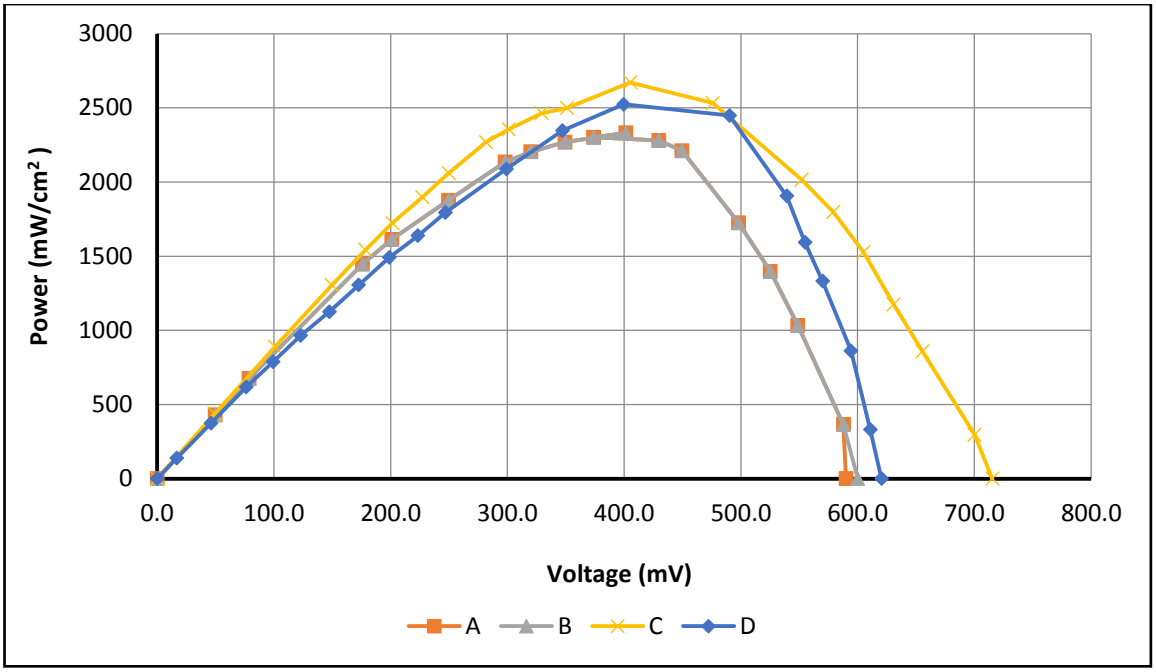

Figure (3.56): P-V characteristics of the fabricated DSSCs, (A) TiO_2(degussa)/Pt , (B) TiO_2(degussa),0.01CNTs /Pt, (C) TiO_2(degussa), 0.025CNTs/Pt, (D) TiO_2(degussa),0.05CNTs/Pt .

Table (3.7): Photo electrochemical parameters of the DSSCs, (A) TiO_2(degussa)/Pt , (B) TiO_2(degussa),0.01CNTs/Pt, (C) TiO_2(degussa), 0.025CNTs/Pt, (D) TiO_2(degussa),0.05CNTs/Pt .

Types of electrodes	Isc (mA)	Voc (V)	Jmax (mA)	Vmax (V)	Pmax	FF%	η%
A	8.670	0.590	6.490	0.349	2.265	0.443	2.962
B	8.670	0.600	6.500	0.349	2.268	0.439	2.985
C	8.920	0.715	6.950	0.405	2.814	0.441	3.679
D	8.220	0.620	6.100	0.425	2.592	0.508	3.384

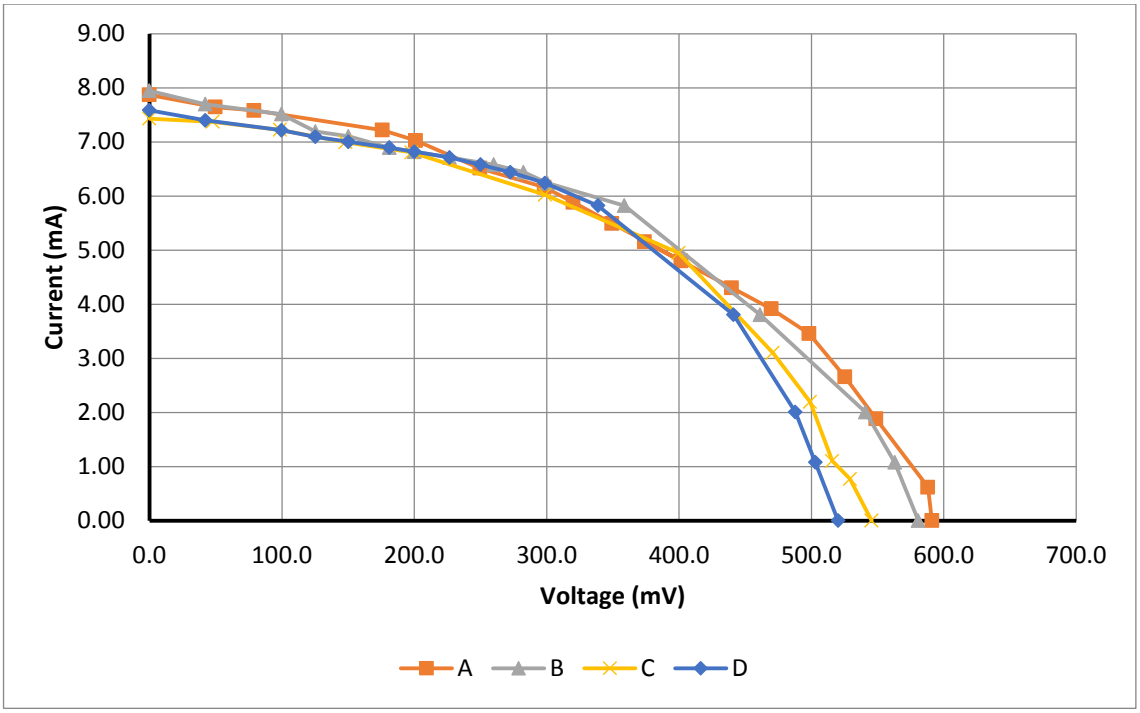

Figure (3.57): I-V characteristics of the fabricated DSSCs, (A) TiO_2(anatase)/Pt , (B) TiO_2(anatase),0.01CNTs/Pt, (C) TiO_2(anatase), 0.025CNTs/Pt (D) TiO_2(anatase), 0.05CNTs/Pt .

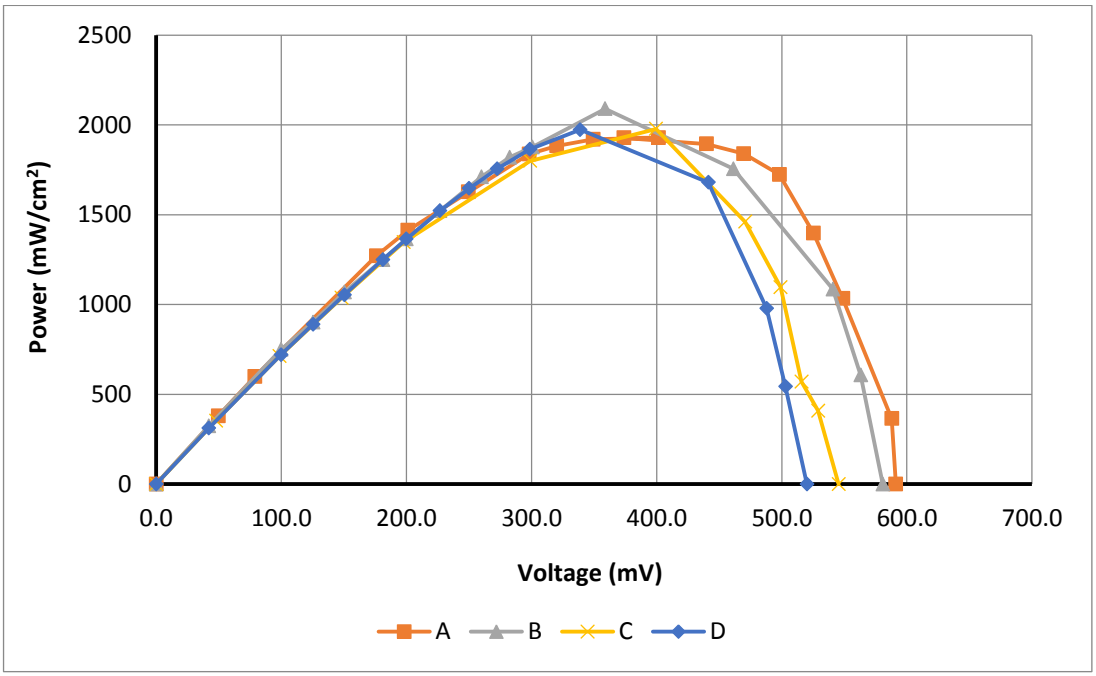

Figure(3.58): P-V characteristics of the fabricated DSSCs, (A) TiO_2(anatase)/Pt , (B) TiO_2(anatase),0.01CNTs/Pt, (C) TiO_2(anatase), 0.025CNTs/Pt, (D) TiO_2(anatase), 0.05CNTs/Pt .

Table (3.8): Photo electrochemical parameters of the DSSCs, (A) TiO_2(anatase)/Pt , (B) TiO_2(anatase),0.01CNTs/Pt, (C) TiO_2(anatase),0.025CNTs/Pt, (D) TiO_2(anatase),0.05CNTs/Pt .

Types of electrodes	Isc (mA)	Voc (V)	Jmax (mA)	Vmax (V)	Pmax	FF%	η%
A	7.870	0.591	5.400	0.374	2.019	0.434	2.640
B	7.950	0.580	5.300	0.400	2.120	0.459	2.766
C	7.430	0.545	5.750	0.345	1.986	0.490	2.595
D	7.590	0.520	5.770	0.350	2.019	0.511	2.640

From figures (3.55) and (3.57) and tables (3.7)and (3.8), it is noticed that when platinum is used as a counter electrode, the efficiency of its cells is higher when the percentages of TiO_2/CNTs composites are higher. This is due to the fact that carbon nanotubes increased the surface area of the composites, thus increasing its absorption capacity, in addition to the high efficiency of platinum as a counter electrode in solar cells. But the increase in carbon nanotubes to a large percentage could affect the transparency of the solar cell and thus reduce its efficiency. That is why very low percentages were used. In previous figures, the highest efficiency of the cell reaches 3.679 with TiO_2(degussa), and 0.025CNTs /pt , as well as 2.766 with TiO_2(anatase), and 0.01CNTs/pt , In both cases, the efficiency of the cells decreases with continuous increase in composites containing CNTs whether it contains TiO_2 anatase or degussa .

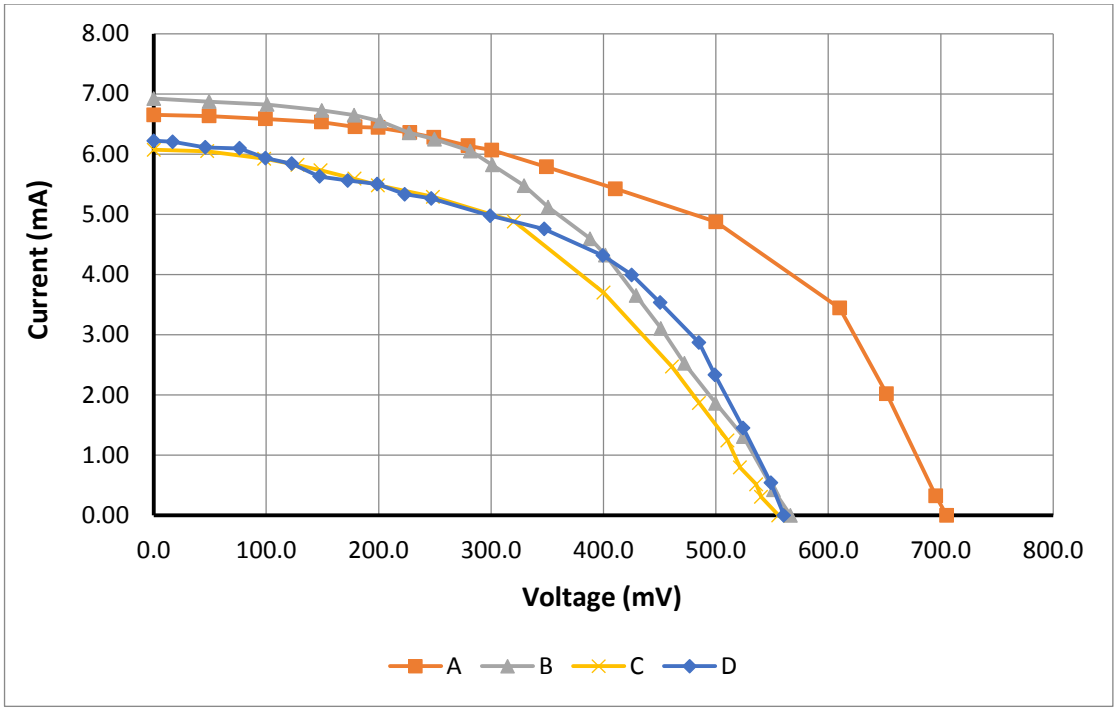

Figure (3.59): I-V characteristics of the fabricated DSSCs, (A) TiO_2(degussa)/CNTs , (B) TiO_2(degussa),0.01CNTs/CNTs,(C) TiO_2(degussa),0.025CNTs/CNTs (D) TiO_2(degussa), 0.05CNTs/CNTs.

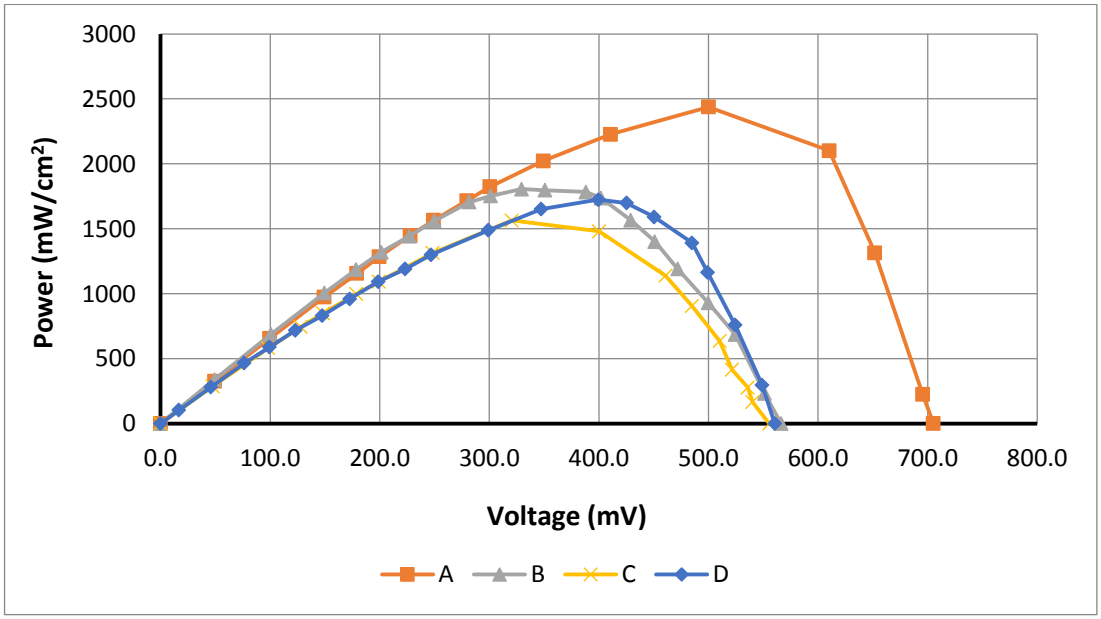

Figure(3.60): P-V characteristics of the fabricated DSSCs, (A) TiO_2(degussa)/CNTs ,(B) TiO_2(degussa),0.01CNTs/CNTs,(C) TiO_2(degussa),0.025CNTs/CNTs,(D) TiO_2(degussa), 0.05CNTs/CNTs.

Table (3.9): Photo electrochemical parameters of the DSSCs, (A) TiO_2(degussa)/CNTs ,(B) TiO_2(degussa), 0.01CNTs/CNTs, (C) TiO_2(degussa),0.025CNTs/CNTs,(D) TiO_2(degussa), 0.05CNTs/CNTs.

Types of electrodes	Isc (mA)	Voc (V)	Jmax (mA)	Vmax (V)	Pmax	FF%	η%
A	6.650	0.705	5.250	0.430	2.257	0.481	2.950
B	6.920	0.566	5.500	0.330	1.815	0.463	2.370
C	6.070	0.555	4.600	0.350	1.610	0.478	2.104
D	6.220	0.560	4.500	0.400	1.800	0.5167	2.350

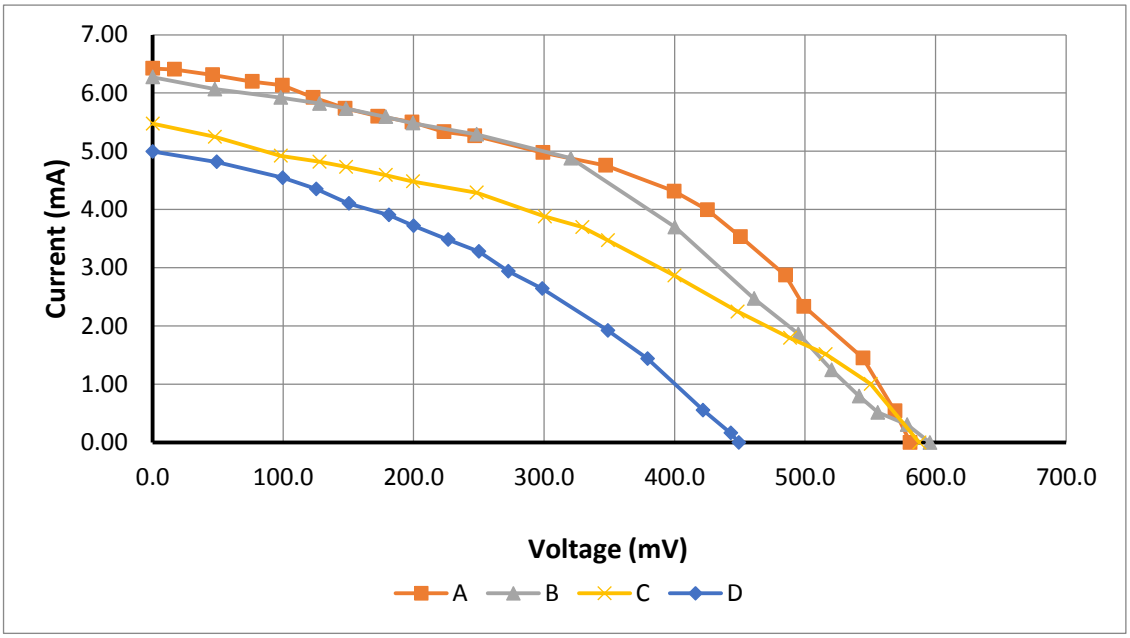

Figure (3.61): I-V characteristics of the fabricated DSSCs, (A) TiO_2(anatase)/CNTs , (B) TiO_2(anatase), 0.01CNTs/CNTs, (C) TiO_2(anatase), 0.025CNTs/CNTs (D) TiO_2(anatase), 0.05CNTs/CNTs.

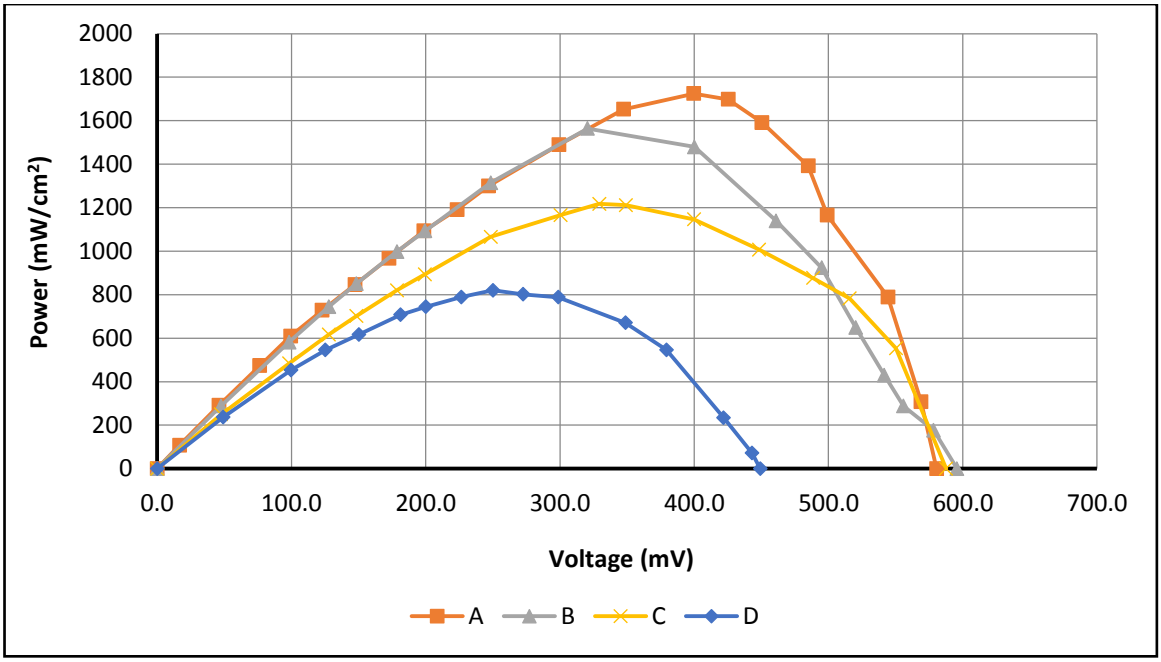

Figure(3.62): P-V characteristics of the fabricated DSSCs, (A) TiO_2(anatase)/CNTs , (B) TiO_2(anatase),0.01CNTs/CNTs, (C) TiO_2(anatase), 0.025CNTs/CNTs, (D) TiO_2(anatase),0.05CNTs/CNTs .

Table (3.10): Photo electrochemical parameters of the DSSCs, (A) TiO_2(anatase)/CNTs ,(B) TiO_2(anatase),0.01CNTs/CNTs,(C) TiO_2(anatase), 0.025CNTs/CNTs,(D) TiO_2(anatase),0.05CNTs/CNTs .

Types of electrodes	Isc (mA)	Voc (V)	Jmax (mA)	Vmax (V)	Pmax	FF%	η%
A	6.420	0.580	4.000	0.425	1.700	0.456	2.219
B	6.270	0.595	4.400	0.360	1.584	0.424	2.067
C	5.470	0.587	4.400	0.346	1.311	0.408	1.700
D	5.000	0.449	3.000	0.282	0.844	0.376	1.100

From figures (3.59) and (3.61) and tables (3.9)and (3.10) , it is noted that when CNT is used as a counter electrode, the efficiency of the cell is higher when using only TiO_2 anatase or degussa, and it reaches 2.95 with TiO_2(degussa) as well as 2.219 with TiO_2(anatase), However, when the different percentages of TiO_2 (anatase, degussa)/CNTs composites are used, the efficiency gradually decreases, because the use of carbon nanotubes as a counter electrode and in the installation of composites at the anode would cause the cell to become dark and reduce its ability to absorb light. Therefore, the efficiency reduces with an increase in the proportion of carbon nanotubes in the composite.

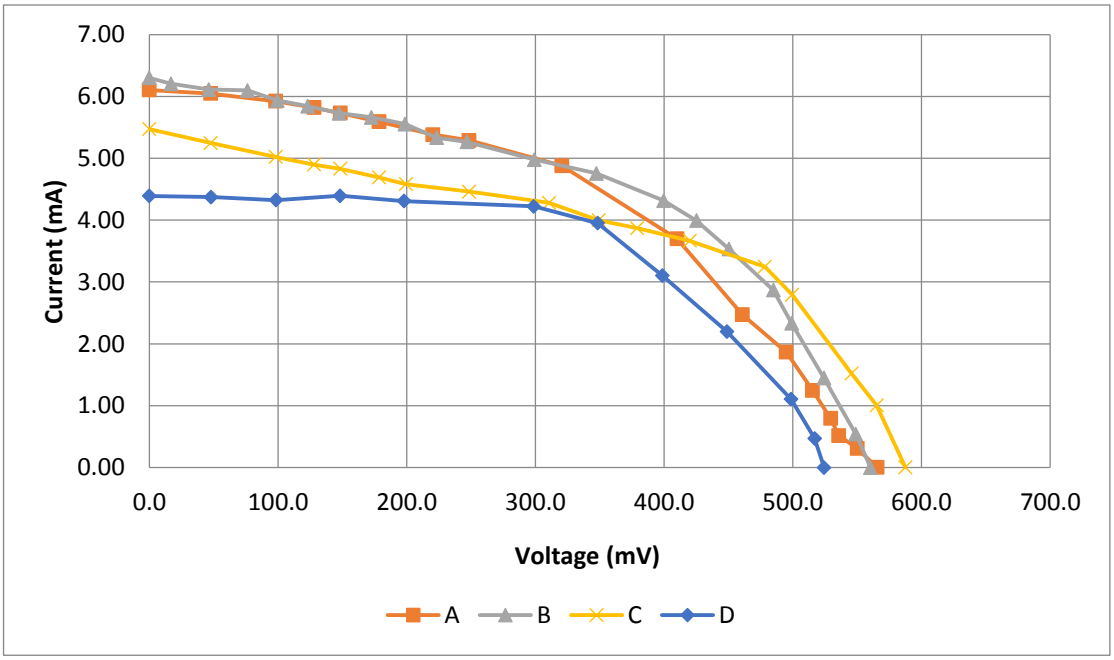

Figure (3.63): I-V characteristics of the fabricated DSSCs, (A) TiO_2(degussa)/graphite , (B) TiO_2(degussa), 0.01CNTs/graphite, (C) TiO_2(degussa), 0.025CNTs/graphite (D) TiO_2(degussa),0.05CNTs /graphite .

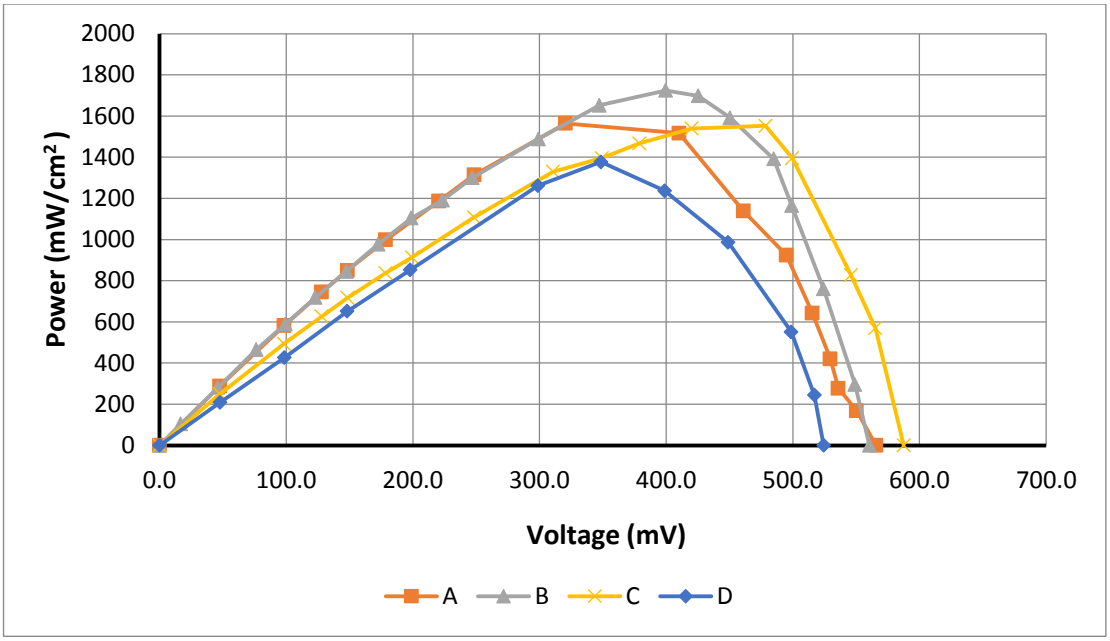

Figure(3.64): P-V characteristics of the fabricated DSSCs, (A) TiO_2(degussa)/graphite ,(B) TiO_2(degussa), 0.01CNTs/graphite,(C) TiO_2(degussa), 0.025CNTs/graphite,(D) TiO_2(degussa), 0.05CNTs /graphite .

Table (3.11): Photo electrochemical parameters of the DSSCs, (A) TiO_2(degussa) /graphite , (B) TiO_2(degussa), 0.01CNTs /graphite, (C) TiO_2(degussa), 0.025CNTs /graphite, (D) TiO_2(degussa), 0.05CNTs /graphite .

Types of electrodes	Isc (mA)	Voc (V)	Jmax (mA)	Vmax (V)	Pmax	FF%	η%
A	6.100	0.565	4.500	0.370	1.665	0.483	2.175
B	6.300	0.560	4.500	0.400	1.800	0.510	2.352
C	5.470	0.587	3.400	0.440	1.496	0.466	1.955
D	4.390	0.524	4.000	0.350	1.400	0.608	1.827

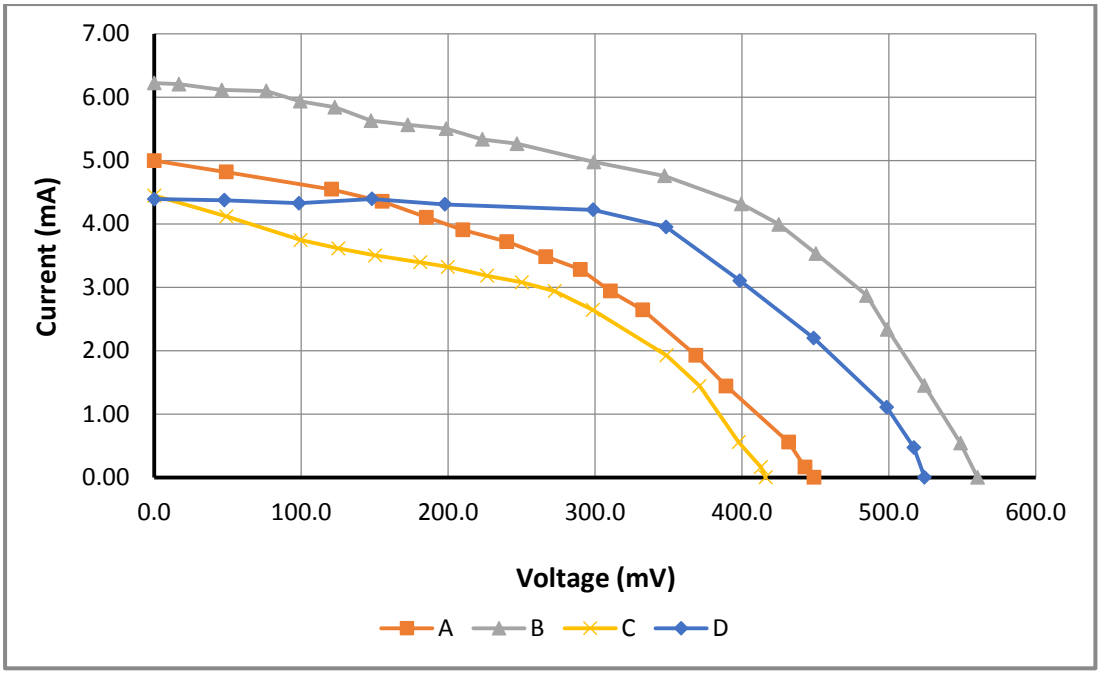

Figure (3.65): I-V characteristics of the fabricated DSSCs, (A) TiO_2(anatase)/graphite , (B) TiO_2(anatase), 0.01CNTs/graphite, (C) TiO_2(anatase), 0.025CNTs /graphit (D) TiO_2(anatase), 0.05CNTs /graphite .

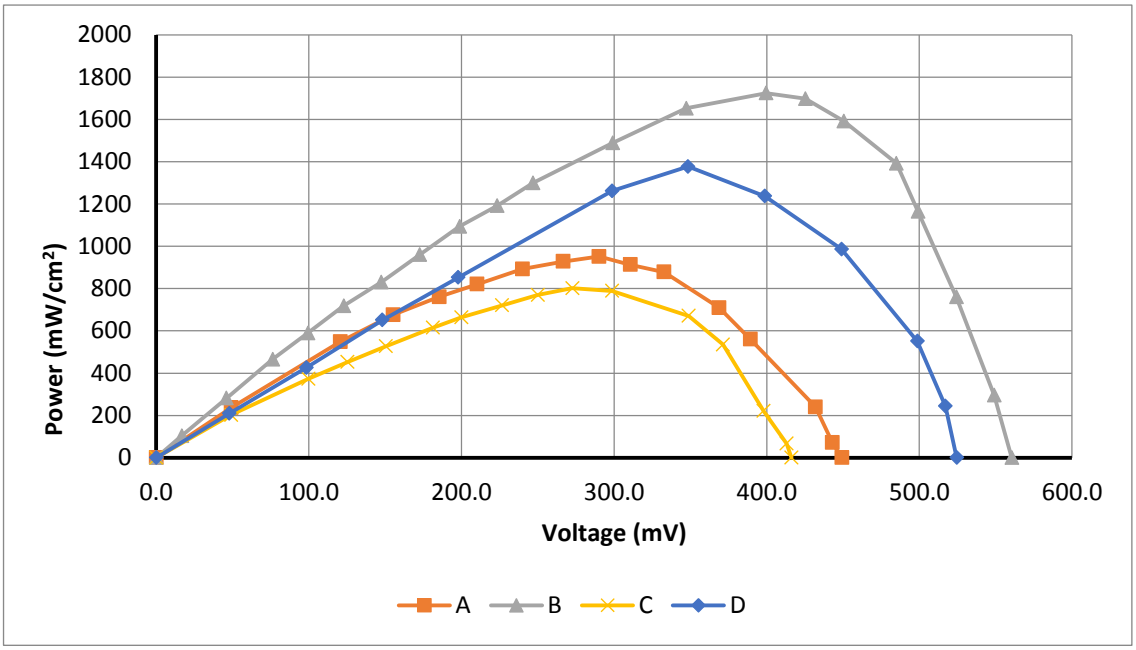

Figure(3.66): P-V characteristics of the fabricated DSSCs, (A) TiO_2(anatase) /graphite , (B) TiO_2(anatase), 0.01CNTs/graphite, (C) TiO_2(anatase), 0.025CNTs/graphite, (D) TiO_2(anatase), 0.05CNTs /graphite.

Table (3.12): electrochemical parameters of the DSSCs, (A) TiO_2(anatase) graphite , (B) TiO_2(anatase), 0.01CNTs /graphite, (C) TiO_2(anatase), 0.025CNTs/ graphit (D) TiO_2(anatase), 0.05CNTs /graphite .

Types of electrodes	Isc (mA)	Voc (V)	Jmax (mA)	Vmax (V)	Pmax	FF%	η%
A	5.000	0.449	3.650	0.260	0.949	0.422	1.240
B	6.220	0.560	4.250	0.405	1.721	0.494	2.249
C	4.450	0.416	3.000	0.290	0.870	0.470	1.137
D	4.390	0.524	4.000	0.340	1.360	1.295	1.770

From figures (3.63) and (3.65) and tables (3.11)and (3.12) , it is observed that when graphite is used as a counter electrode, the efficiency of the cells is high compared to the other electrodes. In addition, its use is advantageous because it is readily available, very cheap, and is easy to prepare, from a pencil or as a candle flame. It gives an excellent efficiency of up to 2.175 with TiO_2(degussa) and 1.240 with TiO_2(anatase). It also performs well with different ratios of composites. The efficiency reaches 2.352 for TiO_2(degussa),0.01CNTs/graphite and 2.249 for TiO_2(anatase),0.01CNTs/graphite. Increasing the proportion of CNT in the composites , reduces the efficiency, probably because the cell becomes very dark, which reduces the efficiency of photocells.

Table (3.13): The best efficiency obtained from the prepared solar cells.

The components of the prepared solar cell	Efficiency %
TiO_2(Degussa),0.025 CNTs/Pt	3.679
TiO_2(anatase),0.01 CNTs/pt	2.766
TiO_2(Degussa)/CNTs	2.95
TiO_2(anatase)/CNTs	2.219
TiO_2(Degussa),0.01 CNTs/Graphite	2.352
TiO_2(anatase), 0.01 CNTs/Graphite	2.249

Conclusions

1- CNTs were synthesized using a new technique (FFD) with a homemade reactor.

2- Because it is safe to use, cheap, and widely available in Iraq, liquefied petroleum gas (LPG) is a useful source for synthesizing CNTs. Liquefied petroleum gas was employed as both an energy source (no need for electricity) and a carbon source.

3- According to XRD and Raman results, the produced CNTs have properties similar to those of purchased MWCNTs.

4- Scanning electron microscopy data showed that the synthesized CNTs particles were dispersed homogenously with an apparent agglomeration of the TiO_2 particles.

5- It is concluded from the obtained data that the type of electrode in the same dye has a very important role in improving the efficiency of the solar cell.

6-TiO_2(degussa) and TiO_2(degussa)/CNTs nanocomposites with pomegranate dye show high efficiency as photoelectric anode in DSSCs with natural dyes.

7- CNTs is cheaper than Pt and has high efficiency, which make it a very attractive choice for use as counter electrode in DSSCs.

8- Fabrication of dye sensitized solar cell from synthesized materials gives high efficiency in compared with other cells that using natural dyes and TiO_2 alone as working electrode.

Recommendations for Future Works

1- Preparation of additional semiconductors and a counter electrode for use in solar cells, with the goal of determining the efficiency of the cells.

2- Other natural dyes such as red cabbage and spinach dyes can be used, as well as dyes that are more efficient.

3- Different electrolytes, as well as various colors, are widely available in the market and can be employed.

4- Trying a new strategy for the synthesis of nanocomposite catalysts with simple conditions.

References

[1] Sudha, P. N., Sangeetha, K., Vijayalakshmi, K., & Barhoum, A. (2018). Nanomaterials history, classification, unique properties, production and market. In *Emerging applications of nanoparticles and architecture nanostructures* (pp. 341-384). Elsevier.

[2] Taniguchi, N. (1974). On the basic concept of nanotechnology. *Proceeding of the ICPE*.

[3] Varghese, R. J., Parani, S., Thomas, S., Oluwafemi, O. S., & Wu, J. (2019). Introduction to nanomaterials: synthesis and applications. In *Nanomaterials for solar cell applications* (pp. 75-95). Elsevier.

[4] Borm, P. J., Robbins, D., Haubold, S., Kuhlbusch, T., Fissan, H., Donaldson, K. Schins, R., Stone, V., Kreyling, W., Lademann, J., Krutmann, J., Warheit, D.,& Oberdorster, E. (2006). The potential risks of nanomaterials: a review carried out for ECETOC. *Particle and fibre toxicology*, *3*(1), 1-35.

[5] Koch, C. C., & Brenner, D. W. (2018). Bulk nanostructured materials. In *Handbook of Nanoscience, Engineering, and Technology* (pp. 706-735). CRC Press.

[6] Panda, P. K., Grigoriev, A., Mishra, Y. K., & Ahuja, R. (2020). Progress in supercapacitors: roles of two dimensional nanotubular materials. *Nanoscale Advances*, *2*(1), 70-108.

[7] Thangadurai, T. D., Manjubaashini, N., Thomas, S., & Maria, H. J. (2020). *Nanostructured materials* (Vol. 210). Cham, Switzerland: Springer International Publishing.

[8] Levchenko, V., Mamunya, Y., Boiteux, G., Lebovka, M., Alcouffe, P., Seytre, G., & Lebedev, E. (2011). Influence of organo-clay on electrical and mechanical properties of PP/MWCNT/OC nanocomposites. *European Polymer Journal*, *47*(7), 1351-1360.

[9] Patel, K. D., Singh, R. K., & Kim, H. W. (2019). Carbon-based nanomaterials as an emerging platform for theranostics. *Materials Horizons*, *6*(3), 434-469.

[10] Ghasempour, R., & Narei, H. (2018). CNT basics and characteristics. In *Carbon nanotube-reinforced polymers* (pp. 1-24). Elsevier.

[11] Asadian, E., Ghalkhani, M., & Shahrokhian, S. (2019). Electrochemical sensing based on carbon nanoparticles: A review. *Sensors and Actuators B: Chemical*, *293*, 183-209.

[12] Yuan, X., Zhang, X., Sun, L., Wei,Y., & Wei, X. (2019). Cellular Toxicity and Immunological Effects of Carbon-based Nanomaterials . *Particle and Fibre Toxicology , 16*(18),2-27 .

[13] Liang, R., Wei, M., Evans, D. G., & Duan, X. (2014). Inorganic nanomaterials for bioimaging, targeted drug delivery and therapeutics. *Chemical Communications*, *50*(91), 14071-14081.

[14] Valero, E. L. (Ed.). (2019). Advanced Nanomaterials for Inexpensive Gas Microsensors: Synthesis, Integration and Applications.Elsevier, Amsterdam, Netherlands.

[15] Chu, H., Wei, L., Cui, R., Wang, J., & Li, Y. (2010). Carbon nanotubes combined with inorganic nanomaterials: Preparations and applications. *Coordination Chemistry Reviews*, *254*(9-10), 1117-1134.

[16] Guo, L., He, N., Zhao, Y., Liu, T., & Deng, Y. (2020). Autophagy modulated by inorganic nanomaterials. *Theranostics*, *10*(7), 3206.

[17] Allouche, J. (2013). Synthesis of organic and bioorganic nanoparticles: an overview of the preparation methods. *Nanomaterials: a danger or a promise?*, 27-74.

[18] Kumar, R., Aadil, K. R., Ranjan, S., & Kumar, V. B. (2020). Advances in nanotechnology and nanomaterials based strategies for neural tissue engineering. *Journal of Drug Delivery Science and Technology*, *57*, 101617.

[19] Johnson, T. History of composites. The evolution of lightweight composite materials. 2018.

[20] Roy, R., Roy, R. A., & Roy, D. M. (1986). Alternative perspectives on "quasi-crystallinity": non-uniformity and nanocomposites. *Materials Letters*, *4*(8-9), 323-328.

[21] Choa, Y. H., Yang, J. K., Kim, B. H., Jeong, Y. K., Lee, J. S., Nakayama, T., Sekino, T.,& Niihara, K. (2003). Preparation and characterization of metal/ceramic nanoporous nanocomposite powders. *Journal of Magnetism and Magnetic Materials*, *266*(1-2), 12-19.

[22] Del Canto, E., Flavin, K., Natali, M., Perova, T., & Giordani, S. (2010). Functionalization of single-walled carbon nanotubes with optically switchable spiropyrans. *Carbon*, *48*(10), 2815-2824.

[23] do Céu Teixeira, M., Santini, A., & Souto, E. B. (2017). Delivery of antimicrobials by chitosan-composed therapeutic nanostructures. In *Nanostructures for Antimicrobial Therapy* (pp. 203-222). Elsevier.

[24] Das, R. N., Lin, H. T., Lauffer, J. M., & Markovich, V. R. (2011). Printable electronics: Towards materials development and device fabrication. *Circuit World*, *37*(1), 38-45.

[25] Ahmadpour, A., Shahsavand, A.,& Shahverdi, M. R. (2003). Current Application of Nanotechnology in Environment, Proceedings of the 4th Biennial Conference of Environmental Specialists Association, Tehran, February 2003 .

[26] Gopakumar, D. A., Pai, A. R., Pasquini, D., Ben, L. S. Y., HPS, A. K., & Thomas, S. (2019). Nanomaterials—state of art, new challenges, and opportunities. *Nanoscale Materials in Water Purification*, 1-24.

[27] Iijima, S., & Ichihashi, T. (1993). Single-shell carbon nanotubes of 1-nm diameter. *nature*, *363*(6430), 603-605.

[28] Cherukuri, P., Bachilo, S. M., Litovsky, S. H., & Weisman, R. B. (2004). Near-infrared fluorescence microscopy of single-walled carbon nanotubes in phagocytic cells. *Journal of the American Chemical Society*, *126*(48), 15638-15639.

[29] Bethune, D. S., Kiang, C. H., De Vries, M. S., Gorman, G., Savoy, R., Vazquez, J., & Beyers, R. (1993). Cobalt-catalysed growth of carbon nanotubes with single-atomic-layer walls. *Nature*, *363*(6430), 605-607.

[30] Doh, J., Park, S. I., Yang, Q., & Raghavan, N. (2019). The effect of carbon nanotube chirality on the electrical conductivity of polymer nanocomposites considering tunneling resistance. *Nanotechnology*, *30*(46), 465701.

[31] Coluci, V. R., Braga, S. F., Legoas, S. B., Galvao, D. S., & Baughman, R. H. (2003). Families of carbon nanotubes: Graphyne-based nanotubes. *Physical Review B*, *68*(3), 035430.

[32] Mukhopadhyay, P., & Gupta, R. K. (Eds.). (2012). *Graphite, Graphene, and their polymer nanocomposites*. CRC press.

[33] Yu, M. F., Yakobson, B. I., & Ruoff, R. S.(2000).Controlled sliding and pullout of nested shells in individual multiwalled carbon nanotubes. *Journal of Physical Chemistry B, 104*(37) , 8764-8767 .

[34] Yadav, A. R., & Mohite, S. K. (2020). Carbon nanotubes as an effective solution for cancer therapy. *Research Journal of Pharmaceutical Dosage Forms and Technology*, *12*(4), 301-307.

[35] Momohjimoh, I., Nouari, S., Hussein, M. A., Laoui, T., & Al-Aqeeli, N. (2019). Thermal behavior of spark plasma sintered alumina-based nanocomposites. *Arabian Journal for Science and Engineering*, *44*(6), 6013-6028.

[36] Venkataraman, A., Amadi, E. V., Chen, Y., & Papadopoulos, C. (2019). Carbon nanotube assembly and integration for applications. *Nanoscale research letters*, *14*(1), 1-47.

[37] Yang, F., Wang, M., Zhang, D., Yang, J., Zheng, M., & Li, Y. (2020). Chirality pure carbon nanotubes: Growth, sorting, and characterization. *Chemical reviews*, *120*(5), 2693-2758.

[38] Zhang, B., Chen, Q., Tang, H., Xie, Q., Ma, M., Tan, L., Zhang,Y.,& Yao, S. (2010). Characterization of and biomolecule immobilization on the

biocompatible multi-walled carbon nanotubes generated by functionalization with polyamidoamine dendrimers. *Colloids and Surfaces B: Biointerfaces*, *80*(1), 18-25.

[39] Saether, E., Frankland, S. J. V., & Pipes, R. B. (2003). Transverse mechanical properties of single-walled carbon nanotube crystals. Part I: determination of elastic moduli. *Composites Science and Technology*, *63*(11), 1543-1550.

[40] Mazari, S. A., Ali, E., Abro, R., Khan, F. S. A., Ahmed, I., Ahmed, M., & Shah, A. (2021). Nanomaterials: Applications, waste-handling, environmental toxicities, and future challenges–A review. *Journal of Environmental Chemical Engineering*, *9*(2), 105028.

[41] Harito, C., Bavykin, D. V., Yuliarto, B., Dipojono, H. K., & Walsh, F. C. (2019). Polymer nanocomposites having a high filler content: synthesis, structures, properties, and applications. *Nanoscale*, *11*(11), 4653-4682.

[42] Wang, X., Li, Q., Xie, J., Jin, Z., Wang, J., Li, Y., Jiang, K.,& Fan, S. (2009). Fabrication of ultralong and electrically uniform single-walled carbon nanotubes on clean substrates. *Nano letters*, *9*(9), 3137-3141.

[43] Qian, C., Qi, H., Gao, B., Cheng, Y., Qiu, Q., Qin, L. C., Zhou, O.,& Liu, J. (2006). Fabrication of small diameter few-walled carbon nanotubes with enhanced field emission property. *Journal of nanoscience and nanotechnology*, *6*(5), 1346-1349.

[44] Iijima, S. (1991). Helical microtubules of graphitic carbon. *nature*, *354*(6348), 56-58.

[45] Ajayan, P.M., Schadler, L.S., & Braun, P.V. (2004). Bulk metal and ceramics nanocomposites. Nanocomposite Science and Technology, Wiley-VCH Verlag GmbH & Co., 1.

[46] Rathinavel, S., Priyadharshini, K., & Panda, D. (2021). A review on carbon nanotube: An overview of synthesis, properties, functionalization, characterization, and the application. *Materials Science and Engineering: B*, *268*, 115095.

[47] Venkataraman, A., Amadi, E. V., Chen, Y., & Papadopoulos, C. (2019). Carbon nanotube assembly and integration for applications. *Nanoscale research letters*, *14*(1), 1-47.

[48] Pant, M., Singh, R., Negi, P., Tiwari, K., & Singh, Y. (2021). A comprehensive review on carbon nano-tube synthesis using chemical vapor deposition. *Materials Today: Proceedings*, *46*, 11250-11253.

[49] Pareek, A., Dom, R., Gupta, J., Chandran, J., Adepu, V., & Borse, P. H. (2020). Insights into renewable hydrogen energy: Recent advances and prospects. *Materials Science for Energy Technologies*, *3*, 319-327.

[50] Eatemadi, A., Daraee, H., Karimkhanloo, H., Kouhi, M., Zarghami, N., Akbarzadeh, A., Abasi, M., Hanifehpour, Y.,& Joo, S. W. (2014). Carbon nanotubes: properties, synthesis, purification, and medical applications. *Nanoscale research letters*, *9*(1), 1-13.

[51] Venkataraman, A., Amadi, E. V., Chen, Y., & Papadopoulos, C. (2019). Carbon nanotube assembly and integration for applications. *Nanoscale research letters*, *14*(1), 1-47.

[52] Rafique, M. M. A., & Iqbal, J. (2011). Production of carbon nanotubes by different routes-a review. *Journal of encapsulation and adsorption sciences*, *1*(02), 29.

[53] Ren, Z. F. (1999). Huang; DZ Wang; JG Wen; JW Xu; JH Wang; LE Calvet; J. Chen; JF Klemic; MA Reed. *Applied Physics Letters*, *75*, 8.

[54] Abbasi, E., Aval, S. F., Akbarzadeh, A., Milani, M., Nasrabadi, H. T., Joo, S. W., Hanifehpour, Y., Nejati-Koshki,K.,& Pashaei-Asl, R. (2014). Dendrimers: synthesis, applications, and properties. *Nanoscale research letters*, *9*(1), 1-10.

[55] Jagadeesan, A. K., Thangavelu, K., & Dhananjeyan, V. (2020). Carbon Nanotubes: Synthesis, Properties and Applications. *21st Century Surface Science*, 27.

[56] Sarangdevot, K., & Sonigara, B. S. (2015). The wondrous world of carbon nanotubes: Structure, synthesis, properties and applications. *Journal of Chemical and Pharmaceutical Research*, *7*(6), 916-933.

[57] Rathinavel, S., Priyadharshini, K., & Panda, D. (2021). A review on carbon nanotube: An overview of synthesis, properties, functionalization, characterization, and the application. *Materials Science and Engineering: B*, *268*, 115095.

[58] Wang, X. D., Vinodgopal, K., & Dai, G. P. (2019). Synthesis of carbon nanotubes by catalytic chemical vapor deposition. *Perspective of Carbon Nanotubes*, 1-19.

[59] Vander Wal, R. L., Berger, G. M., & Ticich, T. M. (2003). Carbon nanotube synthesis in a flame using laser ablation for in situ catalyst generation. *Applied Physics A*, *77*(7), 885-889.

[60] Ebbesen, T. W., & Ajayan, P. M. (1992). Large-scale synthesis of carbon nanotubes. *Nature*, *358*(6383), 220-222.

[61] Dervishi, E., Li, Z., Xu, Y., Saini, V., Biris, A. R., Lupu, D., & Biris, A. S. (2009). Carbon nanotubes: synthesis, properties, and applications. *Particulate Science and Technology*, *27*(2), 107-125.

[62] Sishen**,** X., Wenzhi, L., W, Zhengwei, P., Baohe, C., Lianfeng ,S.(2000). Carbon nanotube arrays. Materials Science and Engineering: A, 286(11), 11-15.

[63] Mubarak, N.M., Abdullah, E.C., Jayakumar, N.S., & Sahu, J.N. (2014). An overview on methods for the production of carbon nanotubes. *Journal of Industrial and Engineering Chemistry*, *20*, 1186-1197.

[64] Wong, E. W., Sheehan, P. E., & Lieber, C. M. (1997). Nanobeam mechanics: elasticity, strength, and toughness of nanorods and nanotubes. *science*, *277*(5334), 1971-1975.

[65] Hammadi, A. H., Jasim, A. M., Abdulrazzak, F. H., Al-Sammarraie, A., Cherifi, Y., Boukherroub, R., & Hussein, F. H. (2020). Purification for

carbon nanotubes synthesized by flame fragments deposition via hydrogen peroxide and acetone. *Materials*, *13*(10), 2342.

[66] Hammadi, A. H., Abdulrazzak, F. H., Atiyah, A. J., & Hussein, F. H. (2017). Synthesis of Carbon Nano tubes by Flame Fragments Deposition of Liquefied Petroleum Gas. *Org & Med Chem IJ*, *29*(12), 2804-2808.

[67] Ebbesen, T. W., Lezec, H. J., Hiura, H., Bennett, J. W., Ghaemi, H. F., & Thio, T. (1996). Electrical conductivity of individual carbon nanotubes. *Nature*, *382*(6586), 54-56.

[68] Treacy, M. J., Ebbesen, T. W., & Gibson, J. M. (1996). Exceptionally high Young's modulus observed for individual carbon nanotubes. *nature*, *381*(6584), 678-680.

[69] Jin, F. L., & Park, S. J. (2013). Recent advances in carbon-nanotube-based epoxy composites. *Carbon letters*, *14*(1), 1-13.

[70] Barnes, T. M., Bergeson, J. D., Tenent, R. C., Larsen, B. A., Teeter, G., Jones, K. M., Blackburn, J.L., & van de Lagemaat, J. (2010). Carbon nanotube network electrodes enabling efficient organic solar cells without a hole transport layer. *Applied Physics Letters*, *96*(24), 118.

[71] Saito, R., Fujita, M., Dresselhaus, G., & Dresselhaus, U. M. (1992). Electronic structure of chiral graphene tubules. *Applied physics letters*, *60*(18), 2204-2206.

[72] del Carmen Camacho, M., Galao, O., Baeza, F. J., Zornoza, E., & Garcés, P. (2014). Mechanical properties and durability of CNT cement composites. *Materials*, *7*(3), 1640-1651.

[73] Cesano, F., Uddin, M. J., Lozano, K., Zanetti, M., & Scarano, D. (2020). All-carbon conductors for electronic and electrical wiring applications. *Frontiers in Materials*, *7*, 219.

[74] Dai, H., Wong, E. W., & Lieber, C. M. (1996). Probing electrical transport in nanomaterials: conductivity of individual carbon nanotubes. *Science*, *272*(5261), 523-526.

[75] Chandra, B., Bhattacharjee, J., Purewal, M., Son, Y. W., Wu, Y., Huang, M., Yan, H., Heinz ,TF., Kim, P., Neaton, JB.,& Hone, J. (2009). Molecular-scale quantum dots from carbon nanotube heterojunctions. *Nano letters*, *9*(4), 1544-1548.

[76] Avouris, P. (2002). Molecular electronics with carbon nanotubes. *Accounts of chemical research*, *35*(12), 1026-1034.

[77] Rao, C. N. R., Govindaraj, A., Gundiah, G., & Vivekchand, S. R. C. (2004). Nanotubes and nanowires. *Chemical engineering science*, *59*(22-23), 4665-4671.

[78] Hahm, M. G., Hashim, D. P., Vajtai, R., & Ajayan, P. M. (2011). A review: controlled synthesis of vertically aligned carbon nanotubes. *Carbon letters*, *12*(4), 185-193.

[79] Ebbesen, T. W., Lezec, H. J., Hiura, H., Bennett, J. W., Ghaemi, H. F., & Thio, T. (1996). Electrical conductivity of individual carbon nanotubes. *Nature*, *382*(6586), 54-56.

[80] Hone, J., Llaguno, M. C., Nemes, N. M., Johnson, A. T., Fischer, J. E., Walters, D. A., & Smalley, R. E. (2000). Electrical and thermal transport properties of magnetically aligned single wall carbon nanotube films. *Applied physics letters*, *77*(5), 666-668.

[81] Tans, S. J., Devoret, M. H., Dai, H., Thess, A., Smalley, R. E., Geerligs, L. J., & Dekker, C. (1997). Individual single-wall carbon nanotubes as quantum wires. *Nature*, *386*(6624), 474-477.

[82] Delaney, P., Di Ventra, M., & Pantelides, S. T. (1999). Quantized conductance of multiwalled carbon nanotubes. *Applied Physics Letters*, *75*(24), 3787-3789.

[83] Bandaru, P. R., Daraio, C., Jin, S., & Rao, A. M. (2005). Novel electrical switching behaviour and logic in carbon nanotube Y-junctions. *Nature materials*, *4*(9), 663-666.

[84] Cheng, Y., & Zhou, O. (2003). Electron field emission from carbon nanotubes. *Comptes Rendus Physique*, *4*(9), 1021-1033.

[85] Modi, A., Koratkar, N., Lass, E., Wei, B., & Ajayan, P. M. (2003). Miniaturized gas ionization sensors using carbon nanotubes. *Nature*, *424*(6945), 171-174.

[86] Yue, G. Z., Qiu, Q., Gao, B., Cheng, Y., Zhang, J., Shimoda, H., Chang,S., Lu, JP.,& Zhou, O. (2002). Generation of continuous and pulsed diagnostic imaging x-ray radiation using a carbon-nanotube-based field-emission cathode. *Applied Physics Letters*, *81*(2), 355-357.

[87] Ruoff, R. S., & Lorents, D. C. (1995). Mechanical and thermal properties of carbon nanotubes. *carbon*, *33*(7), 925-930.

[88] Yu, C., Shi, L., Yao, Z., Li, D., & Majumdar, A. (2005). Thermal conductance and thermopower of an individual single-wall carbon nanotube. *Nano letters*, *5*(9), 1842-1846.

[89] Kim, P., Shi, L., Majumdar, A., & McEuen, P. L. (2001). Thermal transport measurements of individual multiwalled nanotubes. *Physical review letters*, *87*(21), 215502.

[90] Ajayan, P. M., Ebbesen, T. W., Ichihashi, T., Iijima, S., Tanigaki, K., & Hiura, H. (1993). Opening carbon nanotubes with oxygen and implications for filling. *Nature*, *362*(6420), 522-525.

[91] Park, T. J., Banerjee, S., Hemraj-Benny, T., & Wong, S. S. (2006). Purification strategies and purity visualization techniques for single-walled carbon nanotubes. *Journal of Materials Chemistry*, *16*(2), 141-154.

[92] Haddon, R. C., Sippel, J., Rinzler, A. G., & Papadimitrakopoulos, F. (2004). Purification and separation of carbon nanotubes. *Mrs Bulletin*, *29*(4), 252-259.

[93] Patole, S. P., Alegaonkar, P. S., Lee, H. C., & Yoo, J. B. (2008). Optimization of water assisted chemical vapor deposition parameters for super growth of carbon nanotubes. *Carbon*, *46*(14), 1987-1993.

[94] Hou,P.X., Liu, C., Cheng, H.M. (2008). Purification of carbon nanotubes. *Carbon ,46*(15), 2003–2025.

[95] Salernitano, E., Giorgi, L., Makris, T. D., Giorgi, R., Lisi, N., Contini, V., & Falconieri, M. (2007). Purification of MWCNTs grown on a nanosized unsupported Fe-based powder catalyst. *Diamond and related materials*, *16*(8), 1565-1570.

[96] Zhao, N., He, C., Li, J., Jiang, Z., & Li, Y.(2006). Study on purification and tip-opening of CNTs fabricated by CVD. *Materials Research Bulletin,41*(12), 2204-2209.

[97] Moon, J. M., An, K. H., Lee, Y. H., Park, Y. S., Bae, D. J., & Park, G. S. (2001). High-yield purification process of singlewalled carbon nanotubes. *The Journal of physical chemistry B*, *105*(24), 5677-5681.

[98] Hernadi, K., Siska, A., Thien-Nga, L., Forro, L., & Kiricsi, I. (2001). Reactivity of different kinds of carbon during oxidative purification of catalytically prepared carbon nanotubes . *Solid State Ionics, 141–142,* 203-209.

[99] Delpeux, S., Szostak, K., Frackowiak, E., & Beguin, F. (2005). An efficient two-step process for producing opened multi-walled carbon nanotubes of high purity . *Chemical Physics Letters, 404*(374).

[100] Colomer, J. F., Piedigrosso, P., Fonseca, A., & Nagy, J. B. (1999). Different purification methods of carbon nanotubes produced by catalytic synthesis. *Synthetic Metals*, *103*(1-3), 2482-2483.

[101] Raymundo-Pinero, E., Cacciaguerra, T., Simonand, P., & Beguin, F. (2005). A single step process for the simultaneous purification and opening of multiwalled carbon nanotubes . *Chemical Physics Letters, 412,* 184-189.

[102] Rasheed, A., Howe, J. Y., Dadmun, M. D., & Britt, P. F.(2007). The efficiency of the oxidation of carbon nanofibers with various oxidizing agents. *Carbon, 45*(5), 1072-1080.

[103] Lakshminarayanan, P.V. , Toghiani, H., Pittman, C.U.(2004). Nitric acid oxidation of vapor grown carbon nanofibers . *Carbon, 42,* 2433-2442.

[104] Feng, Y., Zhang, H., Hou, Y., McNicholas, T. P., Yuan, D., Yang, S., Ding, L., Feng, W.,& Liu, J. (2008). Room temperature purification of few-walled carbon nanotubes with high yield. *ACS nano*, *2*(8), 1634-1638.

[105] Chen, R. J., Zhang, Y., Wang, D., & Dai, H. (2001). Noncovalent sidewall functionalization of single-walled carbon nanotubes for protein immobilization. *Journal of the American Chemical Society*, *123*(16), 3838-3839.

[106] Zare, K., Gupta, V. K., Moradi, O., Makhlouf, A. S. H., Sillanpää, M., Nadagouda, M. N., Sadegh ,H., Shahryari-ghoshekandi, R., Pal ,A.,Wang, Z., Tyagi, I.,& Kazemi, M. (2015). A comparative study on the basis of adsorption capacity between CNTs and activated carbon as adsorbents for removal of noxious synthetic dyes: a review. *Journal of nanostructure in chemistry*, *5*(2), 227-236.

[107] Chen, R. J., Zhang, Y., Wang, D., & Dai, H. (2001). Noncovalent sidewall functionalization of single-walled carbon nanotubes for protein immobilization. *Journal of the American Chemical Society*, *123*(16), 3838-3839.

[108] Shi Kam, N. W., Jessop, T. C., Wender, P. A., & Dai, H. (2004). Nanotube molecular transporters: internalization of carbon nanotube− protein conjugates into mammalian cells. *Journal of the american chemical society*, *126*(22), 6850-6851.

[109] Yim, T. J., Liu, J., Lu, Y., Kane, R. S., & Dordick, J. S. (2005). Highly active and stable DNAzyme− carbon nanotube hybrids. *Journal of the American Chemical Society*, *127*(35), 12200-12201.

[110] Kukovecz, A., Kramberger, C., Holzinger, M., Kuzmany, H., Schalko, J., Mannsberger, M., & Hirsch, A. (2002). On the stacking behavior of functionalized single-wall carbon nanotubes. *The Journal of Physical Chemistry B*, *106*(25), 6374-6380.

[111] Chen, J., Rao, A. M., Lyuksyutov, S., Itkis, M. E., Hamon, M. A., Hu, H., Cohn ,R.W., Eklund, P.C., Colbert, D.T., Smalley, R.E.,& Haddon, R. C.

(2001). Dissolution of full-length single-walled carbon nanotubes. *The Journal of Physical Chemistry B*, *105*(13), 2525-2528.

[112] Niyogi, S., Hamon, M. A., Hu, H., Zhao, B., Bhowmik, P., Sen, R., Itkis, M.E.,& Haddon, R. C. (2002). Chemistry of single-walled carbon nanotubes. *Accounts of Chemical Research*, *35*(12), 1105-1113.

[113] Hiura, H., Ebbesen, T. W., & Tanigaki, K. (1995). Opening and purification of carbon nanotubes in high yields. *Advanced Materials*, *7*(3), 275-276.

[114] Banerjee, S., Hemraj-Benny, T., & Wong, S. S. (2005). Covalent surface chemistry of single-walled carbon nanotubes. *Advanced Materials*, *17*(1), 17-29.

[115] Ajayan, P. M. (1993). Capillarity-induced filling of carbon nanotubes. *Nature*, *361*(6410), 333-334.

[116] Chen, J., Hamon, M. A., Hu, H., Chen, Y., Rao, A. M., Eklund, P. C., & Haddon, R. C. (1998). Solution properties of single-walled carbon nanotubes. *Science*, *282*(5386), 95-98.

[117] Gupta, V. K., Sadegh, H., Yari, M., Shahryari, G. R., Maazinejad, B., & Chahardori, M. (2015). Removal of ammonium ions from wastewater a short review in development of efficient methods.

[118] Monthioux, M., Smith, B. W., Burteaux, B., Claye, A., Fischer, J. E., & Luzzi, D. E. (2001). Sensitivity of single-wall carbon nanotubes to chemical processing: an electron microscopy investigation. *Carbon*, *39*(8), 1251-1272.

[119] Xie, Y., Liu, T., Chu, Z., & Jin, W. (2021). Recent advances in electrochemical enzymatic biosensors based on regular nanostructured materials. *Journal of Electroanalytical Chemistry*, *893*, 115328.

[120] Srinivasreddy, R. K., & Kadeppagari, R. K. (2021). Functionalized Carbon Nanotubes for Ammonia Sensors. *Environmental Applications of Carbon Nanomaterials-Based Devices*, 251-263.

[121] Chan, S. H. S., Yeong Wu, T., Juan, J. C., & Teh, C. Y. (2011). Recent developments of metal oxide semiconductors as photocatalysts in advanced oxidation processes (AOPs) for treatment of dye waste-water. *Journal of Chemical Technology & Biotechnology*, *86*(9), 1130-1158.

[122] Domaradzki J., Borkowska A., Kaczmarek D., & Prociów E.L. (2005). Properties of transparent oxide thin films prepared by plasma deposition. *Optica Applicata* , *35* (3), 425-430 .

[123] Borkowska, A., Domaradzki, J.,& Kaczmarek, D.(2007). Influence of Eu dopant on optical properties of TiO_2 thin films fabricated by low pressure hot target reactive sputtering. *Optica Applicata* , *37* , 117-122.

[124] Mazur, M., Wojcieszak, D., Domaradzki, J., Kaczmarek, D., Song, S., & Placido, F. (2013). TiO2/SiO2 multilayer as an antireflective and protective coating deposited by microwave assisted magnetron sputtering. *Opto-Electronics Review*, *21*(2), 233-238.

[125] Fazli, F. I. M., Ahmad, M. K., Soon, C. F., Nafarizal, N., Suriani, A. B., Mohamed, A., Mamat, M.H., Malek, M.F., Shimomura, M.,& Murakami, K. (2017). Dye-sensitized solar Cell using pure anatase TiO_2 annealed at different temperatures. *Optik*, *140*, 1063-1068.

[126] Li, W., Ni, C., Lin, H., Huang, C. P., & Shah, S. I. (2004). Size dependence of thermal stability of TiO_2 nanoparticles. *Journal of Applied Physics*, *96*(11), 6663-6668.

[127] Bai, Y., Mora-Sero, I., De Angelis, F., Bisquert, J., & Wang, P. (2014). Titanium dioxide nanomaterials for photovoltaic applications. *Chemical reviews*, *114*(19), 10095-10130.

[128] Hossain, M. K., Pervez, M. F., Mia, M. N. H., Tayyaba, S., Uddin, M. J., Ahamed, R., Khan, R.A., Hoq, M., Khan, M.A.,& Ahmed, F. (2017). Annealing temperature effect on structural, morphological and optical parameters of mesoporous TiO_2 film photoanode for dye-sensitized solar cell application. *Mater. Sci.*, *35*, 868-877.

[129] Jung, Y. H., Park, K. H., Oh, J. S., Kim, D. H., & Hong, C. K. (2013). Effect of TiO_2 rutile nanorods on the photoelectrodes of dye-sensitized solar cells. *Nanoscale research letters*, *8*(1), 1-6.

[130] Li, G., Richter, C. P., Milot, R. L., Cai, L., Schmuttenmaer, C. A., Crabtree, R. H., Brudvig, G.W.,& Batista, V. S. (2009). Synergistic effect between anatase and rutile TiO_2 nanoparticles in dye-sensitized solar cells. *Dalton Transactions*, (45), 10078-10085.

[131] Zhang, J., Xu, Q., Feng, Z., Li, M., & Li, C. (2008). Importance of the relationship between surface phases and photocatalytic activity of TiO_2. *Angewandte Chemie*, *120*(9), 1790-1793.

[132] Kinsinger, N. M., Dudchenko, A., Wong, A., & Kisailus, D. (2013). Synergistic effect of pH and phase in a nanocrystalline titania photocatalyst. *ACS applied materials & interfaces*, *5*(13), 6247-6254.

[133] Su, R., Bechstein, R., Sø, L., Vang, R. T., Sillassen, M., Esbjornsson, B., Palm, A.,& Besenbacher, F. (2011). How the anatase-to-rutile ratio influences the photoreactivity of TiO_2. *The journal of physical chemistry C*, *115*(49), 24287-24292.

[134] Sun, B., & Smirniotis, P. G. (2003). Interaction of anatase and rutile TiO_2 particles in aqueous photooxidation. *Catalysis Today*, *88*(1-2), 49–59.

[135] Kho, Y. K., Iwase, A., Teoh, W. Y., Mädler, L., Kudo, A., & Amal, R. (2010). Photocatalytic H_2 evolution over TiO_2 nanoparticles. The synergistic effect of anatase and rutile. *The Journal of Physical Chemistry C*, *114*(6), 2821-2829.

[136] Sun, B., Vorontsov, A. V., & Smirniotis, P. G. (2003). Role of platinum deposited on TiO_2 in phenol photocatalytic oxidation. *Langmuir*, *19*(8), 3151-3156.

[137] Hurum, D. C., Agrios, A. G., Gray, K. A., Rajh, T., & Thurnauer, M. C. (2003). Explaining the enhanced photocatalytic activity of Degussa P25 mixed-phase TiO2 using EPR. *The Journal of Physical Chemistry B*, *107*(19), 4545-4549.

[138] Hurum, D. C., Agrios, A. G., Gray, K. A., Rajh, T., & Thurnauer, M. C. (2003). Explaining the enhanced photocatalytic activity of Degussa P25 mixed-phase TiO_2 using EPR. *The Journal of Physical Chemistry B*, *107*(19), 4545-4549.

[139] Amano, F., Nakata, M., Yamamoto, A., & Tanaka, T. (2016). Rutile titanium dioxide prepared by hydrogen reduction of Degussa P25 for highly efficient photocatalytic hydrogen evolution. *Catalysis Science & Technology*, *6*(14), 5693-5699.

[140] Pfeifer, V., Erhart, P., Li, S., Rachut, K., Morasch, J., Brötz, J., Reckers, P., Mayer, T., Rühle, S., Zaban, A., MoraSeró, I., Bisquert, J., Jaegermann, W.,& Klein, A. (2013). Energy band alignment between anatase and rutile TiO_2. *The Journal of Physical Chemistry Letters*, *4*(23), 4182-4187.

[141] Deák, P., Aradi, B., & Frauenheim, T. (2011). Band lineup and charge carrier separation in mixed rutile-anatase systems. *The Journal of Physical Chemistry C*, *115*(8), 3443-3446.

[142] Kang, J., Wu, F., Li, S. S., Xia, J. B., & Li, J. (2012). Calculating band alignment between materials with different structures: the case of anatase and rutile titanium dioxide. *The Journal of Physical Chemistry C*, *116*(39), 20765-20768.

[143] Akhavan, O., Azimirad, R., Safa, S., & Larijani, M. M. (2010). Visible light photo-induced antibacterial activity of CNT–doped TiO_2 thin films with various CNT contents. *Journal of Materials Chemistry*, *20*(35), 7386-7392.

[144] Mahshid, S., Askari, M., & Ghamsari, M. S. (2007). Synthesis of TiO_2 nanoparticles by hydrolysis and peptization of titanium isopropoxide solution. *Journal of Materials Processing Technology*, *189*(1-3), 296-300.

[145] Jang, H. D., & Kim, S.-K. (2001). Controlled Synthesis of Titanium Dioxide Nanoparticles in a Modified Diffusion Flame Reactor. *Materials Research Bulletin*, *36*(3-4), 627-637.

[146] Do Kim, K., & Kim, H. T. (2001). Synthesis of TiO_2 nanoparticles by hydrolysis of TEOT and decrease of particle size using a two-stage mixed method. *Powder technology*, *119*(2-3), 164-172.

[147] Jang, H. D., & Kim, S.-K. (2001). Controlled Synthesis of Titanium Dioxide Nanoparticles in a Modified Diffusion Flame Reactor. *Materials Research Bulletin*, *36*(3-4), 627-637.

[148] Krysiak, E., Wypych-Puszkarz, A., Krysiak, K., Nowaczyk, G., Makrocka-Rydzyk, M., Jurga, S., & Ulanski, J. (2015). Core–shell system based on titanium dioxide with elevated value of dielectric permittivity: Synthesis and characterization. *Synthetic Metals*, *209*, 150-157.

[149] Jasim, K. E. (2011). Dye sensitized solar cells-working principles, challenges and opportunities. *Solar Cells-Dye-Sensitized Devices*, *8*, 172Ā210.

[150] Ajayan, P. M. (1999). Nanotubes from carbon. *Chemical reviews*, *99*(7), 1787-1800.

[151] Piscanec, S., Lazzeri, M., Robertson, J., Ferrari, A. C., & Mauri, F. (2007). Optical phonons in carbon nanotubes: Kohn anomalies, Peierls distortions, and dynamic effects. *Physical Review B*, *75*(3), 035427.

[152] Chen, C. S., Chen, X. H., Yi, B., Liu, T. G., Li, W. H., Xu, L. S.,Yang ,Z., Zhang. H.,& Wang, Y. G. (2006). Zinc oxide nanoparticle decorated multi-walled carbon nanotubes and their optical properties. *Acta Materialia*, *54*(20), 5401-5407.

[153] Usmani, F. A., & Hasan, M. (2010). Carbon nanotube field effect transistors for high performance analog applications: An optimum design approach. *Microelectronics Journal*, *41*(7), 395-402.

[154] Gracia-Espino, E., Sala, G., Pino, F., Halonen, N., Luomahaara, J., Mäklin, J., Tóth, G., Kordás, K., Jantunen, H., Terrones, M., Helistö, Seppä, H.M., Ajayan‖,P.M.,& Vajtai, R. (2010). Electrical transport and field-effect transistors using inkjet-printed SWCNT films having different functional side groups. *ACS nano*, *4*(6), 3318-3324.

[155] Barnes, T. M., Bergeson, J. D., Tenent, R. C., Larsen, B. A., Teeter, G., Jones, K. M., Blackburn J. L.,& van de Lagemaat, J. (2010). Carbon nanotube network electrodes enabling efficient organic solar cells without a hole transport layer. *Applied Physics Letters*, *96*(24), 118.

[156] Wu, H., Wexler, D., Ranjbartoreh, A. R., Liu, H., & Wang, G. (2010). Chemical processing of double-walled carbon nanotubes for enhanced hydrogen storage. *International journal of hydrogen energy*, *35*(12), 6345-6349.

[157] Wang, L., Chen, W., Xu, D., Shim, B. S., Zhu, Y., Sun, F., Liu, L., Peng, C., Jin, Z., Xu, C.,& Kotov, N. A. (2009). Simple, rapid, sensitive, and versatile SWNT− paper sensor for environmental toxin detection competitive with ELISA. *Nano letters*, *9*(12), 4147-4152.

[158] Andrews, R., Jacques, D., Qian, D., & Rantell, T. (2002). Multiwall carbon nanotubes: synthesis and application. *Accounts of chemical research*, *35*(12), 1008-1017.

[159] Schadler, L. S., Giannaris, S. A., & Ajayan, P. M. (1998). Load transfer in carbon nanotube epoxy composites. *Applied physics letters*, *73*(26), 3842-3844.

[160] Georgakilas, V., Gournis, D., Tzitzios, V., Pasquato, L., Guldi, D. M., & Prato, M. (2007). Decorating carbon nanotubes with metal or semiconductor nanoparticles. *Journal of Materials Chemistry*, *17*(26), 2679-2694.

[161] Xiang, R. Y., Lin, Y., & Wai, C. M. (2003). Decorating catalytic palladium nanoparticles on carbon nanotubes in supercritical carbon dioxide. *Chemical Communications*, (5), 642-643.

[162] Qi, J., Benipal, N., Liang, C., & Li, W. (2016). PdAg/CNT catalyzed alcohol oxidation reaction for high-performance anion exchange membrane direct alcohol fuel cell (alcohol= methanol, ethanol, ethylene glycol and glycerol). *Applied Catalysis B: Environmental*, *199*, 494-503.

[163] Yakobson, B. I., Brabec , C. J., & Bernholc, J. (1996). Nanomechanics of Carbon Tubes: Instabilities beyond Linear Response. *Physical Review Letters*, *76*, 2511-2514.

[164] Helland, A., Wick, P., Koehler, A., Schmid, K., & Som, C. (2007). Reviewing the environmental and human health knowledge base of carbon nanotubes. *Environmental health perspectives*, *115*(8), 1125-1131.

[165] Baughman, R. H., Zakhidov, A. A., & De Heer, W. A. (2002). Carbon nanotubes--the route toward applications. *science*, *297*(5582), 787-792.

[166] Zaidi, B. (2018). Introductory chapter: Introduction to photovoltaic effect. *Solar Panels and Photovoltaic Materials*, 1-8.

[167] Wohlgemuth, J. H., & Narayanan, S. (1991, October). Buried contact concentrator solar cells. In *The Conference Record of the Twenty-Second IEEE Photovoltaic Specialists Conference-1991* (pp. 273-277). IEEE.

[168] Fthenakis, V. M. (2004). Life cycle impact analysis of cadmium in CdTe PV production. *Renewable and Sustainable Energy Reviews*, *8*(4), 303-334.

[169] Hutchison, J. L., Kiselev, N. A., Krinichnaya, E. P., Krestinin, A. V., Loutfy, R. O., Morawsky, A. P.,Muradyan, V.E., Obraztsova,E.D., Sloan,J., Terekhov,S.V.,& Zakharov, D. N. (2001). Double-walled carbon nanotubes fabricated by a hydrogen arc discharge method. *Carbon*, *39*(5), 761-770.

[170] Huang, H., Kajiura, H., Tsutsui, S., Murakami, Y., & Ata, M. (2003). High-quality double-walled carbon nanotube super bundles grown in a hydrogen-free atmosphere. *The Journal of Physical Chemistry B*, *107*(34), 8794-8798.

[171] Kim, B. J., Han, S. H., & Park, J. S. (2015). Properties of CNTs coated by PEDOT: PSS films via spin-coating and electrophoretic deposition methods for flexible transparent electrodes. *Surface and Coatings Technology*, *271*, 22-26.

[172] Sun, R., Deng, D., Guo, J., Wu, Q., Guo, J., Shi, M., & Min, J. (2019). Spontaneous open-circuit voltage gain of fully fabricated organic solar cells caused by elimination of interfacial energy disorder. *Energy & Environmental Science*, *12*(8), 2518-2528.

[173] Zaidi, B. (2018). Introductory chapter: Introduction to photovoltaic effect. *Solar Panels and Photovoltaic Materials*, 1-8.

[174] Nogueira, A. F., Longo, C., & De Paoli, M. A. (2004). Polymers in dye sensitized solar cells: overview and perspectives. *Coordination Chemistry Reviews*, *248*(13-14), 1455-1468.

[175] Chen, J. Z., Yan, Y. C., & Lin, K. J. (2010). Effects of Carbon Nanotubes on Dye-Sensitized Solar Cells. *Journal of the Chinese Chemical Society*, *57*(5B), 1180-1184.

[176] Chapin, D. M., Fuller, C. S., & Pearson, G. L. (1954). A new silicon p-n junction photocell for converting solar radiation into electrical power. *Journal of Applied Physics*, *25*(5), 676-677.

[177] Ongon, T., Daisuke, M., & Masayasu, I. (2011). Carbon Nanotubes Counter Electrode for Dye-Sensitized Solar Cell, *Fujikura Technical Review*.

[178] Jayawardena, K. I., Rozanski, L. J., Mills, C. A., Beliatis, M. J., Nismy, N. A., & Silva, S. R. P. (2013). 'Inorganics-in-Organics': recent developments and outlook for 4G polymer solar cells. *Nanoscale*, *5*(18), 8411-8427.

[179]Gong, J.,Liang, J., & Sumathy, K. (2012). Review on dye-sensitized solar cells (DSSCs): Fundamental concepts and novel materials. *Renewable and Sustainable Energy Reviews*, *16*(8), 5848-5860 .

[180] Baxter, J. B., & Aydil, E. S. (2005). Nanowire-based dye-sensitized solar cells. *Applied physics letters*, *86*(5), 053114.

[181] Mohammed, A. A., Ahmad, A. S. S., & Azeez, W. A. (2015). Fabrication of dye sensitized solar cell based on titanium dioxide (TiO 2). *Advances in Materials Physics and Chemistry*, *5*(09), 361.

[182] O'regan, B., & Grätzel, M. (1991). A low-cost, high-efficiency solar cell based on dye-sensitized colloidal TiO_2 films. *nature*, *353*(6346), 737-740.

[183] Nazeeruddin, M. K., Kay, A., Rodicio, I., Humphry-Baker, R., Müller, E., Liska, P., Vlachopoulos, N.,& Grätzel, M. (1993). Conversion of light to electricity by cis-X2bis (2, 2'-bipyridyl-4, 4'-dicarboxylate) ruthenium (II) charge-transfer sensitizers (X= Cl^-, Br^-, I^-, CN^-, and SCN^-) on nanocrystalline titanium dioxide electrodes. *Journal of the American Chemical Society*, *115*(14), 6382-6390.

[184] McEvoy, A.J., Markvart, T., & Castaner, L. (2012). Practical Handbook of Photovoltaics: Fundamentals and Applications. 2nd Edition, Academic Press, Waltham.

[185] Krysiak, E., Wypych-Puszkarz, A., Krysiak, K., Nowaczyk, G., Makrocka-Rydzyk, M., Jurga, S., & Ulanski, J. (2015). Core–shell system based on titanium dioxide with elevated value of dielectric permittivity: Synthesis and characterization. *Synthetic Metals*, *209*, 150-157.

[186] Robertson, N. (2006). Optimizing dyes for dye-sensitized solar cells. *Angewandte Chemie International Edition*, *45*(15), 2338-2345.

[187] Haque, S. A., Palomares, E., Cho, B. M., Green, A. N., Hirata, N., Klug, D. R., & Durrant, J. R. (2005). Charge separation versus recombination in dye-sensitized nanocrystalline solar cells: the minimization of kinetic redundancy. *Journal of the American Chemical Society*, *127*(10), 3456-3462.

[188] Nazeeruddin, M. K., Kay, A., Rodicio, I., Humphry-Baker, R., Müller, E., Liska, P., Vlachopoulos, N.,& Grätzel, M. (1993). Conversion of light to electricity by cis-X2bis (2, 2'-bipyridyl-4, 4'-dicarboxylate) ruthenium (II) charge-transfer sensitizers (X= Cl^-, Br^-, I^-, CN^-, and SCN^-) on nanocrystalline titanium dioxide electrodes. *Journal of the American Chemical Society*, *115*(14), 6382-6390.

[189] Chiba, Y., Islam, A., Watanabe, Y., Komiya, R., Koide, N., & Han, L. (2006). Dye-sensitized solar cells with conversion efficiency of 11.1%. *Japanese journal of applied physics*, *45*(7L), L638.

[190] Robertson, N. (2006). Optimizing dyes for dye-sensitized solar cells. *Angewandte Chemie International Edition*, *45*(15), 2338-2345.

[191] Suhaimi, S., Shahimin, M. M., Alahmed, Z. A., Chyský, J., & Reshak, A. H. (2015). Materials for enhanced dye-sensitized solar cell performance: Electrochemical application. *Int. J. Electrochem. Sci*, *10*(4), 2859-2871.

[192] Chang, H., & Lo, Y. J. (2010). Pomegranate leaves and mulberry fruit as natural sensitizers for dye-sensitized solar cells. *Solar energy*, *84*(10), 1833-1837.

[193] Sinha, D., De, D., & Ayaz, A. (2020). Photo sensitizing and electrochemical performance analysis of mixed natural dye and nanostructured ZnO based DSSC. *Sādhanā*, *45*(1), 1-12.

[194] Mortazavi, S. M., Kamali Moghaddam, M., Safi, S., & Salehi, R. (2012). Saffron Petals, a by-product for dyeing of wool fibers. *Progress in Color, Colorants and Coatings*, *5*(2), 75-84.

[195] Brouillard, R. (1982). Chemical structure of anthocyanins. *Anthocyanins as food colors*, 1-40.

[196] Valavanidis, A., & Vlachogianni, T. (2013). Plant polyphenols: recent advances in epidemiological research and other studies on cancer prevention. *Studies in Natural Products Chemistry*, *39*, 269-295.

[197] Goncalves, L. M., de Zea Bermudez, V., Ribeiro, H. A., & Mendes, A. M. (2009). Energy Environ. Sci. 2008, 1, 655;(d) Grätzel, M. *Acc. Chem. Res*, *42*, 1788.

[198] Grätzel, M. (2009). Recent advances in sensitized mesoscopic solar cells. *Accounts of chemical research*, *42*(11), 1788-1798.

[199] Winter, M., & Brodd, R.J. (2004). What Are Batteries, Fuel Cells, and Supercapacitors?. *Chemical Reviews*, *104*, 4245-4270.

[200] Jasim, K. E. (2011). Dye sensitized solar cells-working principles, challenges and opportunities. *Solar Cells-Dye-Sensitized Devices*, *8*, 172Ā210.

[201] Mehmood, U., Rahman, S. U., Harrabi, K., Hussein, I. A., & Reddy, B. V. S. (2014). Recent advances in dye sensitized solar cells. *Advances in Materials Science and Engineering*, *2014*.

[202] Yu, Z., Vlachopoulos, N., Gorlov, M., & Kloo, L. (2011). Liquid electrolytes for dye-sensitized solar cells. *Dalton transactions*, *40*(40), 10289-10303.

[203] de Freitas, J. N., Nogueira, A. F., & De Paoli, M. A. (2009). New insights into dye-sensitized solar cells with polymer electrolytes. *Journal of Materials Chemistry*, *19*(30), 5279-5294.

[204] Zhang, W., Cheng, Y., Yin, X., & Liu, B. (2011). Solid-state dye-sensitized solar cells with conjugated polymers as hole-transporting materials. *Macromolecular Chemistry and Physics*, *212*(1), 15-23.

[205] Zulkifili, A. N. B., Kento, T., Daiki, M., & Fujiki, A. (2015). The basic research on the dye-sensitized solar cells (DSSC). *Journal of Clean Energy Technologies*, *3*(5), 382-387.

[206] Suhaimi, S., Shahimin, M. M., Alahmed, Z. A., Chyský, J., & Reshak, A. H. (2015). Materials for enhanced dye-sensitized solar cell performance: Electrochemical application. *Int. J. Electrochem. Sci*, *10*(4), 2859-2871.

[207] Mahmoud, E. (2013). Electrochemical applications of carbon nanotube. *Journal of Nanotechnology & Advanced Materials* , *1*(1), 23-38.

[208] Sharma, S., Ranjan, P., Das, S., Gupta, S., Bhati, R., & Majumdar, A. (2012). Synthesis of Carbon Nanotube Using Olive Oil and It's Application in DYE Sensitized Solar Cell. *International Journal of Renewable Energy Research (IJRER)*, *2*(2), 274-279.

[209] Subramanian, A., Ho, C. Y., & Wang, H. (2013). Investigation of various photoanode structures on dye-sensitized solar cell performance using mixed-phase TiO_2. *Journal of alloys and compounds*, *572*, 11-16.

[210] Mahmood, S. S., Atiya, A. J., Abdulrazzak, F. H., Alkaim, A. F., & Hussein, F. H. (2021). A Review on applications of carbon nanotubes (cnts) in solar cells. *Journal of Medicinal and Chemical Sciences*, *4*(3), 225-229.

[211] Hagfeldt, A., & Grätzel, M. (2000). Molecular photovoltaics. *Accounts of chemical research*, *33*(5), 269-277.

[212] Chen, L., Zhou, Y., Tu, W., Li, Z., Bao, C., Dai, H., Yu, T., Liu, J.,& Zou, Z. (2013). Enhanced photovoltaic performance of a dye-sensitized solar cell using graphene–TiO_2 photoanode prepared by a novel in situ simultaneous reduction-hydrolysis technique. *Nanoscale*, *5*(8), 3481-3485.

[213] Sharma, S., Ranjan, P., Das, S., Gupta, S., Bhati, R., & Majumdar, A. (2012). Synthesis of Carbon Nanotube Using Olive Oil and It's Application in DYE Sensitized Solar Cell. *International Journal of Renewable Energy Research (IJRER)*, *2*(2), 274-279.

[214] Wang, H. H., Su, C., Wu, C. Y., Tsai, H. B., Li, C. Y., & Li, W. R. (2013). Preparation of composite light-scattering layer for dye sensitized solar cells. *Thin Solid Films*, *529*, 15-18.

[215] Yang, N., Zhai, J., Wang, D., Chen, Y., & Jiang, L. (2010). Two-dimensional graphene bridges enhanced photoinduced charge transport in dye-sensitized solar cells. *ACS nano*, *4*(2), 887-894.

[216] Koo, B. K., Lee, D. Y., Kim, H. J., Lee, W. J., Song, J. S., & Kim, H. J. (2006). Seasoning effect of dye-sensitized solar cells with different counter electrodes. *Journal of Electroceramics*, *17*(1), 79-82.

[217] Fang, Y., Ma, P., Cheng, H., Tan, G., Wu, J., Zheng, J., Zhou, X., Fang, S.,Dai, Y., & Lin, Y. (2019). Synthesis of Low-Viscosity Ionic Liquids for Application in Dye-Sensitized Solar Cells. *Chemistry–An Asian Journal*, *14*(23), 4201-4206.

[218] Rangel, D., Gallegos, J. C., Vargas, S., García, F., & Rodríguez, R. (2019). Optimized dye-sensitized solar cells: A comparative study with different dyes, mordants and construction parameters. *Results in Physics*, *12*, 2026-2037.

[219] Hahsim, E. T., & Abbood, A. A. (2016). Temperature effect on power drop of different photovoltaic modules. *Journal of Engineering*, *22*(5), 129-143.

[220] Gasföreningen, Gasol, ASTM International, D1835 -16 Standard Specification for Liquefied Petroleum (LP) Gases, October 2016. [Online].

[221] Zhang, Q., Huang, J. Q., Zhao, M. Q., Qian, W. Z., Wang, Y., & Wei, F. (2008). Radial growth of vertically aligned carbon nanotube arrays from ethylene on ceramic spheres. *Carbon*, *46*(8), 1152-1158.

[222] Gurleen, K., & Sahil, S. (2018). Gas Chromatography –A Brief Review. *International Journal of Information and Computing Science* , *5*(7),125-131.

[223] Raman, C. V., & Krishnan, K. S. (1928). A new type of secondary radiation. *Nature*, *121*(3048), 501-502.

[224] Beer, R. (1992). *Remote sensing by Fourier transform spectrometry* (Vol. 170). John Wiley & Sons.

[225] Ghosh, P., Afre, R. A., Soga, T., & Jimbo, T. (2007). A simple method of producing single-walled carbon nanotubes from a natural precursor: eucalyptus oil. *Materials Letters, 61*(17) ,3768–3770 .

[226] Graupner, R.(2007).Raman spectroscopy of covalently functionalized single-wall carbon nanotubes. *Journal of Raman Spectroscopy*, *38*, 673-683.

[227] Kao, C. C., & Young, R. J. (2004). A Raman spectroscopic investigation of heating effects and the deformation behaviour of epoxy/SWNT composites. *Composites Science and Technology*, *64*(15), 2291-2295.

[228] Espinosa, L. I. (2014).Determination of the Thermal Expansion Coefficient of Sngle Walled Carbon Nanotubes by Raman Spectroscopy. *International Journal for Rapid Communication*,139-145.

[229] Goldstein, J., Newbury, D.E., Joy, D.C., Lyman, C.E., Echlin, P., Lifshin, E., Sawyer, L., & Michael, J.R. (2003). Scanning Electron Microscopy and X-ray Microanalysis. *Springer*, Berlin .

[230] Popov, V. N. (2004). Carbon nanotubes: properties and application. *Materials Science and Engineering: R: Reports*, *43*(3), 61-102.

[231] Balta-Calleja, F. J., & Vonk, C. G. (1989). *X-ray scattering of synthetic polymers* (No. 8). Elsevier Science Limited.

[232] Suryanarayana, C., & Norton, M. G. (1998). *X-ray diffraction: a practical approach*. Springer Science & Business Media.

[233] Zhang, H., Lin, G., Zhou, Z., Dong, X., & Chen, T. (2002). Raman spectra of MWCNTs and MWCNT-based H_2 adsorbing system. *Carbon*, *40*, 2429-2436.

[234] Coats, A. W., & Redfern, J. P. (1963). Thermogravimetric analysis: A review. *Analyst*, *88*(1053), 906–924.

[235] International Organization for Standards (ISO) 11358:1997. Thermogravimetry (TG) of polymers-part 1: General principles. Switzerland: International Organization for Standardization.

[236] Mansfield, E., Kar, A., & Hooker, S. A. (2010). Applications of TGA in quality control of SWCNTs. *Analytical and bioanalytical chemistry*, *396*(3), 1071-1077.

[237] Arepalli, S., Freiman, S. W., Hooker, S. A., & Migler, K. D. (2008). Measurement issues in single-wall carbon nanotubes.

[238] Trigueiro, J. P. C., Silva, G. G., Lavall, R. L., Furtado, C. A., Oliveira, S., Ferlauto, A. S., Rodrigo,L.G., Ladeira, L.O., Liu, J.W., Frost, R.,& George, G. A. (2007). Purity evaluation of carbon nanotube materials by thermogravimetric, TEM, and SEM methods. *Journal of Nanoscience and Nanotechnology*, *7*(10), 3477-3486.

[239] Murakami, Y., Miyauchi, Y., Chiashi, S., & Maruyama, S. (2003). Characterization of single-walled carbon nanotubes catalytically synthesized from alcohol. *Chemical Physics Letters*, *374*(1-2), 53-58.

[240] Bahr, J. L., & Tour, J. M. (2002). Covalent chemistry of single-wall carbon nanotubes. *Journal of Materials Chemistry*, *12*(7), 1952-1958.

[241] Hennrich, F., Wellmann, R., Malik, S., Lebedkin, S., & Kappes, M. M. (2003). Reversible modification of the absorption properties of single-walled carbon nanotube thin films via nitric acid exposure. *Physical Chemistry Chemical Physics*, *5*(1), 178-183.

[242] Mansfield, E., Tyner, K. M., Poling, C. M., & Blacklock, J. L. (2014). Determination of nanoparticle surface coatings and nanoparticle purity using microscale thermogravimetric analysis. *Analytical chemistry*, *86*(3), 1478-1484.

[243] Safarova, K., Dvorak, A., Kubinek, R., Vujtek, M., & Rek, A. (2007). Usage of AFM, SEM and TEM for the research of carbon nanotubes. *Modern Research and Educational Topics in Microscopy*, *2*, 513-519.

[244] Anas, N. S., Dash, R. K., Rao, T. N., & Vijay, R. (2017). Effect of carbon nanotubes as reinforcement on the mechanical properties of aluminum-copper-magnesium alloy. *Journal of Materials Engineering and Performance*, *26*(7), 3376-3386.

[245] Lehman, J. H., Terrones, M., Mansfield, E., Hurst, K. E., & Meunier, V. (2011). Evaluating the characteristics of multiwall carbon nanotubes. *Carbon*, *49*(8), 2581-2602.

[246] Itkis, M. E., Perea, D. E., Jung, R., Niyogi, S., & Haddon, R. C. (2005). Comparison of analytical techniques for purity evaluation of single-walled carbon nanotubes. *Journal of the American Chemical Society*, *127*(10), 3439-3448.

[247] Bellucci, S., Gaggiotti, G., Marchetti, M., Micciulla, F., Mucciato, R., Regi, M.(2007). Atomic Force Microscopy Characterization of Carbon Nanotubes. *Journal of Physics: Conference Series*, 61-99.

[248] Boroumand, F., Moser, J. E., & Van Den Bergh, H. (1992). Quantitative diffuse reflectance and transmittance infrared spectroscopy of nondiluted powders. *Applied Spectroscopy*, *46*(12), 1874-1886.

[249] Kim, Y. I., Atherton, S. J., Brigham, E. S., & Mallouk, T. E. (1993). Sensitized layered metal oxide semiconductor particles for photochemical

hydrogen evolution from nonsacrificial electron donors. *The Journal of Physical Chemistry*, *97*(45), 11802-11810.

[250] Ammar, A. M., Mohamed, H. S., Yousef, M. M., Abdel-Hafez, G. M., Hassanien, A. S., & Khalil, A. S. (2019). Dye-sensitized solar cells (DSSCs) based on extracted natural dyes. *Journal of Nanomaterials*, *2019*.

[251] Jang, Y. J., Thogiti, S., Lee, K. Y., & Kim, J. H. (2019). Long-term stable solid-state dye-sensitized solar cells assembled with solid-state polymerized hole-transporting material. *Crystals*, *9*(9), 452.

[252] Pathak, C., Surana, K., Kumar V. S., & Singh, P. K.(2019). Fabrication and characterization of dye sensitized solar cell using natural dyes. *Materials Today: Proceedings*,*12*, 665–670.

[253] Younas, M., Gondal, M. A., Dastageer, M. A., & Baig, U. (2019). Fabrication of cost effective and efficient dye sensitized solar cells with WO_3-TiO_2 nanocomposites as photoanode and MWCNT as Pt-free counter electrode. *Ceramics International*, *45*(1), 936-947.

[254]- Hao, S., et al. "Natural dyes as photosensitizers for dye-sensitized solar cell." Solar energy80(2): 209-214(2006).

[255] Trihutomo, P., Soeparman, S., Widhiyanuriyawan, D., & Yuliati, L. (2019). Performance improvement of dye-sensitized solar cell-(DSSC-) based natural dyes by clathrin protein. *International Journal of Photoenergy*, *2019*.

[256]- Singer, G., Siedlaczek, P., Sinn, G., Rennhofer, H., Mičušík, M., Omastová, M., & Lichtenegger, H. C. (2018). Acid free oxidation and simple dispersion method of MWCNT for high-performance CFRP. *Nanomaterials*, *8*(11), 912.

[257]-Soroodan Miandoab, E., & Fatemi, S. (2015). Upgrading TiO_2 photoactivity under visible light by synthesis of MWCNT/TiO_2 nanocomposite. *International Journal of Nanoscience and Nanotechnology*, *11*(1), 1-12.

[258] Liu, X., Xiao, G., Chen, W., Xu, Y., & Wu, J. (2004). Quantification and purification of mulberry anthocyanins with macroporous resins. *Journal of Biomedicine and Biotechnology*, *2004*(5), 326.

[259] Thickness, P., Plasmon, S., Jaafar, H., Rosnan, R. M., Yahaya, H., & Abdullah, S. S.(2019). Enhancing Photocurrent Performance Based on Dye-Sensitized Solar Cells, 12(2111), 1–14.

[260] Yue, G., Cheng, R., Gao, X., Fan, L., Mao, Y., Gao, Y., & Tan, F. (2020). Synthesis of MoIn $_2S_4$@ CNTs Composite Counter Electrode for Dye-Sensitized Solar Cells. *Nanoscale Research Letters*, *15*(1), 1-10.

[261]- Ndeze, U. I., Aidan, J., Ezike, S. C., & Wansah, J. F. (2021). Comparative performances of nature-based dyes extracted from Baobab and Shea leaves photo-sensitizers for dye-sensitized solar cells (DSSCs). *Current Research in Green and Sustainable Chemistry*, *4*, 100105.

[262] Halka, M., Smoleń, S., Ledwożyw-Smoleń, I., & Sady, W. (2020). Comparison of effects of potassium iodide and iodosalicylates on the antioxidant potential and iodine accumulation in young tomato plants. *Journal of Plant Growth Regulation*, *39*(1), 282-295.

[263] Kondo, D., Sato, S., & Awano, Y. (2006). Low-temperature synthesis of single-walled carbon nanotubes with a narrow diameter distribution using size-classified catalyst nanoparticles . *Chemical Physics Letters* , *422*, 481-487.

[264] Toussi, S. M., FAKHRU'L-RAZI, A., Chuah, A., & Suraya, A. (2011). Effect of synthesis condition on the growth of SWCNTs via catalytic chemical vapour deposition. *Sains Malaysiana*, *40*(3), 197-201.

[265] Singh, C., Shaffer, M. S., Koziol, K. K., Kinloch, I. A., & Windle, A. H. (2003). Towards the production of large-scale aligned carbon nanotubes. *Chemical Physics Letters*, *372*(5-6), 860-865.

[266] Colindres, S. C., Aguir, K., Cervantes Sodi, F., Vargas, L. V., Salazar, J. A. M., & Febles, V. G. (2014). Ozone sensing based on palladium decorated carbon nanotubes. *Sensors*, *14*(4), 6806-6818.

[267] Akhavan, O., Azimirad, R., Safa, S., & Larijani, M. M. (2010). Visible light photo-induced antibacterial activity of CNT–doped TiO_2 thin films with various CNT contents. *Journal of Materials Chemistry*, *20*(35), 7386-7392.

[268]Mansfield, E., Kar, A., & Hooker, S. A. (2010). Applications of TGA in quality control of SWCNTs. *Analytical and bioanalytical chemistry*, *396*(3), 1071-1077.

[269] Kittel, C., McEuen, P., & McEuen, P. (1996). *Introduction to solid state physics* (Vol. 8, pp. 105-130). New York: Wiley.

[270] Dresselhaus, M. S., & Eklund, P. C. (2000). Phonons in carbon nanotubes. *Advances in physics*, *49*(6), 705-814.

[271] Nishimura, K., Okazaki, N., Pan, L., & Nakayama, Y.(2004). In Situ Study of Iron Catalysts for Carbon Nanotube Growth Using X-Ray Diffraction Analysis. *Japanese Journal of Applied Physics , 43*(4),471–474 .

[272] Abuilaiwi, F. A., Laoui, T., Al-Harthi, M., & Atieh, M. A. (2010). Modification and functionalization of multiwalled carbon nanotube (MWCNT) via fischer esterification. *The Arabian Journal for Science and Engineering*, *35*(1), 37-48.

[273] Ganguly, S., Leela Mohana Reddy, A., & Ramaprabhu, S. (2009). *Biological Sensors Using Dna Functionalized Multiwalled Carbon Nanotubes*. INDIAN INST OF TECH MADRAS DEPT OF PHYSICS.

[274] Davis, W. M., Erickson, C. L., Johnston, C. T., Delfino, J. J., & Porter, J. E. (1999). Quantitative Fourier Transform Infrared spectroscopic investigation humic substance functional group composition. *Chemosphere*, *38*(12), 2913-2928.

[275] Abdulrazzak, F. H., & Hussein, F. H. (2015). Effects of nanoparticle size on catalytic and photocatalytic activity of carbon nanotubes-titanium dioxide composites. *J. Environ. Anal. Chem*, *2*(2).

[276] Xie, Y., Heo, S., Yoo, S., Ali, G., & Cho, S. (2010). Synthesis and photocatalytic activity of anatase TiO_2 nanoparticles-coated carbon nanotubes. *Nanoscale Research Letters*, *5*(3), 603-607.

[277] Carp, O., Huisman, C. L., & Reller, A. (2004). Photoinduced reactivity of titanium dioxide. *Progress in solid state chemistry*, *32*(1-2), 33-177.

[278] Gao, B., Chen, G. Z., & Puma, G. L. (2009). Carbon nanotubes/titanium dioxide ($CNTs/TiO_2$) nanocomposites prepared by conventional and novel surfactant wrapping sol–gel methods exhibiting enhanced photocatalytic activity. *Applied Catalysis B: Environmental*, *89*(3-4), 503-509.

[279] Liu, G., Yan, X., Chen, Z., Wang, X., Wang, L., Lu, G. Q., & Cheng, H. M. (2009). Synthesis of rutile–anatase core–shell structured TiO_2 for photocatalysis. *Journal of Materials Chemistry*, *19*(36), 6590-6596.

[280] Xie, Y., Heo, S., Yoo, S., Ali, G., & Cho, S. (2010). Synthesis and photocatalytic activity of anatase TiO2 nanoparticles-coated carbon nanotubes. *Nanoscale Research Letters*, *5*(3), 603-607.

[281] Eskandarloo, H., Badiei, A., Behnajady, M. A., & Ziarani, G. M. (2015). UV-LEDs assisted preparation of silver deposited TiO_2 catalyst bed inside microchannels as a high efficiency microphotoreactor for cleaning polluted water. *Chemical Engineering Journal*, *270*, 158-167.

[282] Ding, M., Sorescu, D. C., & Star, A. (2013). Photoinduced charge transfer and acetone sensitivity of single-walled carbon nanotube–titanium dioxide hybrids. *Journal of the American Chemical Society*, *135*(24), 9015-9022.

[283] Shaban, M., Abukhadra, M. R., & Hamd, A. (2018). Recycling of glass in synthesis of MCM-48 mesoporous silica as catalyst support for Ni_2O_3 photocatalyst for Congo red dye removal. *Clean Technologies and Environmental Policy*, *20*(1), 13-28.

[284] Mohamed, F., Abukhadra, M. R., & Shaban, M. (2018). Removal of safranin dye from water using polypyrrole nanofiber/Zn-Fe layered double

hydroxide nanocomposite (Ppy NF/Zn-Fe LDH) of enhanced adsorption and photocatalytic properties. *Science of the Total Environment*, *640*, 352-363.